Title
STATISTICAL THERMODYNAMICS OF PARTICULATE FLUIDIZATION

Authors
Saxton, James A.
Vermeulen, Theodore.

Publication Date
1966-12-01

UCRL-11216

University of California

Ernest O. Lawrence Radiation Laboratory

STATISTICAL THERMODYNAMICS OF PARTICULATE FLUIDIZATION

Berkeley, California

DISCLAIMER

UCRL-11216

UNIVERSITY OF CALIFORNIA
Lawrence Radiation Laboratory
Berkeley, California

AEC Contract No. W-7405-eng-48

STATISTICAL THERMODYNAMICS OF PARTICULATE FLUIDIZATION

James A. Saxton, Jr. and Theodore Vermeulen

December 1966

STATISTICAL THERMODYNAMICS OF PARTICULATE FLUIDIZATION

Contents

I. INTRODUCTION

In order to establish a firm basis for exploring the utility of liquid theory as a guide in understanding fluidized-bed phenomena, it is necessary first to be cognizant of the current status of liquid theory. A fundamental review of the statistical-mechanical foundations of liquid theory and a description of fluidized-bed phenomena are therefore presented below. The basic liquid theory discussed here is that presented in the general statistical-mechanics texts listed as References H1, P1, and T1.

A. Statistical Mechanical Theory of Liquids

The science of "statistical mechanics" employs the theory of probability to deduce the thermodynamic and transport properties of a system containing a very large number of molecules (of the order of 10^{20} or more) from knowledge of the mechanical behavior of the individual molecules. The basic feature of this approach is the mathematical construction of an ensemble of systems, i.e., a collection of a large number ($n \to \infty$) of systems, each constructed to be a qualitative or geometric replica on the macroscopic scale of the actual thermodynamic system of interest, or a subsystem within it. The fundamental assumption made, known as the "ergodic hypothesis," is that the "system of actual interest (which serves as the prototype for the systems of the ensemble) spends equal amounts of time, over a long period of time, in each of the available quantum states" (H2).

The nature of the ensemble is directly related to the thermodynamic description of the actual system. That is, the constraints on the thermodynamic system establish the restrictive conditions that apply to the ensemble. The cononical ensemble is of most frequent utility for liquids; it represents a closed isothermal system having a number of molecules N, volume V, and an absolute temperature T, serving as its constraints, e.g., an enclosed system immersed in a constant temperature bath and thermally in equilibrium with it. For the most part, the remainder of this discussion will be confined to such a system.

In the canonical ensemble, the probability of observing a given quantum state j (having energy E_j) in an arbitrary system of the ensemble is

$$P_j = \frac{e^{-\beta E_j}}{\sum_i e^{-\beta E_i}} \qquad (I-1)$$

where state j is included among the accessible states i=1, 2,...n. The denominator is named the partition function (or sum over states), Z, and β is the reciprocal of kT, k being the Boltzmann constant. The thermodynamic entropy, a function of the randomness of the system, is defined as

$$S = -k \sum_i^N P_i \ln P_i \qquad (I-2)$$

and the macroscopic equilibrium value of a property whose value is D_j

when the system is in quantum state j is

$$\overline{D} = \sum_i D_i P_i = \frac{\sum_i D_i \exp(-\beta E_i)}{Z} \qquad (I\text{-}3)$$

Thus it is easily shown that if the partition function is known, all of the thermodynamic properties of the ensemble can be calculated directly. For example,

$$E = \frac{\sum_i E_i \exp(-\beta E_i)}{\sum_i \exp(-\beta E_i)} = -\frac{\partial}{\partial \beta} \ln \sum_i \exp(-\beta E_i) \qquad (I\text{-}4)$$

$$= kT^2 \left(\frac{\partial \ln Z}{\partial T}\right)_V$$

$$S = kT \left(\frac{\partial \ln Z}{\partial T}\right)_{N,V} + k \ln Z \qquad (I\text{-}5)$$

$$F = E - TS = -kT \ln Z \qquad (I\text{-}6)$$

and $$p = -\left(\frac{\partial F}{\partial V}\right)_{N,T} = kT \left(\frac{\partial \ln Z}{\partial V}\right)_{N,T} \qquad (I\text{-}7)$$

To evaluate the partition function properly it is necessary to solve the quantum mechanical wave equation for N interacting particles, in order to establish the energy levels. Clearly, this is an impossible task, and simplifying assumptions are in order. These assumptions are

in the nature of a decoupling of the less significant intra- and intermolecular interactions, such that the resulting molecular model possesses a manageable number of degrees of freedom and yet truly represents physical reality. The following discussion lists these assumptions and furnishes the basis for an understanding of the major current liquid theories.

In general, the energy of each quantum state is the sum of contributions from the different degrees of freedom. Therefore, because of its exponential dependence upon energy, the partition function can be expressed as the product of factors related to the separate degrees of freedom, i.e.,

$$Z = Z_{int} \cdot Z_{tr} \qquad (I-8)$$

where Z_{tr} (the translational partition function) is the contribution due to the positions and motions of the centers of mass of the molecules, and Z_{int} (the internal partition function) is related to the rotational, vibrational, electronic, and nuclear degrees of freedom of the molecule.

So far our development has been in terms of quantum states, but for other than low temperatures, the energy levels are sufficiently close that the classical approximations can be used. The translational partition function is then

$$Z_{tr} = \frac{1}{N!}\frac{1}{h^{3N}} \int \cdots \int \exp(-\beta H)\, d\vec{p}_1 \cdots d\vec{p}_N\, d\vec{r}_1 \cdots d\vec{r}_N \qquad (I-9)$$

where H is the Hamiltonian, $d\vec{p}_i$ is the volume element in momentum space,

$d\vec{r}_i$ the volume element in position space occupied by molecule i. In most instances, the Hamiltonian can be expressed as a sum of momentum and potential contributions:

$$H = \frac{1}{2m}\sum_{i}^{N}(\vec{p}_i)^2 + W(\vec{r}_1 \cdots \vec{r}_N) \qquad (I\text{-}10)$$

where $W(\vec{r}_1 \ldots \vec{r}_N)$ is the potential energy of the system when the molecules are located at $\vec{r}_1 \ldots \vec{r}_N$. The partition function in this case is separable, and the following expression results:

$$Z_{tr} = \int \cdots \int \exp(-\beta W)\, d\vec{r}_1 \cdots d\vec{r}_N \Big/ \left[h/(2\pi m kT)\right]^{3N} \qquad (I\text{-}11)$$

We thus have $Z_{tr} = Q/\Lambda^{3N}$. Within the accuracy of the above development, and because the mutual separation of the molecules can be defined, the configuration partition function is:

$$Q = \int \cdots \int \exp(-\beta W)\, d\vec{r}_1 \cdots d\vec{r}_N \qquad (I\text{-}12)$$

If we now restrict our discussion to monatomic fluids, for which $Z_{int} = 1$, the thermodynamic properties can be expressed in terms of the configuration partition function. Thus,

$$E = kT^2\left[\frac{\partial}{\partial T}\ln(Q/\Lambda^{3N})\right]_{N,T} = 3NkT + kT^2\left(\frac{\partial \ln Q}{\partial T}\right)_{N,V} \qquad (I\text{-}13)$$

$$S = \frac{3}{2}Nk + k\ln(Q/\Lambda^{3N}) + kT\left(\frac{\partial \ln Q}{\partial T}\right)_{N,V} \qquad (I\text{-}14)$$

$$F = -kT\ln(Q/\Lambda^{3N}) \qquad (I\text{-}15)$$

and

$$p = kT\left(\frac{\partial \ln Q}{\partial V}\right)_{N,T} \qquad (I\text{-}16)$$

The evaluation of the configuration partition function for the entire thermodynamic system remains a difficult task, since it depends upon the location of N (of the order of 10^{20}) molecules, and the extent of their interaction with each other. However, the total interaction of any one molecule with the others is given to a high order of approximation by the vector sum of its individual and separate interactions with each of its immediate neighbors; this is known as the pairwise additivity approximation. Utilizing this approximation, calculations have been made on high speed computers for a small number (10^4) of molecules interacting according to simple parametric intermolecular potentials, e.g., hard-sphere and perturbed square-well potentials (R1, P2, S1, S2).

Two calculation methods are employed: the Monte Carlo method (R1) selects rearrangements in the molecular distribution in a random manner subject to appropriate constraints; the molecular-dynamic method (P2, S1, S2) specifies initial and boundary conditions and solves Newton's

equations of motion for the particles. The two methods yield thermodynamic predictions in good agreement with each other, and the molecular-dynamic method possesses the additional capability of calculating transport properties. These calculations are useful in furnishing an exact result to which other predictions may be compared, but possess the obvious limitation of being able to handle only a small number of molecules, and of requiring an extremely large ratio of computer time to real time.

To simplify further the calculation of the configurational partition function an additional restriction is necessary, and it is the nature of this restriction that differentiates the various liquid theories. Although differing in specific form, all current liquid theories consider that molecular interaction take place only among particles in a subsystem; that is, a given molecule interacts with n ($n \ll N$) particles in an average potential field established by the (N-n) other particles. Mathematically, the irrelevance of the remaining particles is accounted for by averaging over all the configurations available to them. The justification of this assumption lies in the experimental observation that while liquids possess short-range order (among molecules in the subsystem) there is negligible long-range order.

Virtually all liquid theories are of the one-body variety, with a few extensions into the two-body domain. These theories fall into two general categories: the first employs knowledge of the radial distribution of molecules around a central molecule, which is established by experimental or theoretical means, to predict the thermodynamic properties; the second postulates that a hypothetical cage exists

around each molecule, with suitable choice of properties for the environment within the cell leading to quantitative predictions of liquid behavior. Each approach possesses certain advantages, and will now be discussed in more detail.

1. One-Component Systems

The one-component system offers a great simplification in evaluation of the partition function. Since all the molecules are identical, the perturbation to the multicomponent partition function that accompanies an interchange of unlike molecules within a given spacial configuration need not be considered. Therefore, the one-component partition function depends only upon the spacial location of the molecules, not upon their individual identity. A factor of $(N!)^{-1}$ is accordingly introduced into the partition function given in Eq. (I-12) so that each quantum state will be counted only once.

With this in mind, we proceed to a consideration of the specific liquid theories.

a. Radial-Distribution-Function Method. The radial-distribution-function method in its most general form furnishes an exact description of liquids in terms of a radial-distribution function g(r) defined as the ratio of local density to the average density of the fluid. Unfortunately the distribution function cannot be experimentally measured with sufficient accuracy, and the alternative theoretical development leads to an insoluble set of N+1 inter-related integral equations. The approximation necessary for the closure of the set of integral equations constitutes the essential limitation of this method.

The general characteristics of the distribution function are illustrated in Figure I-1 . The form of this function has been verified by experimental X-ray diffraction measurements. From its definition, the departure from unity measures the short-range order, relative to a given molecule, in the arrangement of its neighbors.

$g^{[n+1]}(r_2 \xi)$. Kirkwood (K1) proposed a "superposition principle", analogous to the Hartree approximation in quantum mechanics (H3), to close this set of integral equations. This principle is illustrated by considering a three-body distribution to be expressed in terms of the pair-distribution functions of the three molecules:

$$g(\vec{r}_1, \vec{r}_2, \vec{r}_3) = g(\vec{r}_1, \vec{r}_2)\, g(\vec{r}_2, \vec{r}_3)\, g(\vec{r}_1, \vec{r}_3) \qquad (I\text{-}20)$$

The manner in which the superposition approximation is introduced is also of importance; two different equations for the radial-distribution function have been developed. These equations, derived by Kirkwood (K1) and by Born and Green (B1) are both first-order nonlinear equations and differ only because the superposition approximation is inexact.

The thermodynamic properties can be established by inserting the expression for the radial-distribution function into Eqs. (I-17) - (I-19). The resulting predictions have been found to be quite acceptable from a qualitative standpoint. Due to the approximations involved, they are not quantitatively accurate, however. When they are compared with the exact results for a hard sphere fluid as calculated by Kirkwood, Mann, and Alder (K2), the agreement is seen to become increasingly unsatisfactory at the higher densities where triplet and higher order interactions become important. The lack of success of the distribution-function method in obtaining accurate quantitative predictions suggests that it might be fruitful to examine a more intuitive model based on the short-range order observed in liquids.

b. Free-Volume Theories. The short-range order existing in liquid molecular structure has been mentioned previously. The spacial necessity for such ordering can be traced to the relatively minor volume change that occurs upon melting, and to the extremely large short-range repulsive forces that preclude molecular inter-penetration. For a molecule to move through the liquid it must penetrate the potential barrier formed by its interaction with the surrounding molecules. The motion can be described as a random walk of the molecule between groups of contiguous molecules. Between intergroup jumps the molecule oscillates about a quasi-equilibrium position within the cell formed by its neighbors. If the frequency of oscillation within each cell is much greater than the frequency of the intercell jumps, the thermodynamic properties of the liquid will be largely determined by the cell properties. The problem, then, is to determine the effective potential energy field within a cell, and, hence, to ascertain the Boltzman factor. This being done, the cell partition function and related thermodynamic properties can be established. Such is the nature of the free-volume or cell-model approach to liquid theory.

The free-volume approach, first suggested by Eyring and Hirschfelder (E1), describes a liquid as being composed of individual molecules, each moving in an average potential field created by its neighbors. The resulting partition function for each molecule can be written as

$$z = Z^{1/N} = z_{int} \cdot \frac{v_f \exp\left[-w/(kT)\right]}{\Lambda^3} \qquad (I\text{-}21)$$

where v_f is the free volume and ω is the energy of the molecule in its average potential field. This equation serves to define the free volume as the effective liquid-phase volume within which a molecule will obey the perfect gas law, $pv_f=kT$. The corresponding thermodynamic properties may be readily obtained by substituting Eq. (I-21) into Eqs. (I-13) - (I-16).

$$E = \frac{3}{2}NkT + N\omega + NkT^2\left(\frac{\partial \ln v_f}{\partial T}\right)_V \qquad (I\text{-}22)$$

$$S = Nk\ln(v_f/\Lambda^3) + \frac{3}{2}Nk + NkT\left(\frac{\partial \ln v_f}{\partial T}\right)_V \qquad (I\text{-}23)$$

$$F = N\omega - NkT\ln(v_f/\Lambda^3) \qquad (I\text{-}24)$$

$$p = -N\left(\frac{\partial \omega}{\partial V}\right)_T + NkT\left(\frac{\partial \ln v_f}{\partial V}\right)_T \qquad (I\text{-}25)$$

Eyring empirically related the microscopic variables, ω and v_f to the volumetric properties of the liquid, and succeeded in obtaining reasonable qualitative predictions.

A possibility for improving the Eyring approach would be to relate the parameters ω and v_f to the intermolecular force constants of the molecules. Lennard-Jones and Devonshire (L1) accordingly suggested a "cell model" for liquid structure, which provides expressions

for the force-field parameters in terms of molecular constants. They postulated that since the field acting upon a molecule is rapidly fluctuating, it could be represented by an average field possessing spherical symmetry. In that case, the mean energy of a molecule's interaction with its neighbors depends only upon the radial distance of the molecule from the center of the cell, $\omega(r)$. If the energy state is referenced to the energy of the system when all particles are at the center of their cells, the configuration partition function is

$$Q = v_f^N \exp\left[-N\omega(0)/(2kT)\right] \qquad (I\text{-}26)$$

where

$$v_f = 4\pi \int_{cell} \exp\left\{-\left[\omega(r)-\omega(0)\right]/2kT\right\} r^2 dr \qquad (I\text{-}27)$$

In this case then the free volume v_f serves as the cell partition function; and $N\omega(0)/2$ is the system energy when all particles are at the center of their cells.

Upon assuming a form for the intermolecular potential, e.g., the Lennard-Jones 6-12 potential, the mean energy can be evaluated as a function of radius in a straightforward manner. The resulting expression can be represented functionally by

$$\omega(r) = A\,\varepsilon^* \Phi\left[(d/a), (r/a)\right] \qquad (I\text{-}28)$$

where ε^* and d are the energy and distance parameters in the Lennard-Jones potential, a is the cell radius, and A is the number of nearest neighbors. The thermodynamic functions are again as given in Eqs. (I-22)-(I-25) where ω is now defined equal to $\omega(0)/2$.

Two special cases of cell theory are of sufficient interest to be considered here. The hard-sphere model, sketched in Figure I-2 for the case of hexagonal packing, most clearly illustrates the basic features of cell theory; a large number of calculations have been made for this case. The model postulates "billiard-like" molecules which interact with an infinite repulsive force upon contact, but experience no potential field between collisions. The molecular energy within the cell is thus:

$$\omega(r) = 0 \qquad 0 \leq r < (a-d) \tag{I-28a}$$

$$\omega(r) = \infty \qquad r \geq (a-d) \tag{I-28b}$$

Then from Eqs. (I-27) and (I-25) the free volume and the equations of state are easily determined to be

$$v_f = 4\pi/3 \cdot (a-d)^3 = 4\pi/3 \cdot \gamma\left(v^{1/3} - v_o^{1/3}\right)^3 \tag{I-29}$$

and

$$p = kT \Big/ \left[v^{2/3} \left(v^{1/3} - v_o^{1/3}\right)\right] \tag{I-30a}$$

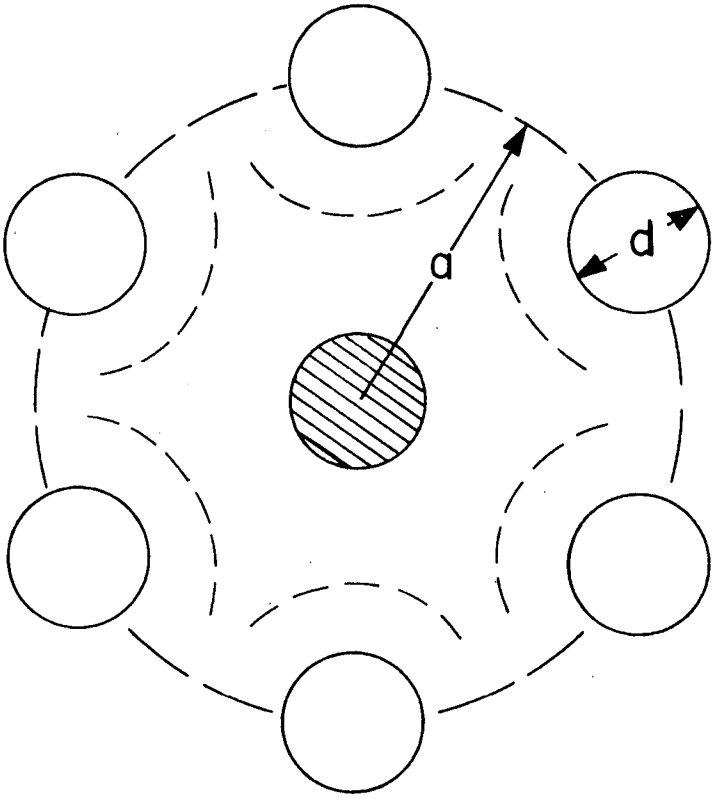

Fig. I-2. Schematic diagram of a hard-sphere-liquid cell with hexagonal packing.

XBL673-2264

where γ is an empirical packing parameter defined by $\gamma=a^3/v=d^3/v_o$ (e.g., $\gamma=\sqrt{2}$ for a face-centered cubic lattice) and v_o is the cell volume of closest packing. The agreement of this equation of state with numerical calculations using the Monte Carlo method is quite good (R1).

A "square-well" model developed by Prigogine (P3) and designated as the "smoothed-potential" approximation offers further improvement, yet possesses the simplicity of form necessary for analytic calculations. It assumes that the molecule in its cell is acted upon by a uniform potential given by the molecular potential of the molecule when located at the cell center. Physically such an assumption is justified by the fact that while a molecule's interaction with some molecules increases when it moves away from the cell center, its interaction with other molecules decreases, and in the range of liquid densities these two effects tend to compensate for each other. The model continues to assume hard-sphere molecular interactions, and the reference potential energy, $\omega(0)$, is generally calculated assuming a Lennard-Jones 6-12 potential. The form of the cell potential with respect to the reference potential is identical to that for hard spheres, i.e.,

$$\omega(r) - \omega(0) = 0 \qquad 0 \leq r < (a-d)$$

$$\omega(r) - \omega(0) = \infty \qquad r \geq (a-d) \qquad \text{(I-31)}$$

Thus the same partition function results, with v_f given by Eq. (I-29). The equation of state differs from Eq. (I-30), in that it now includes the volumetric dependence of the reference potential:

$$p = -\left[\partial w(0)/\partial v\right]_T + kT/\left[v^{2/3}(v^{1/3}-v_0^{1/3})\right] \qquad (I\text{-}32)$$

The last term on the right, the "thermal pressure," arises from the molecular motion of the hard spheres, and the first term, the "static pressure," results from the configuration, i.e., position-dependent, interaction between molecules. The importance of the smoothed-potential modification to the hard sphere model lies in the fact that the liquid-gas transition only occurs for molecules possessing an attractive potential (just as the liquid-solid transition depends on the repulsive potential).

The cell models discussed so far have been of the localized one-body variety, and as such they do not account for the so-called "communal entropy" of liquids. This entropy, which equals Nk, results from the disruption of order that occurs during the solid-liquid transition, and the consequent inability to associate a given molecule with a specific lattice site. The cell model, however, hypothetically divides the liquid into cells, and thus effectively 'reidentifies' the molecules. In an extensive examination of the cell model, Dahler and Hirschfelder (D1, D2) concluded that it is not possible to account satisfactorily for the communal entropy within the restrictions of the conventional cell model. For this reason, two extensions of cell theory, known as the multiple-occupation theory and the cell-cluster theory, have been proposed.

"Multiple occupation of cells" (P4) implies that more, or fewer, than one particle may occupy a cell. The interactions between the

molecules in the same cell are treated exactly, and the interactions between molecules in different cells are approximated by an average potential similar to that used in the Lennard-Jones and Devonshire model. The communal entropy is seen to arise as a result of fluctuations in the cell occupation numbers, i.e., density fluctuations on the molecular scale. The use of higher cell occupation numbers than one successfully predicts the correct communal entropy, and provides a continous transition from a one-particle model to the correct N-body model. It is found, however, that occupation numbers of three or more contribute only 10% of the communal entropy, and of course add greatly to the complexity of the problem. Therefore nearly all discussions of the multiple-cell-occupation approach are restricted to two or fewer molecules per cell. A well known example of this type is the "hole theory" developed by Cernushi and Eyring (C1). Although developed prior to the multiple-occupation theory, it is simply a special case in which the occupation numbers are restricted to be zero (i.e., a hole) or one; since it is only a one-body model, it offers no improvement over the standard cell model with regard to predicting the communal entropy. A more useful application of the general theory is to quantum liquids for which consideration of even doubly-occupied cells provides an insight into the effect of correlations between particle motions.

The cell-cluster theory developed by DeBoer (D3) is a more direct attempt to include correlations between particle motions through the concept of "cell clusters" of two or more neighboring cells. Within the cell cluster, the molecules move under the influence of their mutual

interaction and their interaction with the surrounding (N-n) molecules. The resulting cell-cluster partition function depends only on the number of cells in the cluster and their mutual arrangement. This theory predicts the correct communal entropy for a one dimensional gas. Although no calculation has been published for the condensed state, the correct result should be obtained if sufficiently large cell clusters are employed. (At high densities, a fluctuation will involve a large number of molecules and the cell clusters are correspondingly very large.) Because it accounts for the communal entropy, the concept of multiple occupation of cells seems to offer the best prospect for further development of cell-model theory.

The free-volume model has been discussed thoroughly because it offers an intuitively satisfying model for liquids and, for that reason, serves as the logical starting place for an application of liquid theory to fluidized beds. It must be kept in mind, however, that the assumed cell structure has too high a degree of order "built-in", and the calculated values of free volume depend upon the particular molecular arrangement assumed. Evincing this effect, the isotherms derived from free-volume theory, for other than large cell-clusters or multiply-occupied cells, resemble continuations of the crystalline isotherms. They agree neither with the Monte Carlo predictions nor with the experimental isotherms. Also, the radial-distribution functions calculated from the cell model differ markedly from those obtained by x-ray diffraction methods. Thus the free-volume model provides a useful counterpart to the radial-distribution-function method, but it too falls short of being an accurate quantitative theory.

2. Surface Tension

The existence of surface tension is traceable to the change in free energy which occurs when a molecule is removed from the isotropic potential environment of the bulk phase and placed in the nonisotropic potential environment of the surface phase. It may be defined in terms of the divergence of the local pressure of the close-spaced surface molecules p from the uniform isotropic bulk pressure p°:

$$\sigma = -\int_{-\infty}^{\infty} (p^\circ - p)\, dz' \qquad (I\text{-}33)$$

where σ is the surface tension and z' is the distance away from the plane of the surface. Eq. (I-33) is consistent with the usual macroscopic definition of surface tension in terms of the Helmholtz free energy:

$$\sigma = \left(\frac{\partial F}{\partial A'}\right)_T \qquad (I\text{-}34)$$

The former definition is employed by the radial-distribution-function approach, and the latter is used in the cell-model analysis.

a. Radial-Distribution-Function Method. The bulk hydrostatic pressure is given in terms of the radial-distribution function by Eq. (I-8):

$$p^{\circ} = \rho kT - \frac{\rho^2}{6}\int_0^{\infty} r \frac{dw}{dr}\, g(r)\, 4\pi r^2 dr \qquad (I\text{-}35)$$

The comparable expression for the local pressure is:

$$p(z_1) = \rho(z_1)kT - \rho(z_1)\int_{-\infty}^{0}\int_{-\infty}^{\infty}\int_{0}^{\infty}\int_{-\infty}^{\infty}\int_{z_1}^{\infty} \frac{x_2 - x_1}{r}\frac{dw}{dr}\rho(z_2)g(z_1, z_2, r)\, dx_2\, dy_2\, dz_2'\, dx_1 \qquad (I\text{-}36)$$

where z is the distance away from the surface plane and x_1, x_2, y_2, and z_2 are the remaining Cartesian coordinates of molecules one and two (with $y_1 \equiv 0$). By substitution of Eqs. (I-35) and (I-36) into Eq. (I-33) the surface tension may be obtained. Kirkwood and Buff (K3) have carried out such an evaluation.

b. Cell-Model Theory. Lennard-Jones and Corner (L3) ascertained surface tension from the cell model of the liquid state by determining the free energy difference between a mole of liquid with unit surface area and a mole of liquid with no surface area. The resulting expression for surface tension is:

$$\gamma = \Psi_o - \Phi_o + N_s kT \ln(v_f / v_s) \qquad (I\text{-}37)$$

where $\Psi_o - \Phi_o$ is the increase in potential energy per unit interfacial

area when two semi-infinite blocks of liquid with plane faces are moved from zero to infinite separation in a reversible isothermal process; N_s is the number of molecules per unit interfacial area; and v_f and v_s are the free volumes of a molecule in the bulk and surface phases, respectively.

Empirical observation of surface tension led to a relationship known as Eötvos' law (E2):

$$\sigma v^{2/3} = K(T_o - T) \qquad (I\text{-}38)$$

where K and T_o are independent of temperature. Equations (I-37) and (I-38) can be brought into accord with one another subject to two basic assumptions. These are that both the potential difference $\Psi_o - \Phi_o$, and the free volume ratio v_f/v_s are independent of temperature. Then since $N_s = v^{-2/3}$:

$$\sigma v^{2/3} = k \ln(v_s/v_f)\left[\frac{w_s(o) - w(o)}{2k\ln(v_s/v_f)} - T\right] \equiv K(T_o - T) \qquad (I\text{-}39)$$

c. Surface Wave Behavior. An assessment of the magnitude of the surface tension may be obtained by observing the behavior of a surface disturbance. The propagation velocity of surface waves under the combined influence of gravity and surface tension may be shown to be (M1):

$$c^2 = \left(\frac{g\lambda}{2\pi} + \frac{2\pi\sigma}{\lambda\rho}\right)\tanh\left(\frac{2\pi h}{\lambda}\right) \qquad (I\text{-}40)$$

where c and λ are, respectively, the wave velocity and wave length;

g is the gravitational acceleration; ρ is the fluid density; and h is the fluid depth. If the fluid depth is much greater than the wave length, the hyperbolic tangent factor approaches unity; then

$$c^2 = \frac{g\lambda}{2\pi} + \frac{2\pi\sigma}{\lambda\rho} \qquad (I\text{-}41)$$

Rearranging Eq. (I-41), we arrive at an expression for the surface tension:

$$\sigma = \frac{\rho\lambda}{2\pi}\left(c^2 - \frac{g\lambda}{2\pi}\right) \qquad (I\text{-}42)$$

Therefore, if we measure the wave speed and wave length for a fluid of known density the surface tension is directly obtainable.

3. Transport Properties

From the viewpoint of kinetic theory the distinction between equilibrium and nonequilibrium systems is not fundamental, as both depend upon the same molecular motions. It is therefore natural to expect that some knowledge of a system's nonequilibrium behavior may be gained from consideration of its equilibrium properties. Although this expectation has been realized in the case of dilute gases, for which Chapman (C2) and Enskog(E3) have obtained the nonequilibrium distribution function from a perturbation expansion about the corresponding equilibrium distribution function, the necessary introduction of multimolecular interactions and short-range order has so far prevented the development of a satisfactory equivalent theory for liquids.

In general the development of a complete theory for liquid transport phenomena has had to be approached from two distinct paths. One treatment has been concerned with the solution of the Boltzmann equation under the restriction of no intermolecular collisions; Kirkwood's (K3) Brownian-motion method falls into this category. The other approach has considered only the collision contribution to transport phenomena; originally developed for dense gases by Enskog (E2), it has recently been refined for liquids by Collins and Raffel (C3). Both theories will be discussed briefly in the following paragraphs.

a. Brownian-Motion Theory. The Brownian-motion approach to the establishment of liquid nonequilibrium theory involves an empirical assumption as to the nature of the dissipative process, and the inclusion

of the attributes of short-range order into the Liouville equation. Kirkwood (K4) introduced a parameter, the autocorrelation function $\S$, which serves as a measure of the dissipative behavior of the system:

$$\S = \left\langle F(t) \cdot F(t+\tau_1) \right\rangle \qquad \text{(I-43)}$$

where $F(t)$ is the force due to all neighbors on a given particle at time t, $F(t+\tau_1)$ is the force on the same particle at a later time $t+\tau_1$, and $\langle\ \rangle$ indicates an ensemble average. In effect $\S$ defines a transient "cluster" of 10 to 20 molecules. He then postulated that the nature of the dissipative (or randomization) process is such that a plateau time τ_c exists, for which

$$\begin{aligned} \S &\neq 0 \quad \text{if} \quad \tau_1 < \tau_c \\ \S &= 0 \quad \text{if} \quad \tau_1 > \tau_c \end{aligned} \qquad \text{(I-44)}$$

The essence of this hypothesis is that the forces acting upon a particle will cause it to escape from its initial force field within a time interval τ_c. Thus, for a coarse time scale with units greater than τ_c the system effectively exhibits molecular chaos.

Kirkwood also defined a related quantity, the friction constant,

$$\delta = \frac{1}{mkT} \int_0^{\tau_1} \S(t)\, dt \qquad \text{(I-45)}$$

applicable where $\tau_1 > \tau_c$. This quantity serves as a measure of the lifetime of the "cluster." Since the evaluation of δ is extremely complex, only

Since there is no "action at a distance" in a hard-sphere fluid, only binary collisions are considered; the collision frequency therefore has the value developed in the kinetic theory of gases, times a molecular shielding factor A. The corresponding flux tensor $\underset{\sim}{J}$ for such a system has been shown by Chapman and Cowling (C2) to be

$$\underset{\sim}{J} = \frac{A d^3}{2} \iiint (\psi' - \psi) f^{(2)}\left(\vec{c}_1, \vec{c}_2, \vec{r} - \frac{d}{2}\vec{k}, \vec{r} + \frac{d}{2}\vec{k}\right) \vec{g} \cdot \vec{k}\, \vec{k}\, d\vec{k}\, d\vec{c}_1 d\vec{c}_2 \qquad (I\text{-}52)$$

where ψ is the quantity being transferred, e.g., momentum or kinetic energy; ψ' is the amount of ψ possessed by the second molecule after collision, $f^{(2)}$ is the nonequilibrium pair-distribution function; $\vec{c}_1$ and $\vec{c}_2$ are the respective molecular velocities of the two molecules; $\vec{k}$ is a unit vector along the line of centers at collision; and $\vec{g}$ is the relative velocity, $\vec{c}_2 - \vec{c}_1$. Because of the lack of molecular interaction between collisions, it may be assumed that the velocity distributions of the two molecules are reestablished by the time a second collision occurs between them.

The form of the nonequilibrium pair-distribution function in Eq. (I-52) is therefore taken to be the product of the related equilibrium pair-distribution function and the Maxwellian form of the singlet-density product of the two molecules. The resulting expression for the stress tensor becomes equal to the pressure tensor upon substitution of

$$\psi' - \psi = m(c_2' + c_1' - c_2 - c_1) \qquad (I\text{-}53)$$

Comparison of terms then leads to

$$\eta = \frac{2}{5} d \left(\frac{mkT}{\pi}\right)^{1/2} \left(\frac{P}{kT} - \frac{1}{U}\right) \qquad \text{(I-54)}$$

for the shear viscosity coefficient.

A related development for the self-diffusion coefficient (L4) establishes

$$D_s = \frac{5}{12} \left(\frac{kT}{\pi m}\right)^{1/2} \left[a^2 \left(\frac{P}{kT} - \frac{1}{U}\right)\right]^{-1} \qquad \text{(I-55)}$$

Both coefficients are found to predict values which are a factor of two lower than the experimental values.

4. Mixtures

In principle the formulation of a statistical-mechanical theory of solutions should be very similar to that for pure fluids, since both problems involve the evaluation of the partition function of a general N-body system with many-body interactions. Actually, pure fluids exhibit many simplifying features when compared with mixtures, e.g.:

(i) In a highly-compressed pure fluid, it is frequently assumed that the average positions of the molecules are close to the sites of a regular lattice, while in a mixture the differences in molecular size result, at high densities, in a very irregular average configuration which depends upon composition.

(ii) Many theories of the liquid state take advantage of the indistinguishability of the configurations resulting from a simple interchange of molecules, but in a mixture such an interchange necessitates complex order-disorder considerations. One can write the pure fluid and mixture partition functions in a form which illustrates the order-disorder problem:

for a pure fluid: (I-56)

$$Q = \int_0^V \cdots \int_0^V \exp\left[-W(\vec{r}_1 \cdots \vec{r}_N)/kT\right] d\vec{r}_1 \cdots d\vec{r}_N$$

for a mixture: (I-57)

$$Q = \int_0^V \cdots \int_0^V \left\langle \exp\left[-W(\vec{r}_1 \cdots \vec{r}_N)/kT\right] d\vec{r}_1 \cdots d\vec{r}_N \right\rangle$$

where $\vec{r}_i$ is the position vector of molecule i, and W is the energy of a particular configuration. In Eq. (I-57) the symbol < > denotes an

average over all possible interchanges of the molecules among these positions.

Difficulties such as these have prevented the establishment of a wholly satisfactory theory for mixtures. Thus, for many years the theory of nonelectrolyte fluid solutions has been based upon the regular solution theory of Hildebrand and Scatchard (H4) and the several lattice theories of solution (G1). These theories are semiempirical in nature, since they cannot be derived from a general statistical-mechanical formulation in terms of well defined approximations, and thus they contain parameters whose exact physical definitions are obscure. As the result of a great deal of work on solution theory during the last decade, progress has been made in more fundamental approaches, such as the extension of the radial-distribution-function (RDF) method to mixtures (F1), and the use of perturbation techniques, in which the perturbation may involve a molecular parameter or the intermolecular potential itself, to develop improved "mixture theories" (N1). It is worthwhile to discuss here the basic assumptions and principal results of the RDF approach, and of the mixture theory that extends the cell model to solutions.

a. Radial-Distribution-Function Method. From a formal point of view, the radial-distribution function can be easily formulated for a mixture. For example, the equation of state is given by

$$p = \rho kT + \frac{\rho^2}{6} \int_0^\infty \sum_{ij} x_i x_j r \frac{dW_{ij}}{dr} g_{ij}(r)\, 4\pi r^2 dr \qquad \text{(I-53)}$$

where x_i and x_j are mole fractions, W_{ij} is the intermolecular potential,

and g_{ij} the pair-distribution function of molecules i and j. In appearance Eq. (I-58) is quite similar to Eq. (I-18) for a one component syster, but evaluation of Eq. (I-58) is much more difficult.

The added complexity can be illustrated for a binary mixture. The potential energy of intermolecular force for the binary mixture consists of three terms, rather than one, reflecting the different types of molecular interaction:

$$W_N = \sum^{N_\alpha} W_{\alpha\alpha}(r_{ik}) + \sum^{N_\beta} W_{\beta\beta}(r_{ik}) + \sum^{N_\alpha, N_\beta} W_{\alpha\beta}(r_{ik}) \qquad (I\text{-}59)$$

Also, there are now four triplet distribution functions, viz., $g^{(3)}_{\alpha\alpha\alpha}$, $g^{(3)}_{\alpha\alpha\beta}$, $g^{(3)}_{\alpha\beta\beta}$, and $g^{(3)}_{\beta\beta\beta}$. Introduction of the superposition approximation leads to four integral equations, one each for $g^{(2)}_{\alpha\alpha}$ and $g^{(2)}_{\beta\beta}$ and two for $g^{(2)}_{\alpha\beta}$. The latter become identical only for the special case of $u_{\alpha\alpha} \equiv u_{\beta\beta}$; otherwise, for the general case, the difference between the two predicted values of $g^{(2)}_{\alpha\beta}$ measures the error caused by the superposition approximation.

b. Cell-Model Theory. The methods and procedures by which the cell model has been modified for mixtures are discussed in the following paragraphs. This theory is one of several "mixture-rule" theories that have been recently developed, having as their principal goal the estimation of the properties of mixtures of spherical molecules in terms of properties of characteristic pure fluids.

In cell-model theory, the "mixture rule" serves to define average molecular parameters for the mixture from which one or more mean cell potentials can be derived. This can be conveniently illustrated by

examination of the one- and two-fluid models proposed by Prigogine (P1, P5, P6, P7, S3).

The one-fluid approximation, also known as the "random-mixing approximation," defines a general cell potential function for the mixture by

$$\omega_m(r) = \sum x_\alpha x_\beta \omega_{\alpha\beta} \qquad (\text{I-60})$$

where $\omega_{\alpha\beta}$ is the potential function for interaction between molecules α and β. Physically Eq. (I-60) is equivalent to assuming that the liquid is composed of uniform cells with the parameters ε_m^* and d_m determined by the average environment. This implies a regular lattice at 0°K with all nearest neighbor distances identical. For example, in a binary mixture the potential energy is taken to be the sum of 1-1, 1-2, and 2-2 interactions in the appropriate (random) proportions. Thus the reference fluid is seen to be a single substance of N molecules interacting with the composition-dependent cell potential given by Eq. (I-60). The corresponding excess free energy for the binary mixture with $\alpha \equiv 1$ and $\beta \equiv 2$ is

$$f^E = \frac{1}{2}\left[\omega_m(0) - x_1\omega_{11}(0) - x_2\omega_{22}(0)\right] - kT \ln \frac{\psi_m}{\psi_{11}^{x_1}\psi_{22}^{x_2}} \qquad (\text{I-61})$$

where

$$\psi_m = \int_{\text{cell}} \exp\left\{-\left[\omega_m(r) - \omega_m(0)\right]/kT\right\} 4\pi r^2 dr \qquad (\text{I-62})$$

and $$\varepsilon_m^* = x_1 \varepsilon_{11}^* + x_2 \varepsilon_{22}^* \qquad (I\text{-}63)$$

$$d_m = x_1 d_{11} + x_2 d_{22} \qquad (I\text{-}64)$$

The double subscripts, e.g., in d_{11}, refer to the properties of the pure fluids.

The two-fluid approximation describes the properties of a c-component mixture in terms of a set of c reference fluids. The cell potential functions of the reference fluids are given by

$$\omega_\alpha = \sum_\beta x_\beta \omega_{\alpha\beta} \qquad (I\text{-}65)$$

This approach, which is also known as the "semi-random-mixing approximation," is an improvement over the one-fluid approximation, for the following reasons. If two molecules are of different size, it is obviously an oversimplification to assume that even at 0°K they pack into a regular lattice with a single lattice parameter d_m. Thus, the uniform cell model magnifies the effect of differing molecular size beyond its real importance, and the energy so obtained represents an upper limit. The two-fluid solution was therefore developed to enable attainment of a lower potential energy by allowing lattice irregularities.

Considering the binary mixture again, the two-fluid model assumes that there are two kinds of cells, one for type-1 molecules with parameters d_1 and ε_1^* determined by the average environment of type-1

molecules, and another for type-2 molecules with d_2 and ε_2^* similarly determined. Thus, for type-1 cells the energy is the sum of 1-1 and 1-2 interactions in the proportion x_1/x_2 of type-1 and type-2 nearest neighbors to a type 1 molecule. The cell sizes are chosen so as to minimize the free energy. Then the excess free energy of the mixture is the sum of the free energies of transferring x_1 type-1 molecules from the pure state to type-1 cells in the solution and x_2 type-2 molecules to type-2 cells in the solution. The resulting expression for the excess free energy is

$$f^E = x_1\left[\frac{w_1(0)-w_{11}(0)}{2} - kT\ln\frac{\psi_1}{\psi_{11}}\right] + x_2\left[\frac{w_2(0)-w_{22}(0)}{2} - kT\ln\frac{\psi_2}{\psi_{22}}\right] \qquad \text{(I-66)}$$

where $$\psi_\alpha = \int_{\text{cell}} \exp\left\{-\left[w_\alpha(r)-w_\alpha(0)\right]/kT\right\} 4\pi r^2 dr, \quad \alpha = 1, 2 \qquad \text{(I-67)}$$

and the force constants are

$$\varepsilon_\alpha^* = x_\alpha \varepsilon_{\alpha\alpha}^* + x_\beta \varepsilon_{\alpha\beta}^*, \quad \beta \neq \alpha, \ \alpha, \beta = 1, 2 \qquad \text{(I-68)}$$

$$d_\alpha = x_\alpha d_{\alpha\alpha} + x_\beta d_{\alpha\beta}, \quad \beta \neq \alpha, \ \alpha, \beta = 1, 2 \qquad \text{(I-69)}$$

The application of cell-model theories of solution, and in particular the two-fluid theory, has achieved a reasonable degree of

success. Using this theory, Prigogine (P3) was able to demonstrate theoretically for the first time that in mixtures of nonpolar molecules of the same size, e.g., neopentane and carbon tetrachloride, the excess enthalpy is positive and the excess volume negative. Previously, all solution theories had predicted that the two quantities must have the same sign.

Nevertheless the cell-model approach does suffer from a serious deficiency, which is common to the majority of "mixture-rule" theories. The problem lies in the breakdown of the random-mixing assumption in mixtures composed of molecules of different size (B2). To accentuate the effect of molecular size differences, Salzburg (S4) considered a mixture of hard spheres. He found that, upon mixing at constant temperature and pressure the one- and two-fluid theories possessed singularities; for example, for a binary mixture the one-fluid theory predicted mixture properties identical to those of a pure fluid of large spheres at all compositions, and the two-fluid theory was representative of an ideal mixture of molecules of diameter d_{12} and d_{22}. Thus for a hard-sphere mixture, each theory is singular in the limit of all small molecules.

B. Fluidized-Bed Phenomena

The term "fluidization" designates the phenomenon in which discrete solid particles are levitated by drag forces resulting from upflow of fluid through the interparticle space. The resulting "fluidized bed" displays a free upper surface and other bulk physical properties characteristic of single-phase true liquids. Fluidized beds possess several desirable attributes such as large solid-fluid interfacial area, relatively uniform heat distribution throughout the bed and ease of solids handling. The industrial importance of gas-fluidized beds as catalytic reactors has led to a large number of theoretical and experimental investigations of fluidization. However, its underlying fluid-dynamic mechanism has not yet been fully explained, and the empirical expressions established by various investigators do not form a consistent framework.

As in the theoretical description of real liquids, there are two possible approaches to the development of a general fluidized-bed theory. One is, from observations of the phenomenalistic behavior of the bed, to deduce interrelations between the macroscopic variables that characterize the system; this corresponds to the establishment of a thermodynamic-like framework. The alternative approach is to induce, from the dynamic behavior of the individual particles, the general properties of the fluid bed; this is comparable to the development of a kinetic theory of fluidized beds. Of these two, the thermodynamic approach has received primary attention, since in most instances reactor design requires only a factual knowledge of the

specific attributes of the bed rather than complete understanding of them. In addition, even under the most restrictive assumptions the fluid dynamics of a multibody system has not yet proven amenable to solution, and a fluidized bed exhibits nonuniformities in behavior which further complicate the problem. Nevertheless it appears that useful information can be gained from a rudimentary analysis of the multibody system.

1. General Characteristics of Fluidized Beds

The most obvious physical variable controlling fluidized-bed behavior is the upward velocity of the fluid medium. Many observable properties of the bed can be specified as a function of the fluidizing velocity, subject to still uncorrelated effects of other parameters such as bed diameter and the density difference between the solid and fluid phases.

There are well defined boundaries to fluidized-bed behavior. At the lower limit a minimum fluidizing velocity exists for which the pressure drop through the pre-existing fixed bed becomes just sufficient to support the weight of the particles; at this point

$$\Delta P = \Delta\rho (1-\varepsilon_{mf})\, g\, L \qquad (I\text{-}70)$$

with $$\Delta\rho \equiv \rho_s - \rho$$

Here ΔP is the pressure drop across the bed, ρ_s is the solid-particle density, and ρ is the fluid density; ε_{mf} is the minimum fluidized-bed void-fraction, g is the local gravitational acceleration, and L is the bed height. [Eq. (I-70) holds throughout the fluidization regime when

the minimum void-fraction ε_{mf} is replaced by the void-fraction function ε.]

An upper limit to fluid-bed behavior is furnished by the terminal velocity of fall of single particles, which for spheres is given by

$$C_D u_t^2 = 4 \Delta\rho g d / (3\rho) \qquad (I\text{-}71)$$

where C_D is the particle drag coefficient, a function of Reynolds number and particle shape and roughness; u_t is the particle terminal velocity, and d is the particle diameter. The fluid bed cannot exist for velocities greated than the particle terminal velocity, and unless restrained the bed is "transported" out of the column. It should be noted that the existence of the fluidized state between "fusion" at low system energy and "evaporation" at high system evergy seems strikingly similar to liquid behavior. In this context, the two approaches to fluidized-bed theory mentioned previously can to some extent be viewed as extrapolations either from fixed-bed behavior or from single particle behavior, much as current liquid theories are seen to be solid-like or gas-like.

The behavior of fluidized beds has been found to fall into two general catagories. Systems in which the density difference between phases is small usually exhibit relatively uniform expansion behavior as flow velocity is increased and are said to be "particulately" or "uniformly" fluidized. Systems in which the density difference is large are dynamically unstable; such systems are subject to gross nonuniformities in particle distribution and flow behavior; and hence

are "aggregatively" or "nonuniformly" fluidized. A "dense phase" and a "lean phase" can be identified, and in this respect the aggregative system is analogous to a partly-evaporated liquid. This nonuniform behavior is closely related to several other variables, e.g., local gravitational acceleration, bed height-to-diameter ratio, particle roughness, and distribution of flow of the fluidizing medium. In particular, Simpson and Rodger (S5) have shown that nonuniformity in a gas-solid system can be considerably diminished by decreasing the phase density difference through gas pressurization. The mathematical analysis of aggregative phenomena by Pigford and Baron (P8) has emphasized the central role of inertia effects, which are directly related to the density difference between phases.

Because this investigation has the purpose of exploring applications of the theory of liquids that will elucidate fluid bed phenomena, our interest here will be focused primarily upon uniformly-fluidized systems, and upon those attributes most directly analogous to liquid behavior.

2. Specific Fluidized-Bed Phenomena

The macroscopic basis for viewing fluidized-bed behavior as similar to that of a liquid has been given above. On a microscopic level the similarity in behavior of particles in a uniformly-fluidized bed and that of liquid molecules is also quite evident; in both cases the particles tend to vibrate around quasi-equilibrium lattice sites, with random diffusion between sites. In this regard, numerous

investigators (S8, M8, L6) have observed that the extent to which particle motion in a fluid bed can be described by its vibratory-migration character is strongly dependent upon experimental conditions.

It is pertinent to review the general nature of those fluidized-bed properties which should serve to define most clearly the extent of the analogy with true liquids: volume expansion, viscosity, self diffusion, multiphase behavior, and surface tension. The first four of these have received considerable attention and will be discussed in the following paragraphs; surface tension will be reserved for later discussion.

a. Volume Expansion. The initial attempt to correlate the data on fluidized-bed expansion was based on the pressure-drop relation for fixed-beds developed by Kozeny (K6). Postulating a "tortuous-channel" model for streamline fluid flow through the bed, he obtained the relationship:

$$\Delta P/L = k_1 \mu U s^2 (1-\epsilon)^2/\epsilon^3 \qquad (I\text{-}72)$$

where s is the specific particle surface; k_1 is a constant, approximately 5.0; μ is the fluid viscosity; and ϵ is the void volume, i.e., fraction of bed volume not occupied by particles. The variable U is the superficial flow velocity, that is, volumetric flow rate per unit bed area. Setting this equal to the generalized form of Eq. (I-70), to introduce the effective mass of the bed, yields:

$$(1-\epsilon)/\epsilon^3 = \Delta\rho g/(k_1 \mu U s^2) \qquad (I\text{-}73)$$

This equation furnishes relatively good agreement with experimental data.

Jahnig (J1) has suggested the alternative approach of extending the single-particle free-fall expression, Eq. (I-71), to particulate fluidized beds, and even to fixed beds, by appropriate interpretation of the drag coefficient. Essentially he postulates that the intersticial flow velocity past a particle in a multi-particle system remains equal to its terminal velocity. The drag coefficient is then modified to reflect the diminished flow area

$$C_B = C_D / A^2 \qquad (I\text{-}74)$$

Here C_B is the drag coefficient in the bed, C_D is the drag coefficient for free fall, and A is the fraction minimum area in the direction of fluid flow. He also assumed that the bed expands in a geometrically-uniform manner; thus, for spheres with a cubic packing arrangement

$$A = 1 - 1.21 (1 - \varepsilon)^{2/3} \qquad (I\text{-}75)$$

This relationship has been found approximately to fit the data for spheres over the entire range from single particles to the packed bed, in viscous, turbulent, or transition region flow.

Most expansion data have been correlated by a simpler relationship derived from dimensional considerations. Richardson and Zaki (R3) have established the following dimensionless form which applies for either viscous or turbulent fluidizing flow

$$U/U_i = f\left(\rho U_i d/\mu, \varepsilon, d/D\right) \qquad \text{(I-76)}$$

where U_i is the antilog of the intercept at $\varepsilon=1$ of the log U vs ε curve, and D is the overall (column) diameter of the fluidized bed. It has been empirically determined that this functionality can be represented by

$$U/U_i = \varepsilon^n \qquad \text{(I-77)}$$

with $$n = g\left(\rho U_i d/\mu, d/D\right) \qquad \text{(I-78)}$$

Further, if either the viscous or inertia forces can be neglected, i.e., for other than transition region flow, n becomes merely a function of d/D. Other investigators have concluded that for $d/D \leq 10$ this dependence is slight, i.e., "wall effects" are negligible. This relationship has been found to be equally valid for liquid-solid systems under fluidized and under sedimenting conditions. For small d/D, Richardson proposed that n=-4.65. The data of other investigators do not all support this figure; for example, Jottrand (J2) suggested a value of -5.63.

Bena' (B3) analyzed his volumetric data on uniformly-fluidized spherical particles somewhat differently. By dimensional analysis he arrived at the general functionality:

$$f(Re, Ar, \varepsilon) = 0 \qquad \text{(I-79)}$$

where the Reynolds' number Re is here defined $\rho Ud/\mu$, and the Archimedes' number Ar equals $\rho\Delta\rho gd^3/\mu^2$. From experimental data on two water-fluidized systems, 126μ glass beads and 1380μ polymethylmethacrylate spheres, he empirically established for the laminar regime:

$$\varepsilon^{4.65} = 12.8\, Re\, Ar^{-0.89} \qquad (I\text{-}80)$$

He restricted his definition of the purely laminar region to $Ar \leq 30$.

b. Viscosity. Nearly all fluidized-bed viscosity measurements have been made in gas-fluidized beds. Such measurements have the advantage of a negligible viscous contribution from the fluid phase, but the true nature of the viscous effect tends to be masked by gross convection of the particles.

An article by Matheson, Herbst, and Holt (M2) seems to provide the first description and measurement of fluidized-bed viscosity. Their interest in this property was related to the possibility of using it to characterize the flow properties of the bed. They utilized a Stormer-type paddle viscometer, whose dimensions were only slightly smaller than the gas-fluidized bed, to investigate the dependence of viscosity upon superficial velocity, particle diameter, and particle density. Because of the large paddle size bulk acceleration of the particles was involved in addition to the normal shear properties.

Shuster and Haas (S6) recently conducted viscosity measurements similar to those of Matheson, Herbst, and Holt, but employing a

Stormer-type paddle of much smaller size relative to the bed. They found the measured viscosity to be a function of paddle size and angular velocity, particle size, density, and size distribution, and superficial velocity. They also examined the radial and axial variation of viscosity under identical flow conditions and found some nonuniformity which was strongly a function of the effectiveness of the gas distributor.

A quite different type of air-fluidized-bed viscosity measurement was performed by Daniels (D5). He measured the rate of rise and fall of metallic spheres of differing size and density when drawn through a fluidized bed by a fine thread connected by pulleys to a weight system. He found that his data for the drag coefficient of the moving sphere in 87.5 - 175μ glass-sphere beds, with the exception of some measurements subject to wall effects, could be correlated by:

$$C_D \equiv F_D / (\rho_B V_s d_s^2) = 180 (d/d_s) (V_s d/\nu)^{-0.362} (V_s^2/gd)^{-0.589} \qquad (I\text{-}81)$$

Here F_D is the measured drag force corrected for buoyancy and pulley friction, ρ_B is the bed density, V_s is the velocity of the metallic sphere, d_s is the metallic-sphere diameter, and ν is the kinetic air viscosity. Binnie (B4) then employed an empirical correlation:

$$C_D = 24/Re \cdot (1 + 0.15 Re^{0.687}) \qquad (I\text{-}82)$$

to transform Daniels results into an expression for the apparent kinematic viscosity of the bed ν_a:

$$\nu_a = 0.001 \left(K/\rho_B\right)^{0.92} \cdot d / v_s^{0.84} \qquad (I\text{-}83)$$

where κ is the bed elasticity. This relationship predicts an infinite apparent viscosity as the metallic-sphere velocity approaches zero, however, which is clearly fallacious.

c. Self Diffusion or Migration. There have been a number of experimental investigations of solids mixing in fluidized beds involving the use of tracer particles. These tracer particles may be marked in a variety of ways to distinguish them from the bulk particle properties, e.g., the particles may be irradiated, chemically impregnated, or differentiated by thermal content, color, magnetic properties, or opaqueness to X-rays. Ideally the tracer particles should be introduced in a manner that will least disturb the bed, and samples should be removed locally and continously from several points within the bed. However, most of the actual investigations have been conducted in gas- or liquid-fluidized beds in which no attempt was made to minimize the influence of convective currents, and there has been little quantitative agreement among the data of the various investigators. All the data indicate a general increase of diffusivity with increasing superficial velocity and void fraction.

The earliest quantitative data were those of Bart (B5) for air fluidization of cracking catalyst in a 3.2 cm. diameter column, using tracer particles impregnated with NaCl. The fluidized solids were fed continously into the bottom of the bed and removed from the top, while the tracer particles were injected at the approximate midpoint of the bed. Bart correlated his data for samples taken at points upstream of the injector by the diffusive-mixing relation

$$c/c_o = \exp\left(-Sx/E_s\right) \qquad (I\text{-}84)$$

Here c is the concentration of diffusing component, c_0 is the concentration

of diffusing component at injection point, S is the superficial solid velocity, x is the upstream distance of sample point relative to injection point, and E_s is the solid-diffusion coefficient. For 115μ cracking catalyst, this relation yielded diffusivities of 1.3 to 5.0 kg/m.sec. for superficial gas velocities of 0.1 to 4.0 m/sec. respectively, and indicated that the coefficient of self diffusion was directly proportional to the superficial gas velocity.

Massimilla and Bracale (M4) conducted a similar study with 0.7 mm. glass beads fluidized by air in a 9 cm. column with colored tracer particles added at the top and later sampled at a single bed height. They also found the diffusivity to be proportional to gas velocity and to the percentage expansion, $(L-L_0)/L_0$, but their values were a factor of 15 larger than those of Bart.

Kennedy and Bretton (K7) measured the axial diffusion of closely-sized glass-bead systems of 1.0 and 2.0 mm. diameter and 1.2 mm. lead spheres. The sampling procedure utilized a 0.008 in. nylon-filament screen to divide the column into two parts. In transient-type experiments the extent of intermixing between equal numbers of marked glass spheres, colored by gamma irradiation, and normal spheres was ascertained; the two groups were initially segregated by the screen. Steady-state-type measurements determined the equilibrium axial size gradients. Using Fick's law to interpret the diffusion phenomena, the diffusivities were found to be proportional to the superficial fluidizing velocity excess over its value at the minimum-fluidization point.

Wilde (W1) performed a photographic study of glass-sphere beds

in which the index of refraction of the fluidizing fluid was matched to that of the spheres. He found that the 2.4 - 5.0 mm. particles traveled in groups, and tended to have a greater velocity component parallel to the direction of fluid motion. The mean speed of the particles was seen to be proportional to the superficial fluidizing velocity.

In a recent theoretical study Houghton (H6) developed a Markov theory for particle diffusion in homogenous fluidization. The model expresses the force balance on a single fluidized particle as a nonlinear Langevin equation; it accounts for both particle-fluid and particle-particle interactions. Assuming a Gaussian distribution of particle velocities, the Uhlenbeck-Ornstein stochastic problem is solved to yield particle-diffusion equations in velocity and configuration space. Comparing the resultant single-particle-model diffusivities with experimental values, however, shows that the theoretical values are an order of magnitude too low, even if the fluctuation energy approaches that of the local mean flow. Houghton attributed the high diffusion rates to spacial variations in mean velocity and random macroscopic turbulence. Accordingly, he generalized his model to include such effects, but did not completely develop an expression for such multiple-particle diffusion effects.

d. Multiphase Behavior. There has been very little study of fluidized-bed multiphase behavior. In the related process of classification during sedimentation, the occurence of segregation has been attributed to differences in Stokes settling velocities of the particles in the fluid-solid medium. That is, each particle is assumed to settle

as it would in a uniform fluid having the average density and viscosity of the suspension. Their relative velocities are then given by

$$\frac{u_2}{u_1} = \sqrt{\left(\frac{\rho_2-\rho}{\rho_1-\rho}\right)\left(\frac{d_2}{d_1}\right)\left(\frac{C_{D_1}}{C_{D_2}}\right)} \qquad (I\text{-}85)$$

where the subscripts denote the properties of the two types of particles. In an infinitely long column or when suspended in a column by counter-current fluid flow perfect separation should occur. However, in a fluid bed the vibratory motion of the particles leads to the onset of diffusive particle motion, as discussed above, and this phenomenon partially offsets the tendency toward segregation. As a result, an equilibrium is established, characterized by either strong or weak phase separation depending upon whether the Stokes segregation or the diffusive-remixing tendency predominates.

Hoffman, Lapidus, and Elgin (H5) observed the occurrence of partial phase segregation in their experiments with glass beads fluidized by water. They stated that the behavior of a system composed of particle types possessing nearly identical properties "suggests strongly the analogous behavior of liquid mixtures which may be partially or completely immiscible and in which the degree of miscibility is determined by the temperature (here in the form of fluid velocity or energy)."

3. Liquidlike Theories of Fluidization Phenomena

Many investigators have commented on the similarity between liquid and fluidized-bed behavior, e.g., Hoffman et al, but only three have made specific attempts to interpret fluidized-bed phenomena on this basis. The fundamental problem in postulating a kinetic theory of fluidization is to establish a relation for the mean kinetic energy of particle motion, i.e., a variable analogous to thermal energy kT. The approach of the three sets of investigators to this problem, including the supporting experimental data of the Japanese and German groups will be discussed below.

a. Work of Furukawa and Ohmae (F2). The essence of the theoretical approach of these investigators was that the overall volumetric behavior of a fluidized-bed is the resultant of individual "volume vibrations" of particle subgroups, in response to slight variations in the fluid-flow distribution. The dynamic-equilibrium volume of this vibration is established by a balance between the "expansive" force per unit volume of fluid drag, of the form given by Eq. (I-72), and the "contractive" force per unit volume given by Eq. (I-70). When these forces become momentarily out of balance, a volume vibration occurs, and the potential energy of this vibration is taken to be:

$$\Phi = l_e \int_{V_e}^{V} (\rho_e - \Delta P/L)\, dV \qquad \text{(I-86)}$$

where l_e is a characteristic length of the equilibrium cell volume, ρ_e is the contractive force per unit volume, $\Delta P/L$ is the expansive force per unit volume, and V_e is the equilibrium volume. The volumetric dependence

of the potential energy is schematically indicated in Figure I-3, with superficial fluidizing velocity as a parameter (U_2 being larger than U_1).

Furukawa and Ohmae next related bed void fraction to interparticle distance by use of Ergun's (E6) cylindrical-channel model, developed for fixed beds, and substituted the resulting expression into the relation for the average kinetic energy of a harmonic oscillator:

$$\overline{KE} = a_p^2/4 \cdot (d^2\phi/dr^2)_{r_e} \qquad (I\text{-}87)$$

where a_p is the amplitude of particle oscillation, and r is the interparticle distance. Based upon their experimental data, the form of the resulting expression was

$$\overline{KE} = (\text{const})\,\mu U \qquad (I\text{-}88)$$

Hence μU represented the fluidized-bed variable analogous to thermodynamic temperature.

To support their proposal they succeeded in correlating experimental data on fluidized-bed expansion, viscosity, surface tension, and miscibility, by substituting μU for kT in various empirical relationships that have been developed for the analogous liquid properties. The nature of their experimental work and the resulting correlations is briefly described in the following paragraphs.

The experiments were performed in a 6 cm. i.d. glass tube using particles in the 160 - 750 μ size range. The expansion and viscometry measurements were conducted on air-fluidized polyvinylacetate

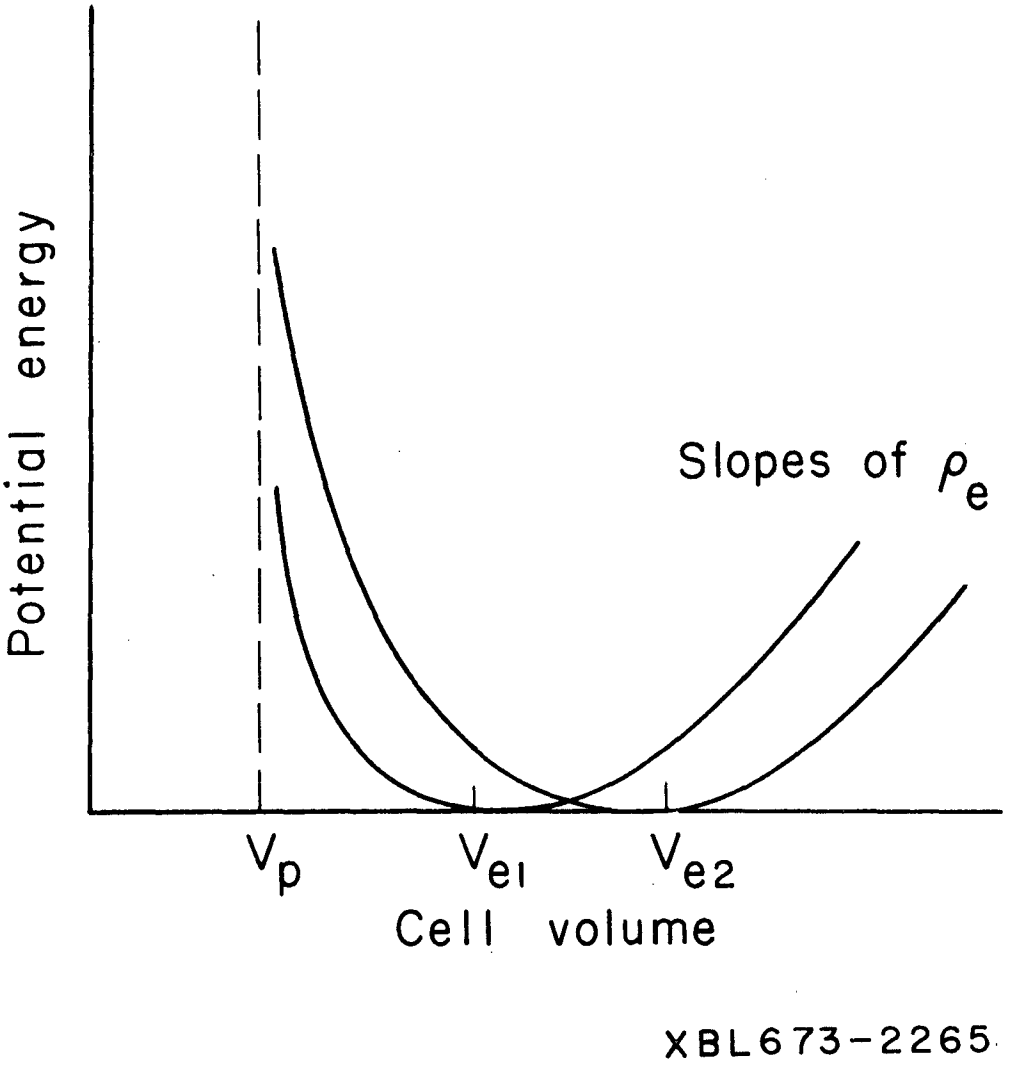

Fig. I-3. Schematic of Furukawa and Ohmae's volume-vibration potential energy.

beds, while the surface tension and miscibility experiments employed water fluidization of sand, with some miscibility data obtained for a charcoal--sand system. The specific experiments were as follows:

(i) Expansion. The expansion data were correlated by the use of three liquidlike relationships, each applicable to a different expansion range:

$$V/V_{mf} = 1 + \delta_f (U-U_{mf}) + \delta_f' (U-U_{mf})^2 + \cdots \quad , \; V/V_{mf} < 1.5 \qquad (I\text{-}89)$$

$$1 - (V_{mf}/V)^{1/3} = G_f U^{1/2} \quad , \quad 1.5 < V/V_{mf} < 4.0 \qquad (I\text{-}90)$$

$$\frac{V}{V_{mf}} = \left(\frac{V_{max}}{V_{mf}}\right) - \left(\frac{V_{max}}{V_{mf}} - 1\right)\left[1 - \frac{U-U_{mf}}{U_{max}-U_{mf}}\right]^{1/3.1} \quad , \; \frac{V}{V_{mf}} > 4.0 \qquad (I\text{-}91)$$

where δ_f, δ_f', G_f, V_{max}, U_{max} are empirical constants. The first of these relations is clearly a power-series fit; the second is related to free-volume theory; and the third is analogous to an empirical equation developed from the principle of corresponding states.

(ii) Viscosity. The viscosity data were obtained using a modified Stormer viscometer, and agree with the results of Matheson, Herbst, and Holt (M2) and Diekmann and Forsythe (D6). The correlating equation employed was similar to that developed by Andrade (A2) for liquids:

$$\mu_f = F_f \exp(-E_f/U) \qquad (I\text{-}92)$$

where F_f and E_f are empirical constants for a given system with E_f directly proportional to d_p^2. The viscosity data also displayed an inverse proportionality to free volume, $V - V_{mf}$, as suggested for liquids by Batschinski (B6).

(iii) Surface Tension. Furukawa and Ohmae are the only investigators to have explored experimentally this property of fluidized beds, although the passage of bubbles through aggregatively-fluidized beds has offered ample evidence of the existence of some form of stability at interfaces between empty fluid and the fluid-solid mixture. Their measuring technique consisted of determining the number and shape of air bubbles injected at known volumetric rates into a water-sand fluidized system. They correlated their data by the relation

$$\frac{\sigma_f}{\sigma_{mf}} = \left(\frac{V_{mf}}{V}\right)^{2/3}\left[1 - \frac{U - U_{mf}}{U_{max} - U_{mf}}\right] \qquad (I\text{-}93)$$

where σ_{mf} is an empirical constant of the system.

(iv) Miscibility. Miscibility data were obtained for several mixtures of sands of two different diameters, and for sand and charcoal which differed both in density and diameter. In the sand-sand system, segregation increased with increasing superficial fluidizing velocity, while in the charcoal-sand system the inverse effect was observed. Furukawa and Ohmae commented that the former behavior is similar to solvation phenomena in liquids, while the latter corresponds to polar-nonpolar interactions. They correlated their data by

$$\ln(X_1/X_2) = p + q/U \qquad (I\text{-}94)$$

where p and q are empirical constants.

b. Work of Schügerl, et al (S7). These investigators analyzed their experimental data on fluidized-bed viscous effects so as to enable comparison with the Eyring rate theory of viscosity (E5). They thereby established a thermal-energy function for the fluidized bed.

A rotating-cylinder viscometer was employed in the experimental investigation. The outer cylinder was held fixed, and both inner and outer cylinder surfaces were roughened by affixing a layer of 500μ glass spheres. X-ray measurements were made concurrently at the mean level of the cylinder in order to assess the extent and influence of nonuniformities in the fluidization.

The nature of their results for "stably" fluidized beds is illustrated by Figures I-4 - I-6. These figures present different aspects of a stress-shear curve for a 110μ glass-sphere bed fluidized by air. Figure I-4 displays the nature of the results obtained in the bob rotational-velocity range employed in the current investigation. They obtained measurements over a much larger rotational-velocity range, however, and Figure I-5 gives the overall form of the flow curve. Obviously, the curve does not tend to approach linearity at $\omega \sim 30$ min^{-1} as might be suspected from Figure I-4. In fact, its general nature cannot be truly inferred from data restricted to low bob rotational velocities ($\omega \leq 60$ min^{-1}).

Figure I-6 shows the excellent fit to their data achieved by Schügerl, et al using a hyperbolic-sine function:

$$\omega(\tau) = A_0 \sinh(B_0 \tau) \qquad (I\text{-}95)$$

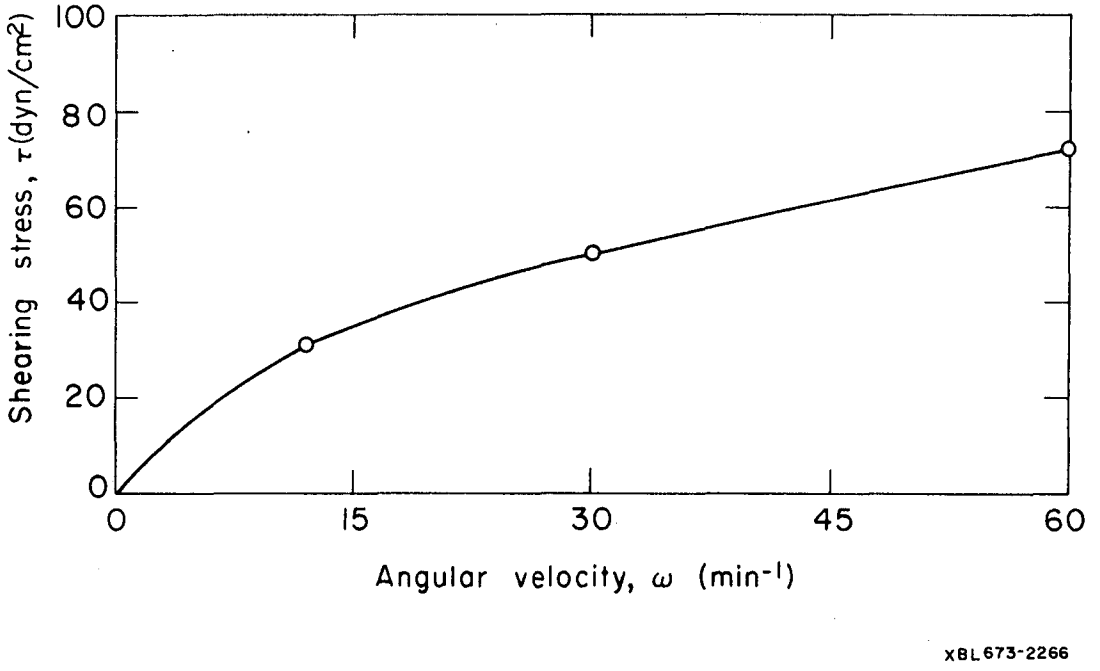

Fig. I-4. Schügerl et al. Spindle-rotation curve $\omega(\tau)$ for 110μ quartz sand over the 0-60 RPM rotation-rate range (S7).

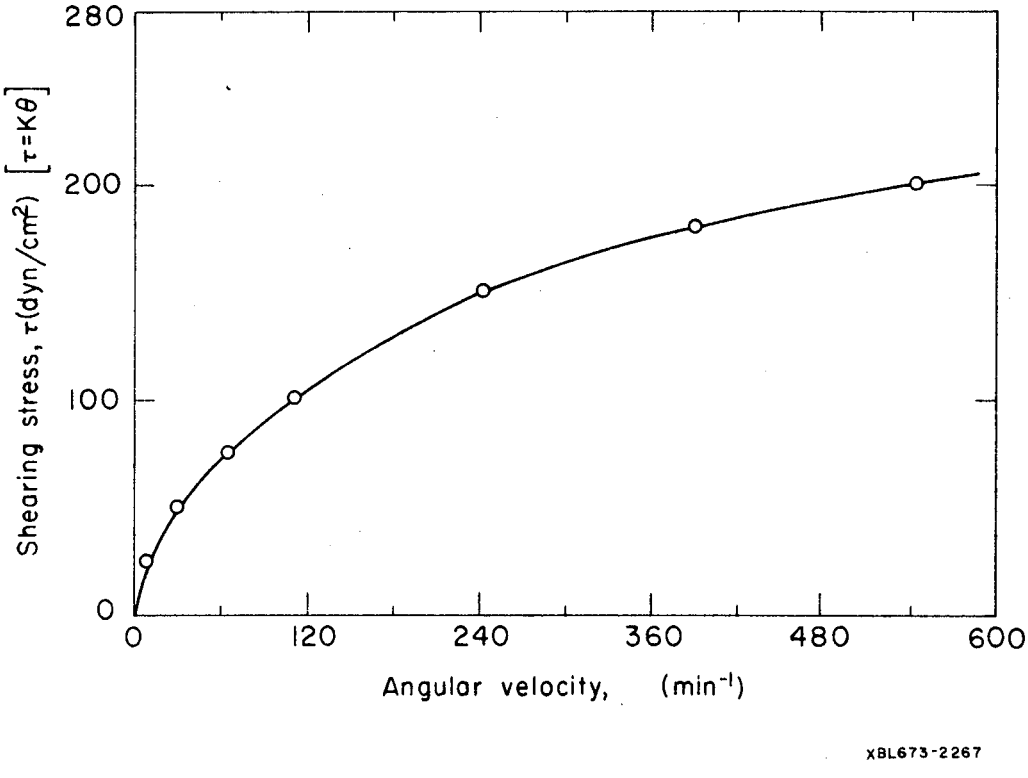

Fig. I-5. Schügerl et al. Spindle-rotation curve $\omega(\tau)$ for 110μ quartz sand over the entire ω range [S7].

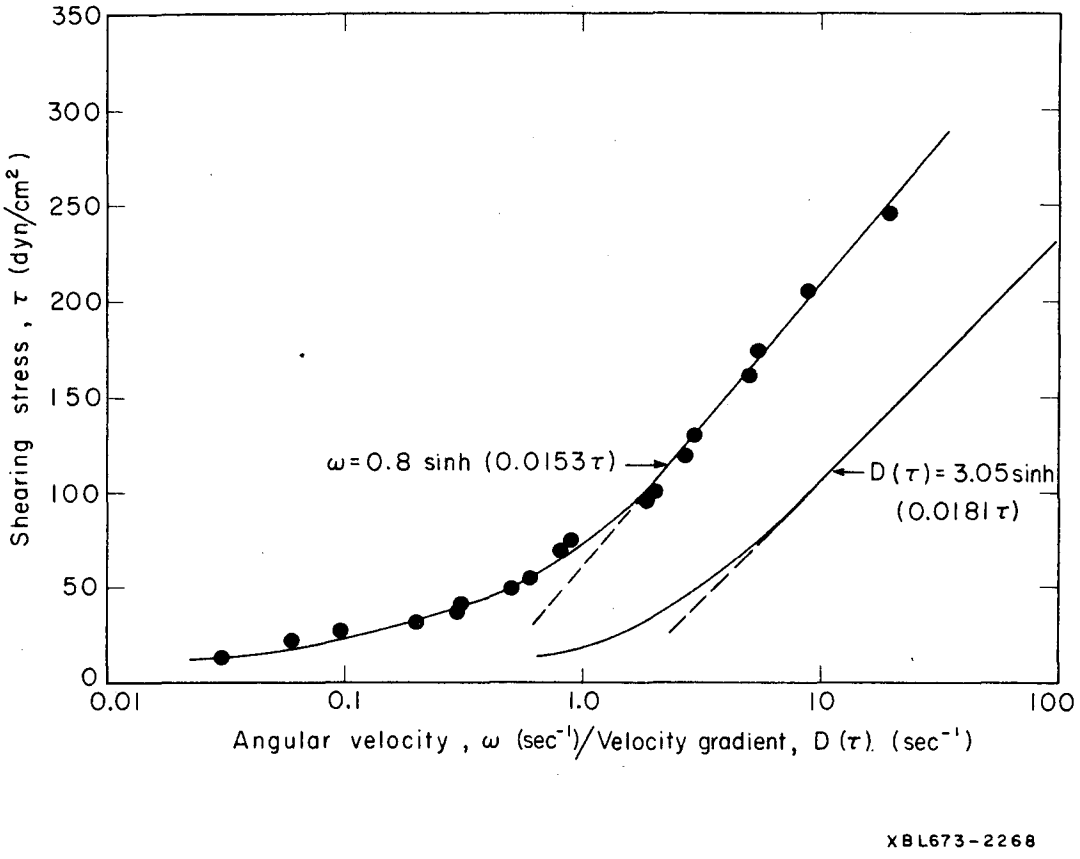

Fig. I-6. Schügerl et al. Spindle-rotation curve $\omega(\tau)$, and the related stress curve $D(\tau)$ for sharp-edged 110μ quartz sand (S7).

where ω is the shear rate which results from an imposed shear stress τ, and A_0 and B_0 are experimentally determined constants. The method of Pawlowski (P9) was then employed to obtain the corresponding friction law, which was found to be also of hyperbolic-sine form, e.g.,

$$D(\tau) = A_1 \sinh (B_1 \tau) \qquad (I\text{-}96)$$

where $D(\tau)$ is the strain function, i.e., velocity gradient. The parameters A_1 and B_1 were fit by:

$$A_1 = \alpha_0 \exp (-\sigma_0 B_1 d^{3/2}) \qquad (I\text{-}97)$$

$$B_1 = C_4 d^2 / [U_{mf}(U-U_{mf})] \qquad (I\text{-}98)$$

where C_4, a function of particle shape, equals 0.325 for glass spheres.

The effective viscosity is then given by

$$\eta = \tau / D(\tau) \qquad (I\text{-}99)$$

which at low rotational velocities approaches a Newtonian limit of $(AB)^{-1}$. The resulting effective viscosity for the flow system considered in the figure is 18.1 poise. (Note: when multiplied by their calibration constant, 0.67, the corrected value of viscosity for this case is 12.1 poise.)

The form of Eq. (I-99) is identical to that of Eyring's rate-theory

expression for viscosity,

$$D(\tau) = 2ak_0'/\delta_0 \sinh\left[aF/(2n\delta_0 kT)\right] \qquad (I\text{-}100)$$

Here a is the diffusion "jump-distance", k_0' is the frequency of diffusion jumps in the absence of external forces, δ_0 is the distance between molecular layers (quasi-crystal), and n is the particle number density. F, the diffusive force per unit area, equals shear stress for a Newtonian fluid. By comparing Eqs. (I-96) - (I-98) to (I-100), Schügerl, et al established an expression for the "thermal energy" of a fluidized bed

$$kT = a/(2n\delta_0) \cdot U_{mf}(U-U_{mf})/(C_4 d^2) \qquad (I\text{-}101)$$

Some doubt is raised, from the theoretical and experimental studies of the present paper, that $(U-U_{mf})$ best represents the system energy.

Schügerl et al also abstracted an expression for fluidized-bed self diffusion from their viscosity correlation. In Eyring's development the self-diffusion coefficient of a liquid is given by $D = k_0' \delta_0^2$; a comparison of Eqs. (I-96) and (I-100) yields the following fluidized-bed relation for k_0':

$$k_0' = \delta_0 A_1/(2a) = (\delta_0/2a)\,\alpha_0 \exp\left[\frac{-C_4 \tau_0 d^{7/2}}{U_{mf}(U-U_{mf})}\right] \qquad (I\text{-}102)$$

Schügerl noted that the diffusion data of May (M3) exhibited this general form. i.e., a linear dependence of log D on the reciprocal of $(U-U_{mf})$.

c. Work of Ruckenstein (R4). A recent theoretical study by Ruckenstein was concerned primarily with the influence of particle motion upon mixing in the fluidized phase, rather than in establishing a liquidlike theory of fluidization. However, it furnishes a relatively complete and ingenious extension of single-particle theory into a multiparticle framework, and illustrates the complex character of the particle kinetic energy. Ruckenstein indicated that his theory can be used to modify liquid theory for application to fluidized-bed behavior, but made no attempt to do so.

Ruckenstein assumes that, as originally postulated by Schügerl et al, (S7) the energy for particle support remains equal to its value at the point of incipient fluidization, $H_{s,mf}$. Thus the rate of energy dissipation due to particle motion is given by

$$H_m = H - H_{s,mf} = (U - U_{mf})\Delta P \qquad (I\text{-}103)$$

$$= (U - U_{mf}) g h (1 - \bar{\varepsilon}) \Delta\rho$$

This particle motion is assumed to be a unidimensional harmonic oscillation in the vertical direction, about an equilibrium position or "lattice site." The net rate of energy transferred from the fluid to the particles during this motion is taken to be proportional to the average particle kinetic energy $\rho_s d^3 \overline{v^2}/\tau'$, where $\overline{v^2}$ is the mean-square oscillation velocity and τ' is the oscillation period. This rate of energy transfer is equated to the rate of energy dissipation in the fluid phase; hence,

$$N \rho_s d^3 \overline{v^2}/\tau' \propto (U - U_{mf}) g h \Delta\rho (1 - \bar{\varepsilon}) \qquad (I\text{-}104)$$

where N is the total number of particles in the bed, equal to $(1-\bar{\varepsilon})V/v_p$.

Ruckenstein next considered the equation of motion of a single particle in a fluid:

$$d\vec{v}/dt = \Delta\rho\vec{g}/\rho - (3C_D\rho)/(4\rho_s d)|\vec{w}|\vec{w} - m_a(\rho/\rho_s)d\vec{w}/dt \qquad (I\text{-}105)$$

where $\vec{v}$ is the particle velocity, $\vec{w}$ the relative velocity between fluid and particles, and m_a is a factor which when multiplied by $(\pi/6)\rho d^3$ equals the "apparent mass." The left term represents the particle acceleration and the three terms on the right relate respectively to buoyant, drag, and inertia effects. By a mean-value type of evaluation of this differential equation Ruckenstein was able to establish a second relation between $\overline{v^2}$ and τ', which with Eq. (I-104) enabled solution for these two quantities. Of more interest to Ruckenstein than τ', however, is the variance of the void fraction, $\sigma_\varepsilon^2=(\varepsilon-\bar{\varepsilon})^2$ where $\bar{\varepsilon}$ is the mean void fraction of the bed, and ε is the instantaneous void fraction in the vicinity of a particle during its vibration. The mean deviation σ_ε is related to τ' by

$$\tau' \propto \mathcal{L}/(\overline{v^2})^{1/2} = (\partial\mathcal{L}/\partial\varepsilon)_{\bar{\varepsilon}}\,\sigma_\varepsilon/(\overline{v^2})^{1/2} \qquad (I\text{-}106)$$

where $\mathcal{L}$ is the characteristic length of the "atmosphere" around the vibrating particle.

The final expressions developed by Ruckenstein for $\overline{v^2}$ and σ_ε are quite complex, e.g.,

$$\overline{v^2} \propto g\sqrt{d}\left(1-\frac{U_{mf}}{U}\right)\left(\frac{\Delta\rho}{\rho_s}\right)\left(\frac{\rho_s+m_a\rho}{\rho}\right)^{1/2}\left|\frac{\partial C_s}{\partial\varepsilon}\right|_{\bar{\varepsilon}}^{1/2}\left(\frac{\partial\mathcal{L}}{\partial\varepsilon}\right)_{\bar{\varepsilon}}^{1/2} \qquad (I\text{-}107)$$

and

$$\sigma_\varepsilon \propto \left(1-\frac{U_{mf}}{U}\right)\frac{g d^{3/2}}{U^2}\left(\frac{\Delta\rho}{\rho_s}\right)\left(\frac{\rho_s+m_a\rho}{\rho_s}\right)^{3/2}\left|\frac{\partial C_B}{\partial\varepsilon}\right|_{\bar{\varepsilon}}^{-3/2}\left(\frac{\partial\varphi}{\partial\varepsilon}\right)_{\bar{\varepsilon}}^{-1/2} \quad \text{(I-108)}$$

The expression for $\overline{v^2}$ should prove useful for a kinetic theory of fluidized particle motion and σ_ε relates the effect of this motion to fluid phase mixing.

II. THE PROBLEM CHOSEN FOR STUDY

The premise of this investigation is that the similarity between particulately fluidized beds and liquids is sufficient to justify the employment of the latter as a model for the former. Such a possibility has been expressed previously (F2, S7, R4), but a complete and self-consistent treatment has not been effected. In this chapter aspects of the similarity between the two systems are considered, and the scope of the study is defined.

A. Phenomenological Similarities between Liquids and Fluidized Beds

The occurrence of fluidization phenomena analogous to solid-to-liquid melting and liquid-to-gas critical-point behavior was mentioned in the Introduction (pp 40-41). Between these two limits continuous expansion occurs in particulately fluidized beds as the superficial fluidizing velocity is increased. This may be likened to the thermal-expansion behavior of liquids; in which case the fluidized-bed variable equivalent to thermodynamic temperature should be some function of the fluidizing velocity.

Another characteristic of particulate fluidization is the relatively quiescent free upper surface of the bed. Very few particles attain sufficient energy to rise far above it; in this sense the bed resembles a liquid having low vapor pressure. In addition, the surface, when disturbed, will support wave propagation so that a finite surface tension may be associated with it.

The viscous behavior of the fluidized bed has been studied by a number of investigators (M2, D5, S7), as discussed in the Introduction. It was found that while uniform fluidization is maintained, the apparent viscosity of the beds decreases as the fluidizing velocity is increased. Thus, if the bed thermal energy is directly related to the fluid flow energy as indicated by the volumetric behavior, then the thermal behavior of the viscosity resembles that of liquids, rather than gases.

Phase separation and partial miscibility have also been observed in fluidized beds. Furukawa and Ohmae (F2) found that in some systems an increase in fluidizing velocity produced greater segregation, similar to solvation phenomena in liquids. In others segregation diminished as the fluidizing velocity was increased, much like polar-nonpolar behavior in liquids.

The above paragraphs have briefly stated those liquid-like characteristics of particulately fluidized beds which prompted this investigation. In the next section, the dynamics of liquid-molecule and fluidized-particle motion, which give rise to the observed phenomena, are compared.

B. Dynamics of Liquid-Molecule and Fluidized-Particle Motion

A reasonably complete discussion of the theory of nonpolar liquids was given in the Introduction (pp 1-38). The dynamics of each molecule's motion is determined by the conservative potential field formed by the other molecules, plus any imposed external field, e.g., a shearing stress. The mathematical difficulties involved in relating system properties to particle dynamics led in all cases to the consideration only of particle subgroups. In the basic cell model, the subgroup is the single molecule and its nearest neighbors. The molecular motion consists of vibrations within the cell with infrequent random diffusion between cells.

The fluidized particle's motion, on the other hand, is controlled by a different variety of forces. At steady state the downward force of gravity upon the particle is exactly matched by the upward drag force of the fluidizing flow. The force of gravity is here equivalent to a cohesive, or attractive, force between the particles, while the fluid drag is of expansive, or repulsive, character. Particle motion occurs because the local fluid-dynamic force fluctuates about its mean value and direction. This fluctuation is largely attributable to the presence of the surrounding particles, and will be assumed to have no preferred direction due to the flow distribution properties of those particles. The net force acting upon the particle is then effectively isotropic.

If the particles are smoothly fluidized, i.e., the flow of the fluidizing fluid is uniform spacially and timewise, the fluidized particles should behave in a manner similar to sedimenting particles, which retain their position relative to their neighbors. Thus, if attempts are made to establish relatively uniform flow of the fluidizing medium throughout the

bed the particles should tend to remain localized in their motion, i.e., oscillate about quasi-equilibrium positions. Particulate fluidization is of this character by definition.

Finally, since at steady state there is no translation of or rotation about the particle system's center of gravity, the net external forces and torques exerted upon that system must equal zero. Thus, it is meaningful to describe the fluidized system in terms of an apparent interaction potential of the particles themselves. The fluidizing fluid then acts as an "ether" which transmits the interparticle forces.

C. Scope of the Work

In the preceding two sections the phenomenological and particle-dynamic similarities between liquids and particulately fluidized beds have been considered. Both liquid molecules and fluidized particles were said to move, within the potential field established by their neighbors, in an isotropic mode about quasi-equilibrium sites, with random diffusion between sites. In both cases a large number of particles are present (of the order of 10^{23} in liquids and 10^{6} in our fluidized beds). To the extent then that particulately fluidized particles conform to our model, the statistical thermodynamic theories of liquids may be used to interpret fluidization phenomena.

Therefore, the objectives of this investigation were set as the establishment of a statistical-thermodynamic theory of fluidization on a self-consistent basis, and the experimental exploration of the meaningfullness of this representation. As a first step, experimental measurements of expansion, viscosity, miscibility, and surface-wave behavior were made on water-fluidized glass-sphere systems; the fluidization apparatus, experimental measurements, and their evaluation are discussed in the next chapter. Then an appropriate liquid model is chosen, the fluidization parameter equivalent to thermodynamic temperature is identified, and our experimental data, plus some from the literature, e.g., self-diffusion data, are interpreted using the statistical-thermodynamic relations.

III. EXPERIMENTAL STUDY

In this section the essential aspects of the fluidization system, i.e., the flow system, column, and packing, are described. Then the equipment employed, operational procedures, and measurement results are discussed for the four experimental phases of the investigation - expansion, viscosity, miscibility, and surface-tension measurements.

A. Fluidization Apparatus

1. Flow System

The general characteristics of the flow system are schematically illustrated by Figure III-1. The constant-head tank, located 25 feet above column inlet, served as the water source. Flow control to the column was maintained by three parallel Fisher-Porter rotameters, whose calibration curves are given as Figure A-1 in the Appendix. To improve the evenness of the water feed, the end of the 1/2-inch copper inlet tube was formed into a sparger by bending it into a 5-inch-square configuration, set horizontally, and drilled evenly at 1-1/8-inch intervals along its length by 3/64-inch holes pointing downward.

The flow then proceded through the six-inch distributor section filled with a homogeneous mixture of 0.375-inch ceramic spheres and 0.45-inch lead shot. (At a superficial velocity of 1.0 cm./sec. the pressure drop through the distributor section was 0.32 psf.) From there the water flowed through and fluidized the glass spheres in the visually monitored bed section, then out the overflow pipe and down the drain.

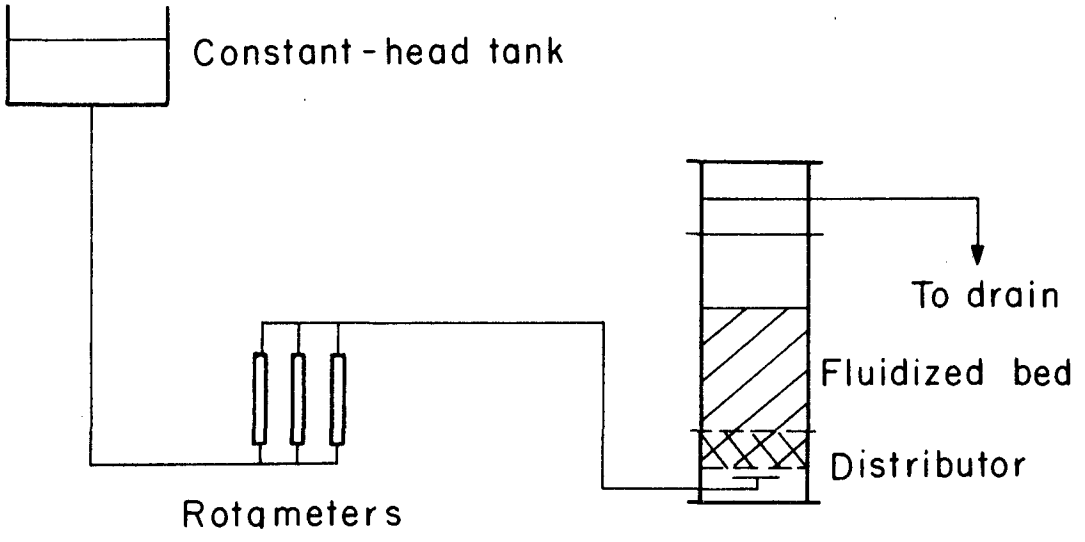

Fig. III-1. Flow system.

2. Column

The column and some of its accessory equipment are pictured in Figure III-2. As can be seen in this photograph, the column (having a nominal nine-inch inside diameter) was assembled from aluminum end-sections and a glass-pipe center-section. The glass section was mounted on an aluminum base plate through which a nine-inch hole had been drilled. The base plate was upheld by the double-unistrut support frame; and the bed-support screen and lower column section were attached to its underside.

The platform seen in the picture permitted easy access to the upper parts of the column, and a guard rail was placed at waist height above it. The jack mechanism shown beneath the column, bolted to the table which was on rollers, was used to support the 80-lb. bottom column section whenever that section was removed.

a. Bottom Column Section. The bottom section, detailed in Figure III-3, was 1-ft. long by 9-in. inside diameter. It was attached to the 3/4-in.-thick base plate by a ring of eight equally-spaced 7/16-in. by 1-1/2-in. bolts, which passed through identically-located 7/16-in. clear-drilled holes in the support-screen flange. The support-screen flange was further secured to the base plate by a hinge at the right side and a catch latch located diametrically opposite. With this arrangement, the bottom section could be removed while the 200-mesh stainless-steel support screen remained in place. To empty the bed material a large collecting vessel was placed beneath the screen, and the screen lowered.

The bottom section was divided into two parts by the distributor

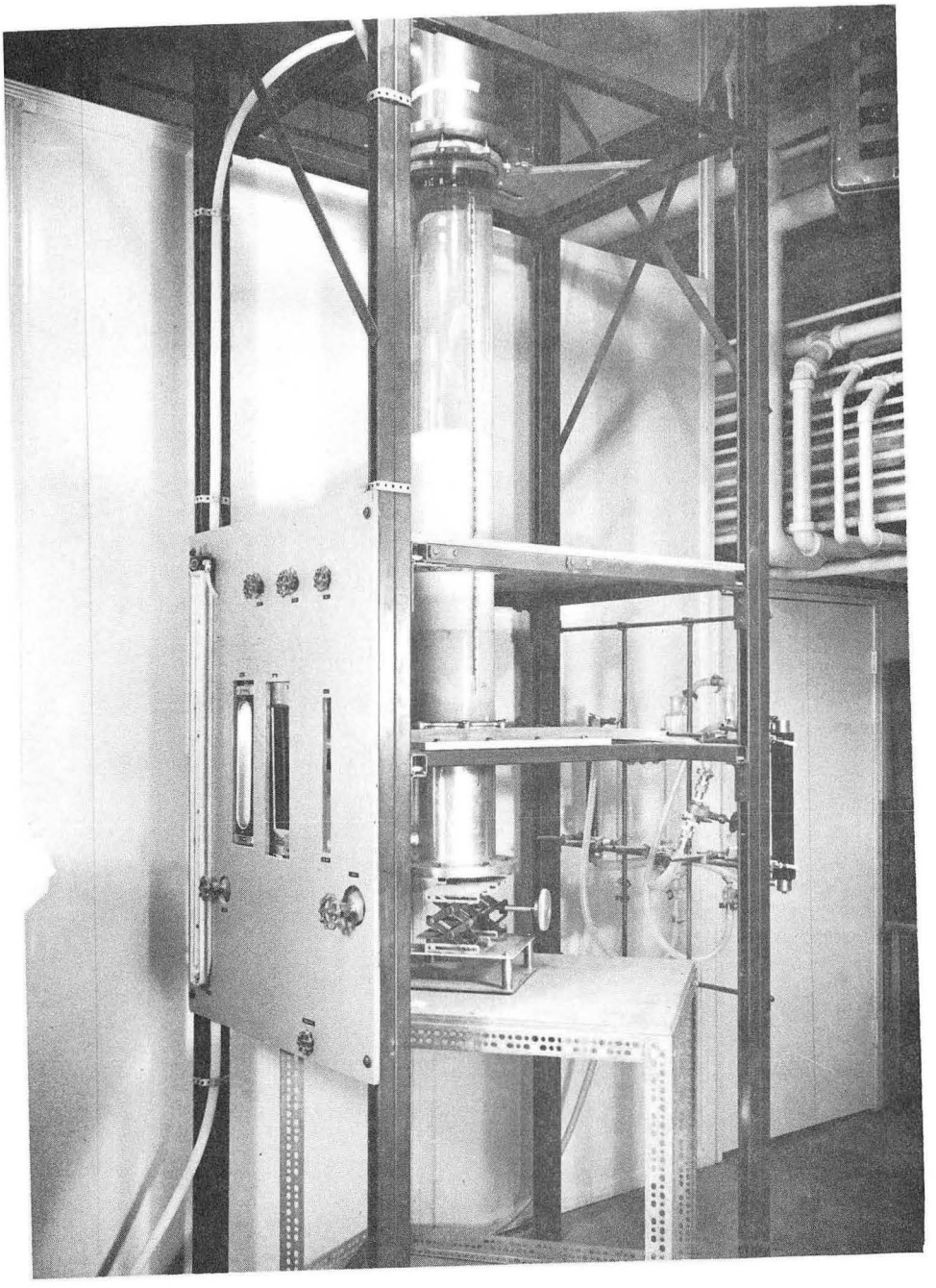

ZN-4079

Fig. III-2. Column assembly.

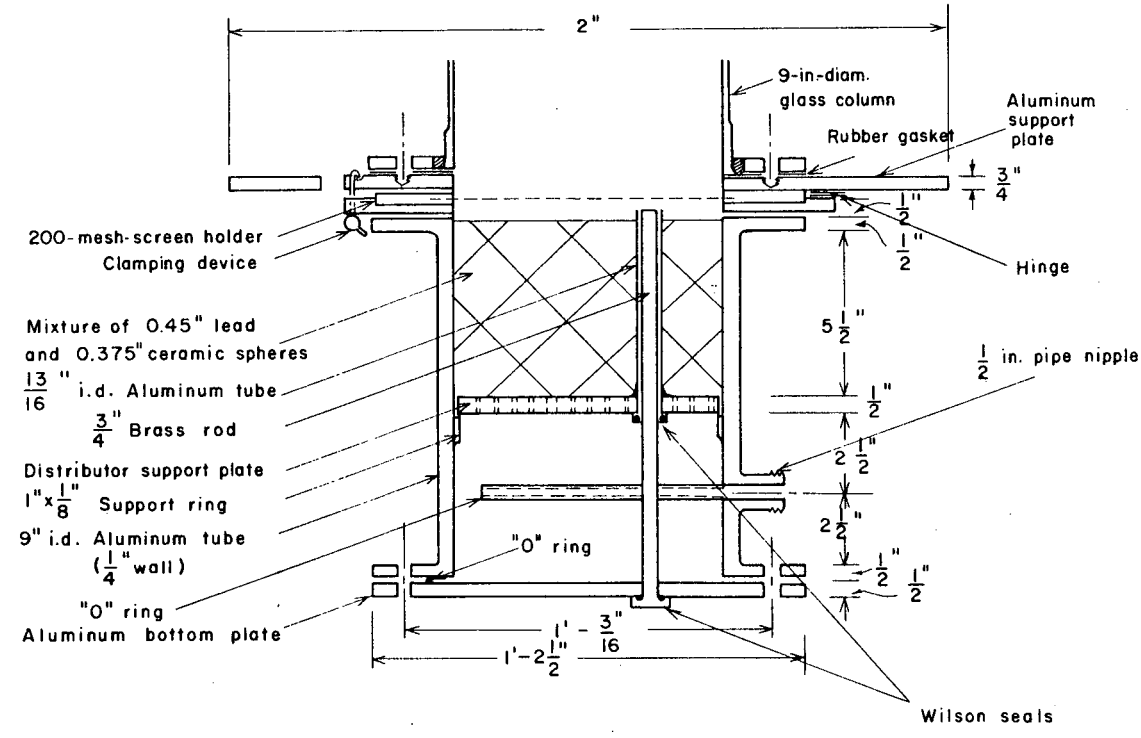

Fig. III-3. Fluidized-bed (bottom) distributor section.

support plate, a top view of which is given in Figure III-4. This 1/2-inch-thick aluminum plate had 13 concentric rings of 1/4-in. holes for fluid passage; a 1/16 by 1/16-in. triangular trough was machined between the holes in each ring to prevent the total blockage of a hole by one of the distributor particles.

The 13/16-in. aluminum tube, welded to the top of the distributor plate, formed a channel through the distributor material for the sampling tube used in the miscibility measurements. In all other experiments the solid brass rod was inserted to block the channel and prevent disruptively-high flow rates through that passage.

b. Glass Center-Section. The bed itself was contained by a section of industrial glass pipe 5 ft. long by 9 in. in nominal inside diameter, with a 3/8-in.-thick wall and flanged ends, manufactured by Q.V.F. Ltd. Examination of the pipe showed that along most of its length the inside diameter was constant at 8-17/32 inch; but the 4-3/8-inch-long flange sections attached at each end widened conically to the 9-inch value stated by the manufacturer. Cast-iron attachment collars around the flanged ends enabled the glass pipe to be mounted securely.

c. Calming Section. The top calming section, shown in Figure III-5, identically matched the bottom section in general detail, but did not have the flow-distribution devices of the latter. This section helped to eliminate end effects in the fluidized bed proper. It also served as a mounting platform for the two types of viscometers used. There were two pressure taps drilled through its lower flange, located diametrically opposite each other. (Similarly-located pressure taps were present in the column base plate.)

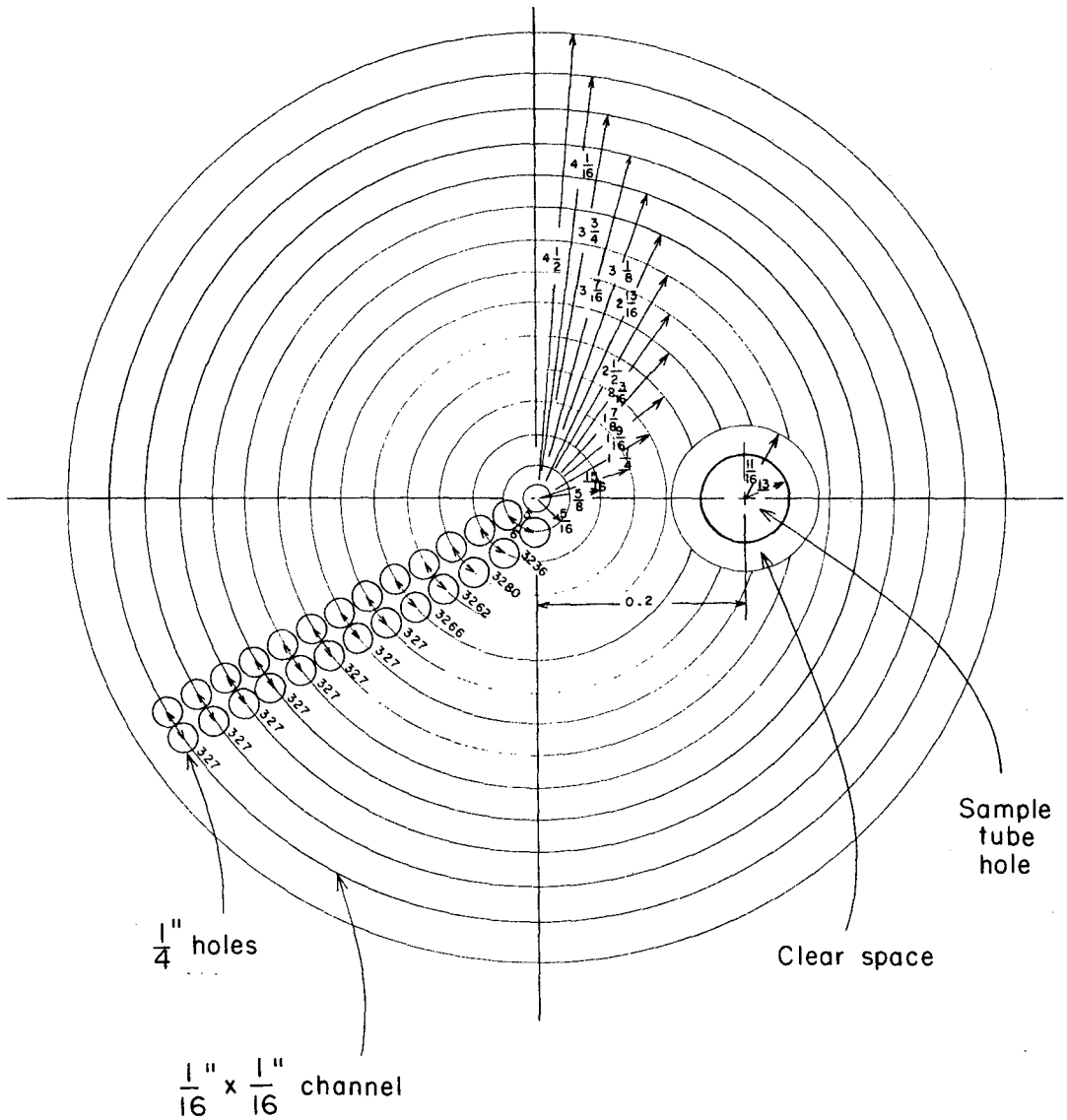

Fig. III-4. Distributor support plate.

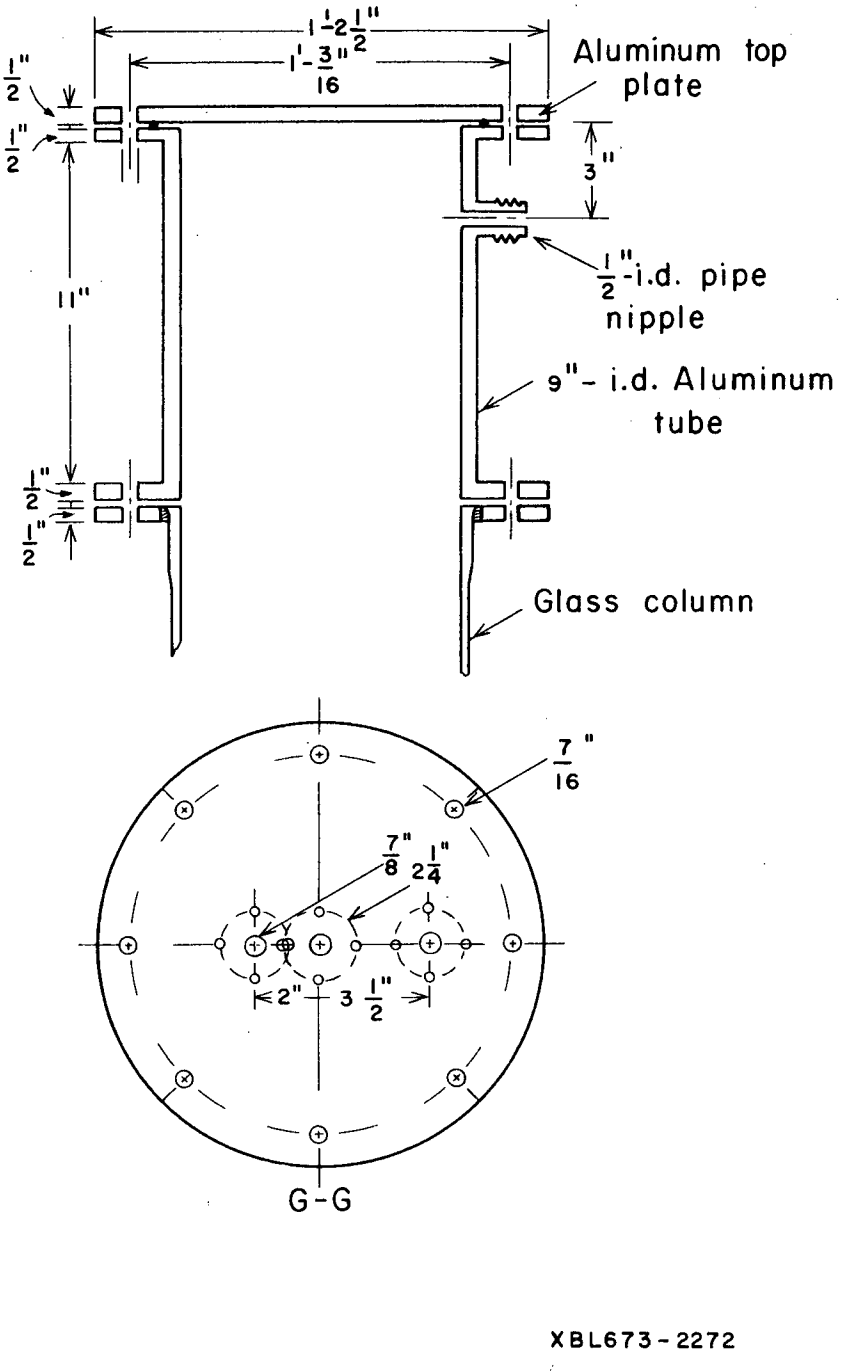

Fig. III-5. Top calming section.

3. Glass-Sphere Packing

The glass beads used were "Superbrite" brand obtained from the Minnesota Mining and Manufacturing Company. The beads were spherical in shape, as is illustrated by a 100:1 microphotograph of several 191-μ particles (Figure III-6), and had a particle density of 2.5 g./cc.

Particle-size distributions were ascertained from microphotographs; the distributions for several sizes are given as Figures A-2 - A-5 in the Appendix. The arithmetic-mean diameter was used to characterize the particles, and the related minimum-fluidization and terminal-settling velocities for the particles are given in Table III-1. Figure 7.7 of Zenz (Z1) was used to determine the minimum-fluidization velocity, and Figure 6.4 enabled the calculation of the terminal settling velocity. Our observed particle sizes matched closely those of Hoffman et al (H5) who appear to have employed particles from the same source.

Table III-1. Glass-sphere properties.

Manufacturer-Listed Diameter (Microns)	Measured Diameter (Microns)	Minimum Fluidization velocity (cm/sec)	Terminal Velocity (cm/sec)
470	455	2.63	10.5
290	270	1.09	3.73
200	191	0.629	2.64
150	142	0.285	1.40
100	95.5	0.196	0.747
60	52.2	0.005	0.294

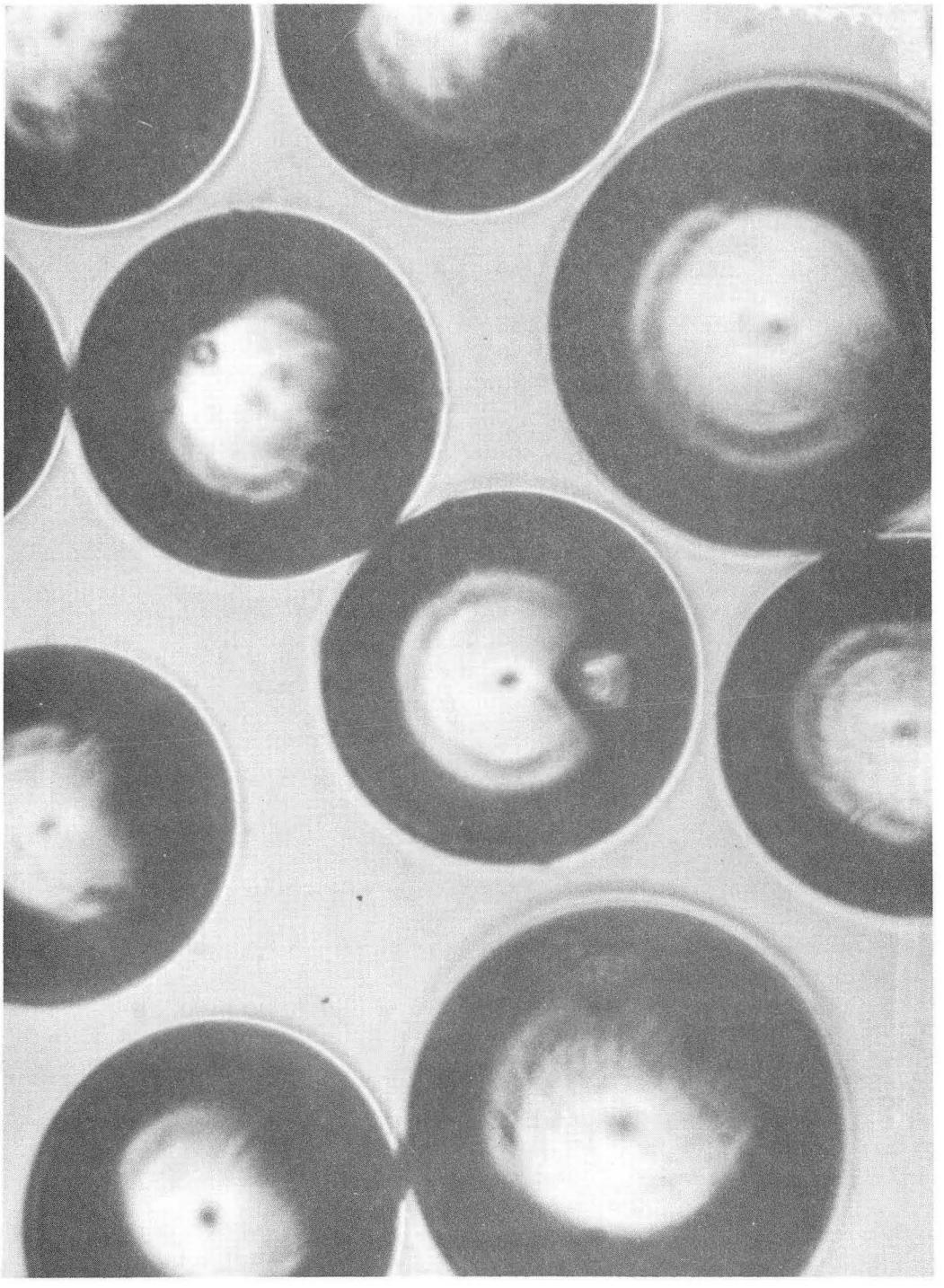

XBB675-2703

Fig. III-6. Photomicrograph of 191-micron glass spheres.

B. Volumetric Measurements

1. Equipment Description

The volumetric behavior of the system may be simply assessed by observing the height of the bed relative to its unfluidized height as a function of the fluidizing velocity. To do this an inch-scale was taped to the side of the glass column; this scale is clearly visible in Figure III-2.

2. Operational Procedure

It was found that the bed attained equilibrium more rapidly during contraction than during expansion. For this reason, the expansion measurements for the six particle sizes were made by over-expanding the bed and then measuring the expansion states for a sequence of decreasing fluidizing velocities. At least 3 to 5 minutes were allotted for the bed to reach equilibrium at each fluidizing velocity. In a number of instances, no observable volumetric change occurred when the fluidizing velocity was held constant over a period of several hours.

Water temperature was $20 \pm 2°C$ in all runs.

3. Experimental Results and Analysis

The expansion data, i.e., bed height h versus fluidizing velocity U, for the six particle sizes are tabulated in Table III-2. In order to determine the void-fractions ε (given in column 5) from the observed bed heights it was necessary to make a minor correction for the effect of the conical entrance section. As described on p. 77, the glass pipe contracted conically in 4-3/8-inches from a 9-inch initial flange diameter

Table III-2. Expansion data.

Particle Diameter (Microns)	Unfluidized Height (inches)	Fluidizing Velocity (cm/sec)	Fluidized Height (inches)	Void Fraction ϵ a
52.2	10	0.065	24.37	0.772
		0.054	22.37	0.752
		0.044	20.78	0.733
		0.033	19.0	0.708
		0.024	16.12	0.655
		0.0177	14.37	0.612
		0.0116	12.19	0.542
95.5	10.37	0.366	38.5	0.850
		0.296	30.75	0.815
		0.248	26.37	0.781
		0.204	22.31	0.745
		0.185	20.19	0.729
		0.165	20	0.712
		0.128	17.56	0.672
		0.096	15.12	0.625
142	10.78	0.517	32.41	0.806
		0.441	28.03	0.776
		0.369	24.41	0.744
		0.293	21.41	0.708
		0.215	18.34	0.659
		0.172	16.78	0.627
		0.130	15.28	0.590
		0.108	14.47	0.567
		0.087	13.66	0.542
		0.065	12.72	0.507

[a] $\epsilon_0 = 0.443$ in all cases.

Table III-2. (Continued)

Particle Diameter (Microns)	Unfluidized Height (inches)	Fluidizing Velocity (cm/sec)	Fluidized Height (inches)	Void Fraction ϵ^a
191	12.25	0.888	35.50	0.802
		0.739	30.12	0.768
		0.589	25.56	0.727
		0.441	21.62	0.679
		0.293	18.25	0.621
		0.218	16.50	0.582
		0.174	15.50	0.556
		0.131	14.25	0.518
270	12.22	1.038	27.03	0.748
		0.888	24.10	0.718
		0.739	21.66	0.636
		0.589	19.5	0.651
		0.441	17.34	0.608
		0.293	15.47	0.560
		0.218	14.22	0.521
		0.174	13.41	0.492
455	8.38	1.183	12.28	0.620
		1.038	11.59	0.598
		0.888	11.03	0.577
		0.739	10.47	0.554
		0.589	9.87	0.528
		0.441	9.28	0.497

[a] $\epsilon_0 = 0.443$ in all cases.

to a 8-17/32-inch tubing diameter. The greater volume per unit length in the conical section was taken into account by defining an equivalent length of 8-17/32 tubing, which in this case is 4-5/8-inches (0.25 inches longer than the actual length of the conical section.) From the continuity equation, for the same volumetric flow the mean superficial fluid velocity through the conical section is 0.945 times that through the straight tubing. Bena's (B3) relation, Eq. (I-80), predicts then that due to the lower flow rate the void-fraction in the conical section will be $(0.945)^{1/4.65}$, or 0.988, times that in the remainder of the bed. Assuming conservation of particles, the relationship between the void-fraction in the straight-tubing section ε and the measured bed height h is determined to be:

$$\varepsilon = \frac{(h+0.25)-(1-\varepsilon_o)(h_o+0.25)}{(h+0.25)-(1-0.988)4.625} \qquad (III-1)$$

Here h_o is the unfluidized-bed height, and ε_o is the minimum void-fraction which for our systems was found to be 0.443 (loosely-packed).

For comparison, sedimentation data were obtained for the 191μ system. The fluidizing flow to an expanded bed of void-fraction ε was cut off and the settling velocity of the upper bed surface measured. As shown in Table III-3, a close correspondence exists between the sedimentation velocity and the fluidizing velocity for that void-fraction.

Table III-3. 191 μ sedimentation data.

Unfluidized Height (cm)[a]	Fluidizing Velocity (cm/sec)	Fluidized Height (cm)	Fluidized Void Fraction ϵ	Sedimenting Velocity (cm/sec)
20.7	0.740	47.1	0.745	0.706
	0.589	41.1	0.707	0.559
	0.442	35.9	0.664	0.422
	0.369	33.4	0.639	0.358
	0.293	31.2	0.613	0.292
	0.218	28.8	0.580	0.231
	0.205	28.6	0.579	0.209
	0.174	27.3	0.557	0.176
	0.130	25.4	0.527	0.122
	0.109	22.9	0.508	0.109

[a] $\epsilon_0 = 0.443$

C. Viscosity Measurements

Two discrete methods were employed to measure viscous effects. The Brookfield viscometer measures the torque on a rotating bob as a function of rotational speed; and the moving-sphere determines the terminal velocity of a large sphere moving through the bed under a set weight difference.

1. Brookfield Viscometer

a. Equipment Description. A Brookfield Model LVT "Synchro-lectric" viscometer was employed for the more extensive set of fluidized-bed viscosity measurements. This instrument can produce eight rotational speeds - 60, 30, 12, 6, 3, 1.5, 0.6, and 0.3 rpm. - and has a spring constant of 6.737 ergs per degree of deflection.

The rotating spindle used with this viscometer was supplied by the manufacturer, on special order. Figure III-7 is a photograph of it. The central portion of the 3/4-in.-high by 3/4-in.-diameter cylinder was hollowed out to minimize its interference with the water flow. Its exterior surface was roughened with regularly-spaced 0.005-inch-deep vertical sawtooth cuts 0.0327-inch apart to promote more complete momentum transfer during particle impacts.

Since the bob geometry was designed so as to minimize the influence of the vertical flow of the fluidizing fluid, resistance to bob rotation should arise nearly entirely from particle impacts. This premise was confirmed by a series of measurements made in the absence of particles, which showed that the viscous effect of the flowing fluid alone was more than an order of magnitude less than the smallest values

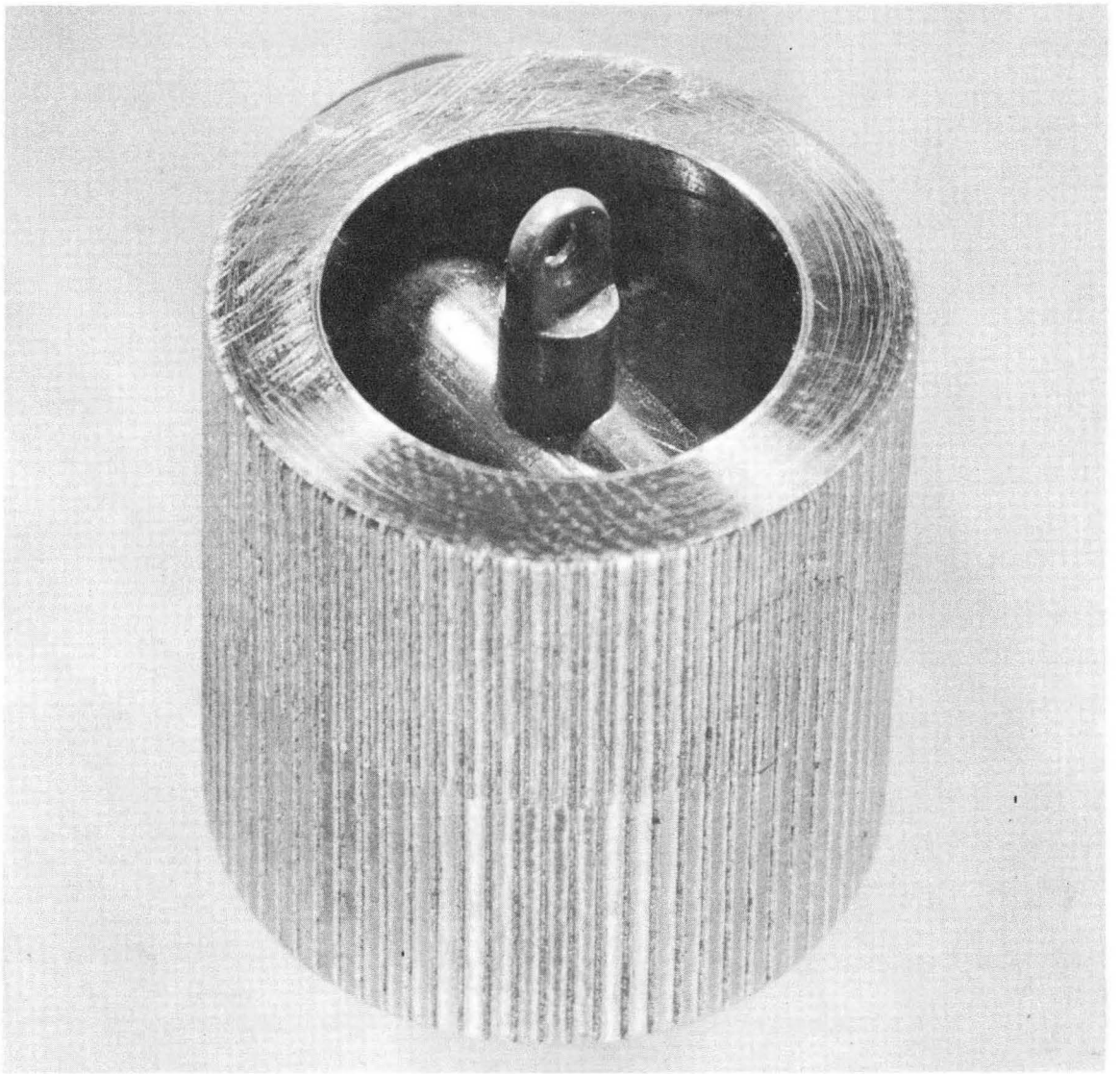

ZN-4080

Fig. III-7. Spindle for Brookfield viscometer.

observed in any of the fluidized beds.

The viscometer was mounted on the top plate of the column, and could be stationed at three radial locations - centered, or at either 2.0 or 3.5-inches off centerline; these are the locations of holes in the top plate as shown in Figure III-5. The spindle could be situated at various depths in the bed, ranging in 6-in. intervals from 3 to 33 inches of scale height, by employing a number of flexible extension wires.

b. Operational Procedure. As the first step in the Brookfield measurements for each bed, the viscometer spindle was lowered into the column by a number of 1-foot extension wires, hooked end to end. A 3-inch and a 6-inch segment were also available, permitting greater latitude in setting the spindle height above the support screen. In our measurements, heights of 9, 15, and 18 inches were used, as these placed the spindle at the approximate midpoint of the expanded beds. The height was maintained constant for each set of measurements.

The uppermost extension wire was passed through the hole in the top plate of the calming section, and hooked to the lower shaft of the viscometer. The viscometer was then mounted on the cover plate by its two screws, and leveled using the bubble level on its casing.

To make a set of measurements, the bed was expanded to the desired level, the spindle rotation rate ω varied over the available range, and the resulting viscometer-pointer angular deflection θ recorded. At least 15 minutes were allotted to insure expansion equilibrium prior to starting the viscosity measurements. The physical properties of our system were such that only the three higher rotation rates, i.e., 60, 30, and 12 rpm, yielded meaningful values for θ. These rotation rates were traversed twice, in descending and ascending order. Three minutes were needed to come to equilibrium at each rotation-rate setting, and the readings were checked at least three times.

c. Measurement Results and Analysis. Brookfield measurements were made for 52.2, 95.5, 142, 191, and 270μ particle-diameter beds, and the results are tabulated in Table III-9. Fluctuating particle-convection currents present in the 455μ bed, however, precluded viscosity measurements for that system, i.e., it was not possible to obtain steady-state values for the local shearing stresses.

As may be seen in the table, the magnitude of the viscometer-needle angular deflection θ was 10 or less in most instances, even for the higher rotation rates. This was due to the relatively small (3/4-in.×3/4-in.) viscometer bob, which had been designed to yield point-viscosity values and to minimize flow-field interference. The two-orders-of-magnitude fall-off in water-fluidized-bed viscosities relative to the comparable gas-fluidized-bed values (S7) had not been anticipated. Unfortunately, the resulting low angular deflections for bob-rotation rates of less than 12 rpm could not be accurately measured. This problem was accentuated by an insensitivity of the Brookfield viscometer at its lower range of operation. Angular deflections of 2° or more were found to be reproducible and self-consistent, but values of less than 2° were not. As a result, only those data corresponding to $\theta \geq 2°$ are treated as meaningful in the following discussion.

The angular deflections θ are plotted as a function of spindle-rotation rate in Figures III-8 - III-12. The form of the shear curves is seen to be quite similar for the four larger particle sizes. The curves are clearly nonlinear, and an inflection point may be present at the higher void-fraction; the existence of such an inflection point in the 52.2μ curves seems apparent. The limited number of data points (2 or 3)

Table III-4. Brookfield viscosity data.

Spindle height and location (inches)	Particle diameter (microns)	Fluidizing velocity (cm/sec)	Void Fraction ϵ	$\theta(60)$ (deg)	$\theta(30)$ (deg)	$\theta(12)$ (deg)	Viscosity based on initial slope (centipoise)
9(cl.)	95.5	0.442	0.892	4.0	2.4	1.1	9.7
		0.369	0.850	4.05	2.2	1.1	9.8
		0.293	0.812	4.4	2.3	1.1	10.6
		0.248	0.781	4.6	2.4	1.1	11.1
		0.204	0.745	4.9	2.6	1.4	11.9
		0.187	0.713	4.9	2.6	1.4	11.9
		0.165	0.711	5.3	2.6	1.4	12.8
		0.131	0.671	5.5	2.9	1.4	13.3
		0.096	0.618	5.9	2.9	1.5	14.3
		0.065	0.542	7.0	3.6	1.6	16.9
		0.052	0.498	8.0	5.4	2.4	30.2
9(cl.-3.5)	95.5	0.366	0.852	4.1	2.1	1.1	9.9
		0.296	0.815	4.1	2.1	1.2	9.9
		0.248	0.781	4.5	2.3	1.2	10.9
		0.204	0.746	4.6	2.3	1.1	11.1
		0.185	0.730	4.6	2.4	1.2	11.1
		0.165	0.711	4.8	2.5	1.3	11.6
		0.128	0.672	5.0	2.6	1.4	12.1
		0.096	0.625	5.9	2.9	1.6	14.3
		0.065	0.576	7.1	3.0	1.8	17.2
		0.045	0.538	8.1	4.1	2.0	19.4
9(cl.)	191	0.888	0.802	7.5	4.2	2.2	28.2
		0.739	0.768	7.6	4.3	2.2	28.6
		0.589	0.727	7.7	4.4	2.2	29.0
		0.441	0.679	8.5	4.8	2.3	32.0
		0.293	0.621	9.5	5.5	2.7	36.7
		0.218	0.582	10.5	6.3	3.0	40.3

Table III-4. (Continued)

Spindle height and location (inches)	Particle diameter (microns)	Fluidizing velocity (cm/sec)	Void fraction ϵ	$\theta(60)$ (deg)	$\theta(30)$ (deg)	$\theta(12)$ (deg)	Viscosity based on initial slope (centipoise)
		0.174	0.556	12.0	7.0	3.4	45.1
		0.131	0.518	18.9	10.9	5.0	62.9
		0.087	0.458	79.0	53.0	31.4	29.7
9(cl.)	270	1.038	0.748	7.4	4.0	1.8	20.3
		0.888	0.718	8.3	4.2	1.9	22.8
		0.739	0.686	9.0	4.7	2.1	24.7
		0.589	0.651	9.4	5.1	2.1	25.8
		0.441	0.608	10.3	5.9	2.6	31.9
		0.293	0.560	13.4	7.9	3.6	45.9
		0.218	0.521	19.1	11.4	4.6	65.4
		0.174	0.492	35.0	23.4	13.2	120.0
18(cl.)	52.2	0.065	0.772	3.5	1.8	1.1	-
		0.054	0.752	3.9	1.8	1.3	-
		0.044	0.733	4.7	2.2	1.5	-
		0.033	0.705	5.1	2.3	1.5	-
		0.024	0.655	6.1	2.5	1.9	-
		0.018	0.612	8.1	3.1	2.0	-
18(cl.)	270	1.038	0.748	8.4	4.2	2.5	20.3
		0.888	0.718	8.7	4.6	2.4	28.3
		0.739	0.686	10.4	5.5	2.1	33.8
		0.589	0.651	10.6	6.0	2.6	34.5
		0.441	0.608	11.9	7.0	3.0	38.7
		0.293	0.560	15.0	7.6	3.0	51.4
15(cl.)	142	0.517	0.806	4.6	2.9	1.5	11.1
		0.441	0.776	4.6	2.9	1.7	11.1
		0.369	0.744	4.9	2.5	1.9	11.8
		0.293	0.708	5.3	3.2	2.0	12.8
		0.215	0.659	6.1	2.9	1.9	14.7

Table III-4. (Continued)

Spindle height and location (inches)	Particle diameter (microns)	Fluidizing velocity (cm/sec)	Void fraction ϵ	$\theta(60)$ (deg)	$\theta(30)$ (deg)	$\theta(12)$ (deg)	Viscosity based on initial slope (centipoise)
9(cl.)		0.172	0.627	9.0	4.2	3.1	21.8
		0.130	0.590	10.1	5.0	3.0	24.4
		0.108	0.567	10.8	6.1	3.1	43.5
		0.087	0.542	11.8	6.9	3.7	48.3
		0.065	0.507	14.1	8.8	4.5	58.0
		0.052		25.3	13.9	7.3	104.0

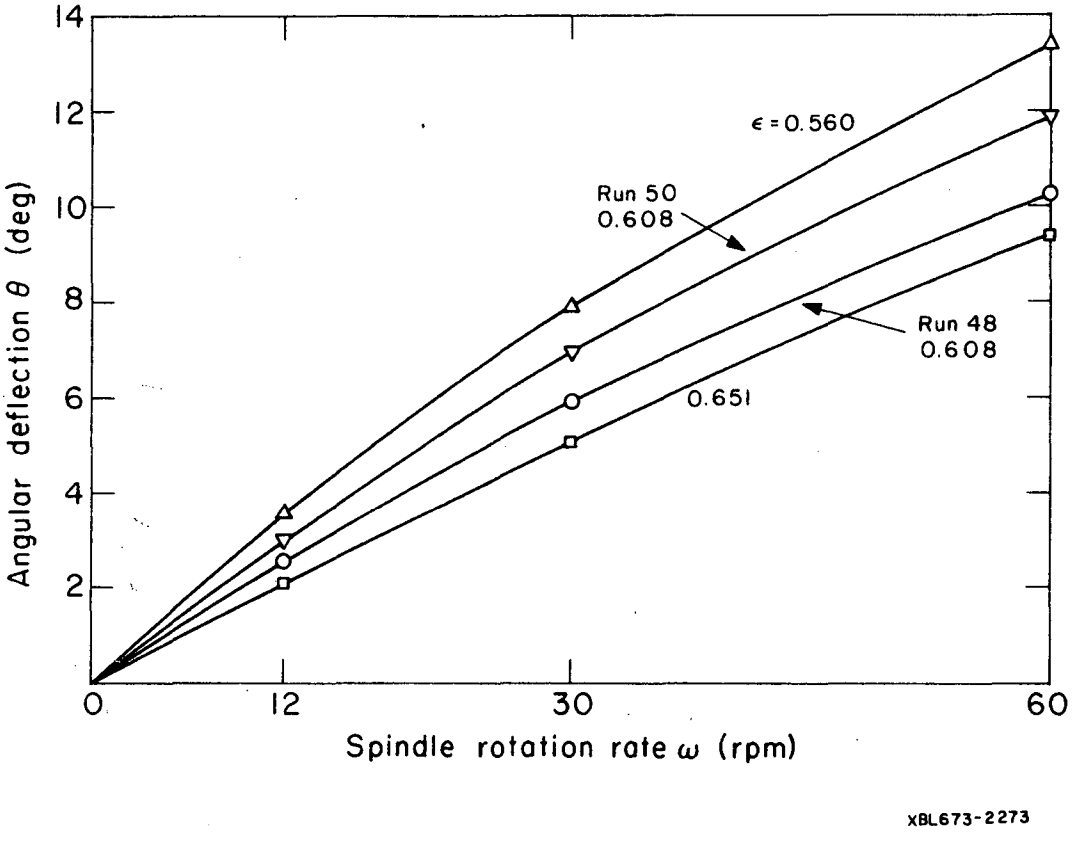

Fig. III-8. Brookfield shear curves for 270μ particles.

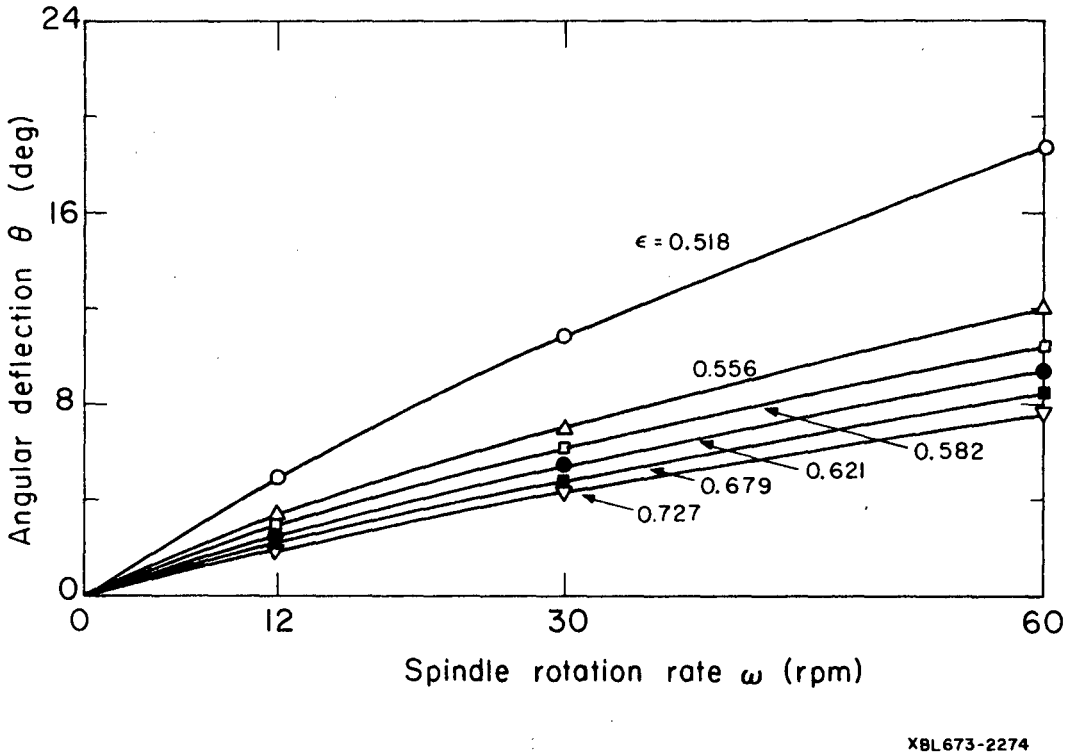

Fig. III-9. Brookfield shear curves for 191μ particles.

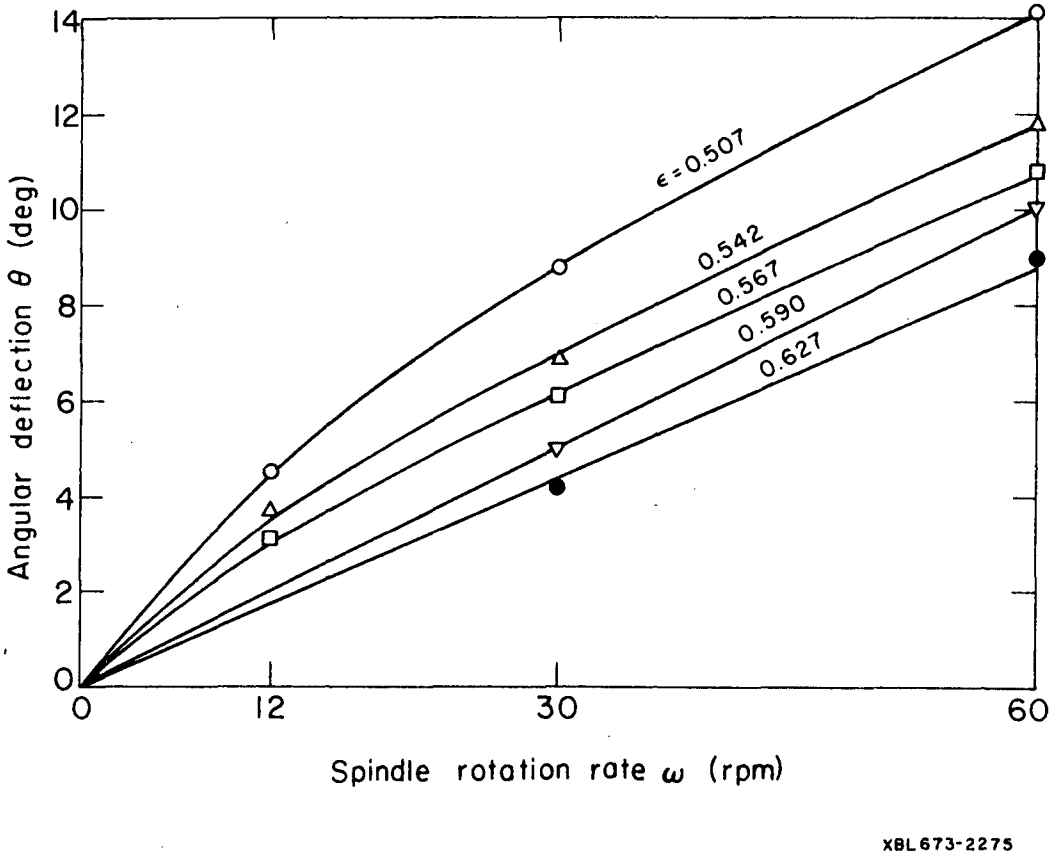

Fig. III-10. Brookfield shear curves for 142μ particles.

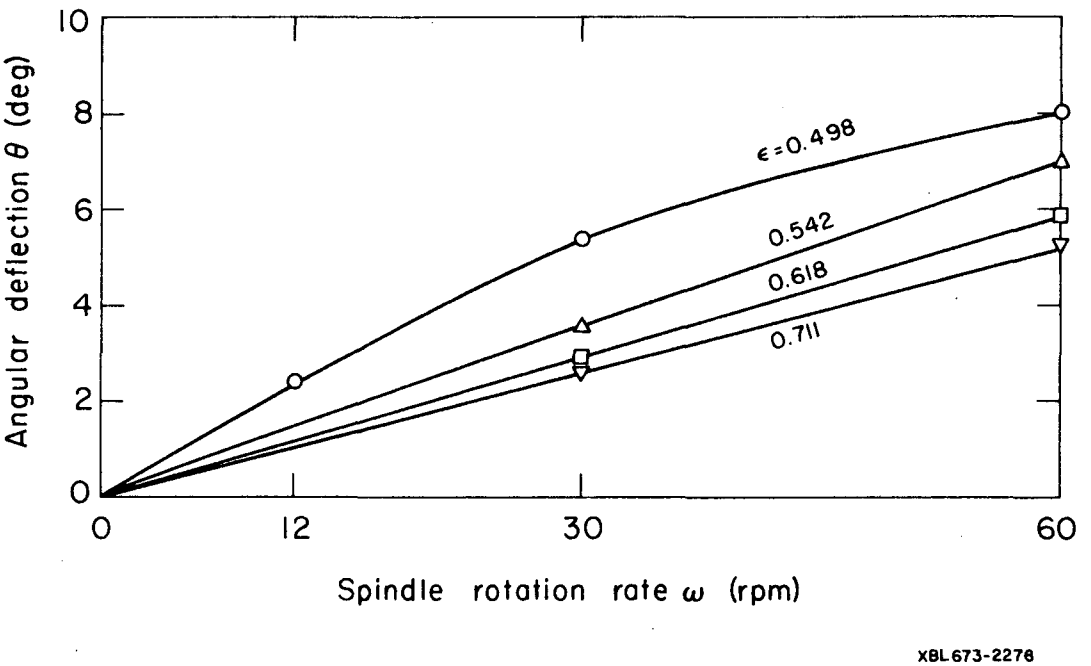

Fig. III-11. Brookfield shear curves for 95.5μ particles.

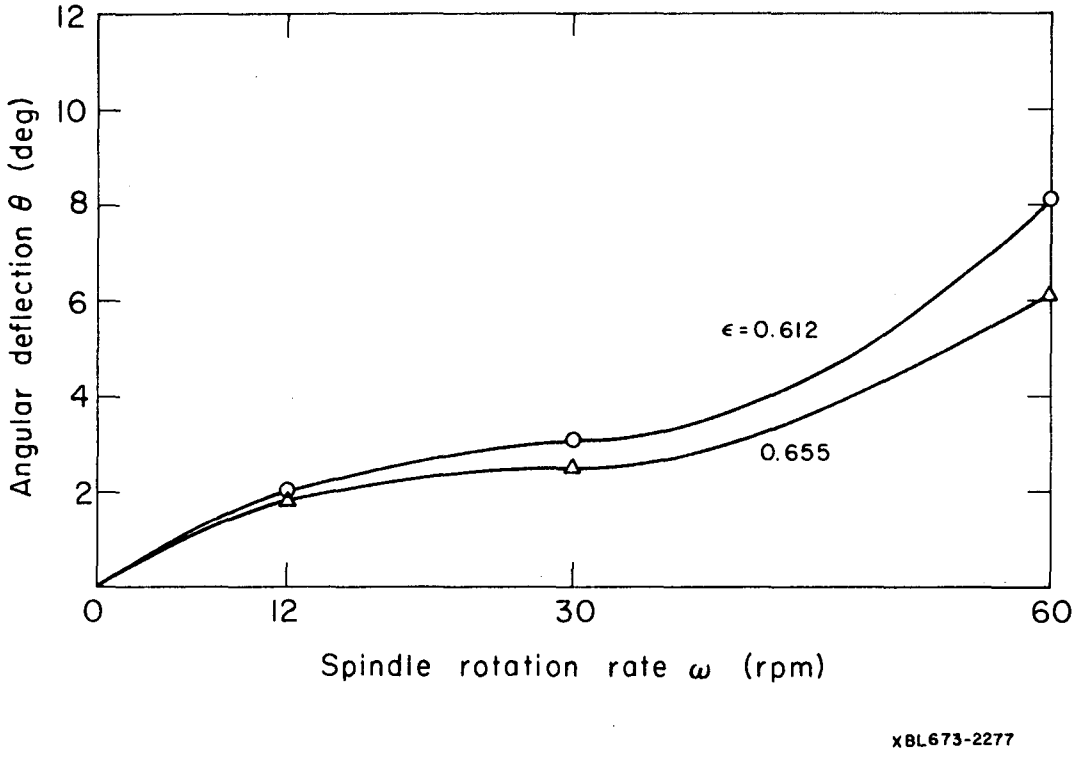

Fig. III-12. Brookfield shear curves for 52.2μ particles.

for each curve prevents complete definition of the shear curves, and prohibits a comprehensive discussion of bed viscous effects. Fortunately, for our statistical-thermodynamic model we are primarily interested in the initial curve slopes, which may be determined with a reasonable degree of accuracy.

The bed viscosities may be determined from the stress curves by consideration of the equation of motion. The θ component of the equation of motion, written in cylindrical coordinates, is:

$$\frac{1}{r^2}\frac{\partial}{\partial r}(r^2\tau) = 0 \qquad (\text{III-2})$$

which integrates to:

$$r^2\tau = K_1 \qquad (\text{III-3})$$

where τ is the tangential shear on the fluid element and K_1 is an integration constant. The velocity gradient in cylindrical coordinates is defined by:

$$D(\tau) = -r\frac{\partial}{\partial r}\left(\frac{V_\theta}{r}\right) = -r\frac{\partial \omega}{\partial r} \qquad (\text{III-4})$$

Here v_θ is the angular velocity and ω is the angular rotation rate, v/r. The integral of Eq. (III-4) for a spindle rotating in an infinite medium is

$$\omega = -\int_0^r D(\tau)\frac{dr}{r} \qquad (\text{III-5})$$

which with the help of the differential form of Eq. (III-3):

$$\frac{dr}{r} = -\frac{d\tau}{2\tau} \qquad (III-6)$$

becomes:

$$\omega = \frac{1}{2}\int_0^{\tau} \frac{D(\tau)}{\tau}\, d\tau \qquad (III-7)$$

Differentiating Eq. (III-7) with respect to τ leads to:

$$\frac{D(\tau)}{2\tau} = \frac{d\omega}{d\tau} \qquad (III-8)$$

By definition the apparent Newtonian viscosity is:

$$\eta = \frac{\tau}{D(\tau)} \qquad (III-9)$$

which by Eq. (III-8) is, therefore:

$$\eta = \frac{1}{2}\frac{d\tau}{d\omega} \qquad (III-10)$$

To employ Eq. (III-10) to interpret the shear curves, the shear stress τ must be related to the measured viscometer-needle angular deflections θ. The viscometer itself had been fully calibrated by the manufacturer, i.e., the spring constant had been carefully established. It was necessary, however, to empirically calibrate the viscometer-bob system since this bob differs from those conventionally employed. This

was done using Newtonian fluids of known viscosities. The measurement results are listed in Table III-5, and the calibration curves are plotted in Figure III-13. From these curves the relationship equivalent to Eq. (III-6) between viscosity and the observed angular deflection as a function of rotational bob velocity was found to be:

$$\eta = 145 \; d\theta/d\omega \quad [=] \text{ centipoise} \qquad \text{(III-11)}$$

where θ is the angular deflection in degrees, and ω is the rotational bob velocity in min.^{-1}.

By Eq. (III-11) an apparent Newtonian viscosity based on the local curve slope may be determined for each point on the shear curves. As indicated on p. 101 we are primarily interested in the initial curve slope, which we assume represents a Newtonian limit. This assumption seems justified based on a comparison with the results of Schügerl et al (S7) for gas-fluidized beds of glass spheres and quartz sand, discussed on pp. 58, 62-63 of the Introduction. As illustrated by Figure I-4, the form of their shear curves is identical to ours for the same spindle-rotation velocity range. Since they obtained data over a larger rotational velocity range, however, they were able to more completely define the shear curves, as shown in Figure I-5. They determined their bed viscosities in the manner present above, except that for a concentric-cylinder viscometer with the inner cylinder moving and the outer cylinder held fixed, Eq. (III-7) becomes

$$\omega = \frac{1}{2} \int_{(r_i/r_o)^2 \tau}^{\tau} \frac{D(\tau)}{\tau} \, d\tau \qquad \text{(III-12)}$$

Table III-5. Brookfield-viscometer calibration data.

Material	Temperature (deg cm)	Reference Viscosity (centipoise)[a]	Spindle Rotation Rate ω(RPM)	Angular Deflection (deg)
Castor oil	25	490	12	44.4
			6	23.5
			3	12.5
	22.5	670	12	56.6
			6	28.6
			3	15.4
Ethylene	21.9	19.2	60	8.9
Glycol			30	4.0
			12	2.0
Cyclo-	36.0	29.1	60	12.0
hexanol			30	5.7
			12	2.9
Glycerine	41.0		60	34.5
(93%)			30	17.0
			12	7.2
			6	3.6
	25.8	285	60	86.1
			30	42.1
			12	17.1
			6	9.0
			3	5.3
			1.5	3.1

[a]Handbook of Chemistry, N. A. Lange, Ed. (Handbook Publ., Sandusky, Ohio).

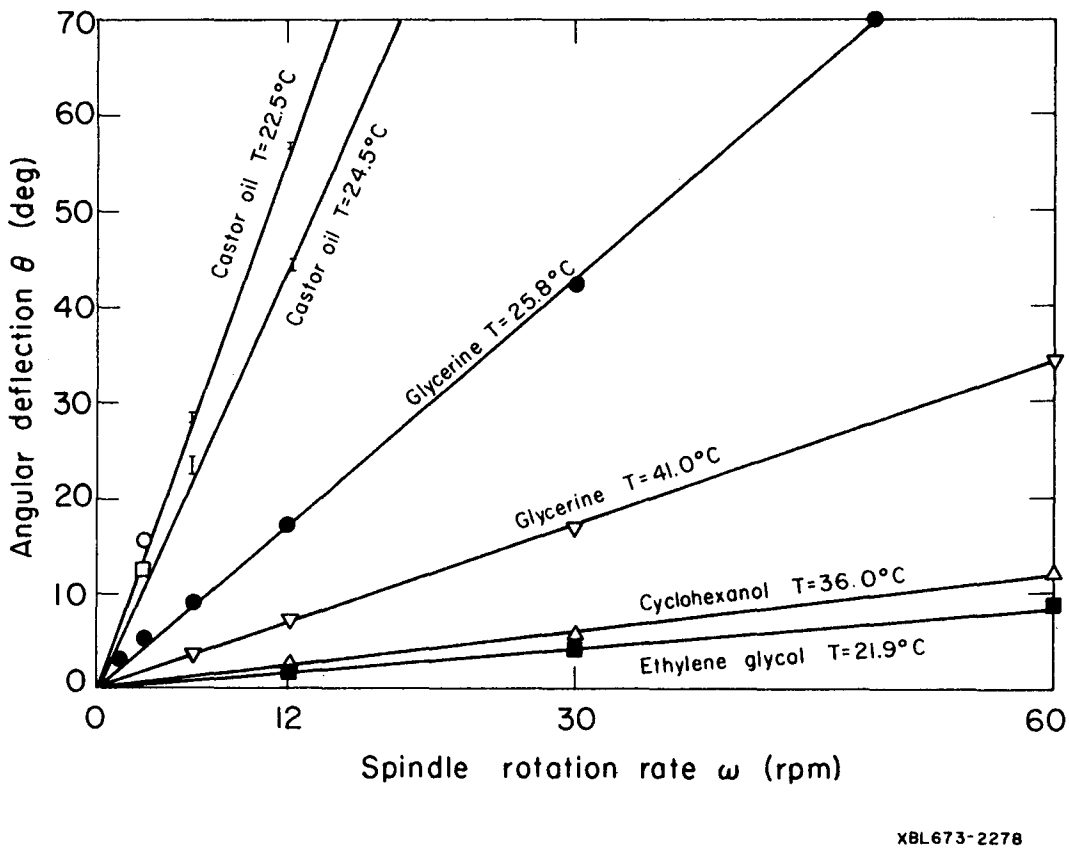

Fig. III-13. Brookfield viscometer calibration data.

where r_i and r_o are the inner and outer cylinder radii. The resulting expression for the shear rate is

$$D(\tau) = D\left[(r_i/r_o)^2\tau\right] + 2\tau\,\omega'(\tau) \qquad (\text{III-13})$$

which Pawlowski (P9) pointed out is equivalent to

$$D(\tau) = 2\tau\sum_{k=0}^{\infty}(r_i/r_o)^{2k}\,\omega'\left[(r_i/r_o)^{2k}\tau\right] \qquad (\text{III-14})$$

where ω' denotes $d\omega/d\tau$. Schügerl et al. graphically determined that their data when substituted in Eq. (III-14) could be correlated by:

$$D(\tau) = A_1 \sinh(B_1\tau) \qquad (\text{I-96})$$

where A_1 and B_1, defined by Eqs. (I-97) and (I-98), are functions of the particle properties and flow velocity v. Since the form of Eq. (I-96) is identical to that of Eyring's (E5) rate-theory expression, Eq. (I-100), Schügerl et al. interpreted their results on that basis (as discussed on p. 63). One facet of the Eyring expression for viscosity is that it approaches a Newtonian limit as the shear rate goes to zero. Thus, Schügerl et al.'s viscosities, and our own by similarity, approach a Newtonian limit η_o as $\omega \to 0$.

The Newtonian viscosities η_o are tabulated in column 8 of Table III-1 and plotted as a function of fluidizing velocity in Figure III-14. Since the fluidizing velocity U is directly related to bed "temperature" (as shown in Chapter IV), the temperature dependence of the viscosity is seen to be

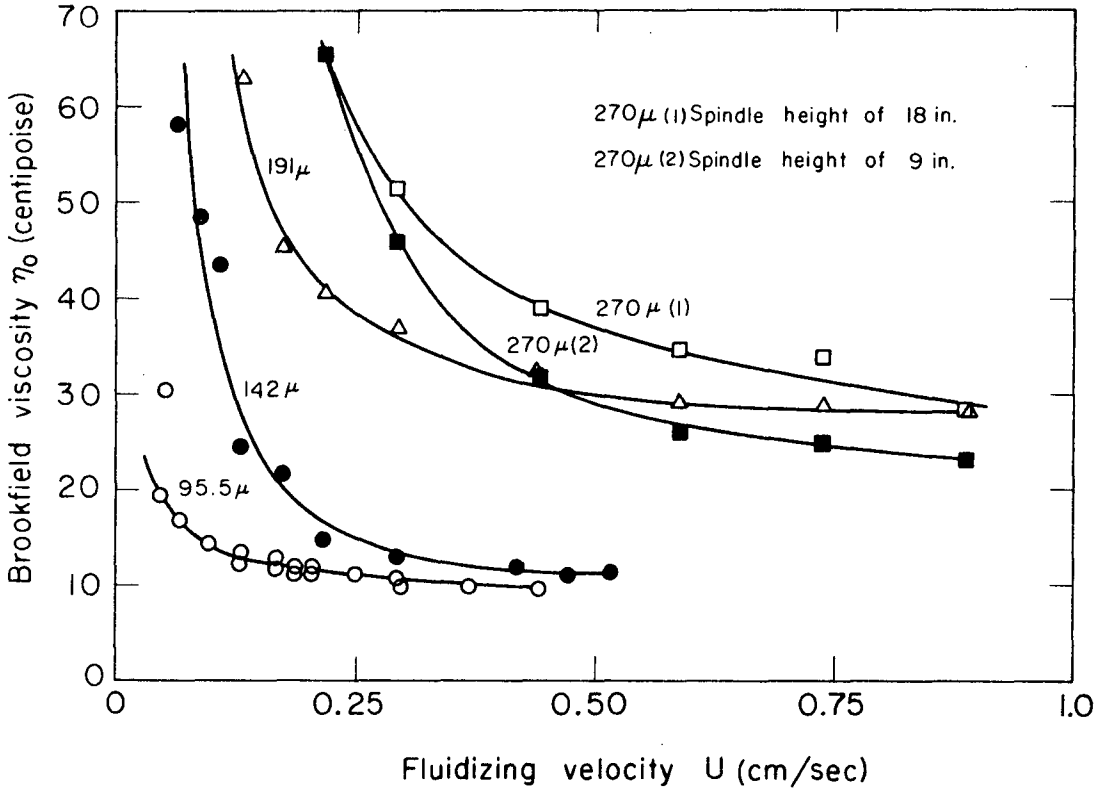

Fig. III-14. Brookfield viscosity data plotted as a function of fluidizing velocity U.
270(1) spindle height of 18-inches
270(2) spindle height of 9-inches

liquid-like, i.e., the viscosity decreases with increasing temperature, rather than gas-like, i.e., increasing viscosity with increasing temperature. In addition, the 20-80 centipoise magnitude of the viscosities is roughly two orders of magnitude less than the values reported by Schügerl et al. for the corresponding gas-fluidized beds. The viscosity data are correlated by our (liquid-like) statistical-thermodynamic model in Chapter IV, and the relationship between water-fluidized-bed and gas-fluidized-bed viscosities is discussed at that time.

The two sets of measurements in the 95.5μ system represent, as indicated, two radial locations of the viscometer spindle - on the centerline and 3.5-inches off the centerline (within 3/4-inch of the column wall). The results lie within 10% of each other for all but the lowest void-fraction, and no consistent trend is discernible. Likewise, the axial variation of viscosity may be ascertained from the two sets of data for the 270μ system, in which the spindle height was set at 9 inches for one set and at 18 inches for the other. Here the agreement is to within 30%, with lower viscosity values measured in the lower section of the bed. Thus, relatively uniform particle dispersion and motions are indicated throughout the bed, with slightly greater particle velocities indicated in the upper bed section.

2. Moving-Sphere Viscometer

a. Equipment Description. A schematic diagram of the moving-sphere viscometer apparatus is given in Figure III-5. It consisted of the moving sphere, two pulleys, a weight-pan and weights, and a length of 10μ line.

Two types of moving spheres were employed. A 1/2-inch-diameter aluminum sphere was used for the initial set of measurements. This sphere was then coated with a layer of 191μ glass spheres, sealed on by epoxy cement; and a number of "rough" sphere measurements made. Some additional "smooth" sphere data were later gathered using a second (uncoated) 1/2-inch aluminum sphere. The characteristics of these moving spheres are summarized in Table III-6.

The two pulleys were Lucite discs of 1-inch diameter and 3/32-inch thickness, mounted on 1/4-inch bearings. One pulley was so located on the top plate that the moving sphere traveled along the centerline of the column, and the other overhung the edge of the top plate so that the motion of the external-weight system was not impeded by the column flanges. Care was taken to minimize pulley friction; by a series of measurements in air and in quiescent water, the pulley friction coefficients were determined to be:

$$\mu_p = \mathcal{F}/N = 0.0090 \qquad (III-5)$$

where $\mathcal{F}$ is the pulley friction and N is the net downward weight upon the pulley.

Ten-micron nylon line, weighing $2.2 \cdot 10^{-4}$ g/cm., was used to link the moving sphere to the external weight system. At one end it was tied

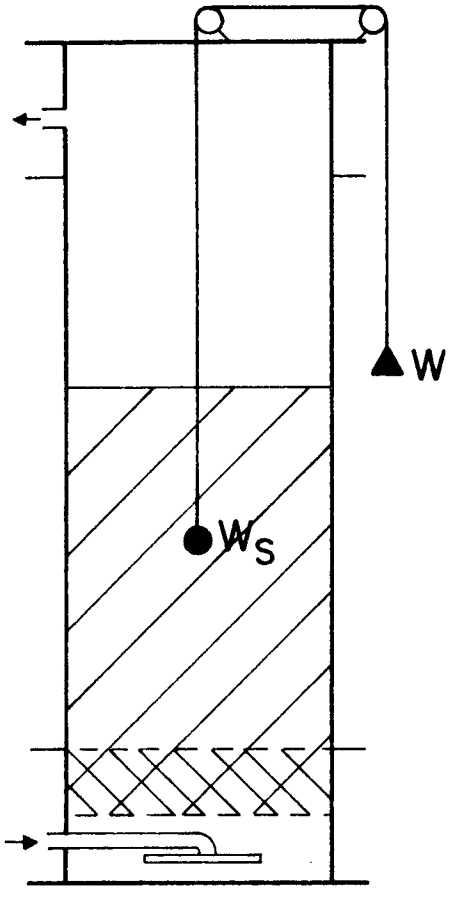

XBL673-2279

Fig. III-15. Moving-sphere viscometer.

Table III-6. Physical properties of the moving spheres.

Run Nos.	Moving-sphere diameter d_s (cm)	Moving-sphere weight w_s (g)
27, 29, 33	1.27[a]	2.9763
44	1.308[b]	3.1778
45	1.27[c]	2.9694

[a] Sphere No. 1

[b] Sphere No. 1 modified by a coating of 191μ glass spheres

[c] Sphere No. 2

to a short piece of six-micron nylon line sealed with epoxy into a small hole in the top of the sphere; at the other it was connected to the support strings of the weight pan.

b. Operational Procedure. The direction of passage of the moving sphere through the fluidized bed was controlled by choice of the external weight w. An excess, or deficit, in w relative to the buoyed sphere weight caused the sphere to rise, or fall, through the bed. In general a sequence of weights was used which straddled the sphere weight, so that both rising and falling sphere data were obtained for each bed state.

The value of the sphere's terminal velocity was measured by clocking the visually observed motion of the external weight between two reference heights by means of a hand-held stopwatch. Two passage lengths were clocked in each case to insure that a true terminal velocity had been achieved.

c. Measurement Results and Analysis. The moving-sphere measurement results are presented in Table III-7. The deduced viscosities are also included in the table, and some discussion of their derivation is worthwhile.

Although the flow field in the vicinity of the moving sphere cannot be described analytically, an apparent viscosity can be determined in the following manner by use of the standard drag correlation for spheres. Assuming that the drag effects on the moving sphere of the fluidized particles and the fluidizing flow are additive, the drag force attributable to the particles F_s when the moving sphere is at its terminal velocity is:

$$F_s = \left| W - W_s \frac{\Delta\rho}{\rho_{ms}} \right| - F_f - \mathcal{F} - \Delta l_w \qquad \text{(III-16)}$$

Here w denotes the external weight, w_s is the sphere weight, ρ_{ms} is the moving-sphere density, and $\Delta\rho$ is the difference between the moving-sphere and mean-bed densities, i.e., $\varepsilon(\rho_{ms}-\rho)$. The friction force $\mathcal{F}$ is given by Eq. (III-15), and the buoyed-line-weight difference Δl_w is based on the mean location of the sphere during the run. The fluid drag force F_f to be used in Eq. (III-16) is calculated by:

$$F_f = C_D(Re_f) \frac{\rho U_{rel}^2}{2} \frac{\pi d_s^2}{4} \qquad \text{(III-17)}$$

where the fluid Reynolds number Re_f is defined as $\rho U_{rel} d_s/\mu$ with d_s being the moving-sphere diameter. The relative velocity between the sphere and fluid U_{rel} is defined as the sphere velocity v_s plus or minus the

Table III-7. Moving-sphere measurements.

Bed-particle diameter (micron)	Moving-sphere diameter (cm)	Fluidizing velocity (cm/sec)	Void fraction ϵ	External weight (dyne)	Moving-sphere velocity (cm/sec)	Viscosity [Based on ϵ] (cp)	Revised void fraction ϵ_ℓ	Revised viscosity (cp)	Mean viscosity (cp)
95.5	1.27 (smooth)	0.369	0.852	1939	-15.9	22.9	0.878	14.6	19
				1890	-12.7	35.2		21.5	
				1841	- 9.77	49.1		27.0	
				1547	6.35	<0		12.7	
				1449	11.5	6.69		19.5	
				1351	15.4	12.0		21.0	
		0.339	0.839	1939	-15.9	28.3	0.880	13.9	17
				1890	-12.7	42.5		19.6	
				1841	- 9.41	66.6		28.8	
				1351	15.9	6.59		19.0	
				1302	17.7	8.28		19.2	
				1253	21.8	2.08		10.4	
		0.293	0.813	1939	-18.1	20.9	0.840	15.1	16
				1890	-15.9	24.3		16.0	
				1841	-12.7	37.8		22.9	
				1449	8.47	1.61		18.2	
				1351	12.7	10.7		21.9	
				1302	15.9	7.87		15.3	
				1253	18.1	7.77		14.2	
		0.233	0.772	1841	-14.9	34.3	0.830	13.4	16
				1743	-11.5	35.9		6.30	
				1714	- 8.47	66.8		11.0	
				1694	- 6.68	94.1		13.8	
				1351	9.77	6.87		50.1	
				1253	16.9	1.98		17.3	
				1204	18.1	5.13		20.1	
				1155	23.6	<0		6.05	

Table III-7. (continued)

Bed-particle diameter (micron)	Moving-sphere diameter (cm)	Fluidizing velocity (cm/sec)	Void fraction ϵ	External weight (dyne)	Moving-sphere velocity (cm/sec)	Viscosity [Based on ϵ] (cp)	Revised void fraction ϵ_f	Revised viscosity (cp)	Mean viscosity (cp)
95.5	1.27 (smooth)	0.168	0.715	1841	-15.9	49.6	0.777	24.0	23
				1743	-12.7	55.8		21.4	
				1253	12.7	<0		22.3	
		0.109	0.643	1743	-18.1	29.5	0.694	17.3	27
				1694	-15.9	38.1		19.2	
				1645	-12.7	59.1		30.8	
				1596	-10.6	71.6		33.1	
				1253	3.91	<0		74.0	
				1204	8.47	<0		27.2	
				1155	10.2	3.68		33.0	
191	1.27 (smooth)	0.739	0.768	1841	-14.1	51.2	0.793	37.5	43
				1743	- 9.76	71.8		50.1	
				1351	7.06	15.9		45.3	
				1253	11.6	21.5		36.8	
		0.589	0.727	1743	-10.6	90.6	0.775	50.2	44
				1645	- 7.46	100.0		38.1	
				1253	7.46	35.6		100.0	
				1155	13.5	17.4		43.1	
		0.441	0.679	1645	-11.9	53.4	0.714	31.9	33
				1547	- 7.26	84.7		40.1	
				1253	8.45	<0		12.1	
				1155	11.3	10.5		28.0	
		0.293	0.621	1547	-14.1	23.9	0.603	32.9	110
				1449	- 7.06	80.7		106.0	
				959.3	6.35	192.0		158.0	
				861.3	9.53	152.0		150.0	

Table III-7. (continued)

Bed-particle diameter (micron)	Moving-sphere diameter (cm)	Fluidizing velocity (cm/sec)	Void fraction ϵ	External weight (dyne)	Moving-sphere velocity (cm/sec)	Viscosity [Based on ϵ] (cp)	Revised void fraction ϵ_ℓ	Revised viscosity (cp)	Mean viscosity (cp)
191	1.31 (rough)	0.739	0.768	2037	-19.5	21.9	0.779	19.7	40
				1890	-12.1	48.6		40.4	
				1841	- 9.75	60.5		50.6	
				1449	6.69	22.4		37.4	
				1351	10.6	29.8		39.2	
		0.589	0.727	2037	-19.5	31.5	0.740	28.1	26
				1841	-10.6	77.0		68.1	
				1351	9.06	16.2		26.5	
				1253	13.4	16.7		22.5	
		0.441	0.679	1939	-19.5	26.9	0.686	25.0	30
				1841	-15.9	35.4		31.9	
				1351	5.44	3.49		12.4	
				1253	9.07	23.2		30.1	
				1204	10.6	29.1		34.8	
		0.293	0.621	1939	-21.2	29.6	0.621	29.6	31
				1841	-18.1	34.8		34.8	
				1253	2.82	48.3		48.3	
				1155	8.46	32.0		32.0	
		0.218	0.582	1753	-15.9	46.2	0.582	46.2	51
				1645	-12.7	58.0		58.0	
				1155	3.30	98.4		98.4	
				1057	8.46	51.7		51.7	
		0.131	0.518	1547	-11.3	84.2	0.495	100.0	100
				1449	- 9.25	76.2		100.0	
				861.3	8.46	112.0		81.1	
				763.3	9.53	146.0		119.0	

mean intersticial fluid velocity (given by U/ε), where the sign depends upon whether the sphere rose with or fell against the rising fluid stream. The standard sphere drag correlation is assumed for $C_D(Re)$. [Refer to Zenz (Z1), Figure 6.3]

An apparent drag coefficient may be defined for the solid particles by:

$$C_D(Re_s) \equiv \frac{8 F_s}{\pi \rho_b U_s^2 d_s^2} \qquad (III-18)$$

where the Reynolds number for moving-sphere motion through the fluidized particles is:

$$Re_s \equiv \frac{\rho_b U_s d_s}{\eta_a} \qquad (III-19)$$

and ρ_b is the mean bed density $\varepsilon\rho + (1 - \varepsilon)\rho_s$.

The $C_D(Re)$ relation for the moving-sphere interaction with the fluidized particles is, as for fluid drag, assumed to conform to the standard sphere drag correlation given in Figure 6.3 of Zenz (Z1). With the measured terminal sphere velocity U_s a function of external weight w, the apparent viscosity of the bed η_a may now be calculated by Eqs. (III-15) - (III-19).

The viscosity values obtained by this procedure are listed in column 7 of Table III-7. A clear asymmetry about the point of zero weight difference is discernible. The rising-sphere viscosities are a great deal larger than the falling-sphere values, and the largest value occurs just above the balance point. The balance points were calculated using the void-fractions (given in column 4) determined from the bed

expansion data. An obvious possibility is that the sphere tends to see a local particle concentration which differs from the average value throughout the bed. Proceeding on this basis a trial-and-error method was employed to determine for each bed-state that value of local void-fraction which yielded the most self-consistent set of apparent viscosities. The results are given as columns 8 - 10 in Table III-7. Clearly, the approach met with relatively good success, since by the adjustment of the void-fraction a single value for apparent viscosity emerged for each bed state and a plausible trend of viscosity with bed void-fraction could be perceived. In the next section these moving-sphere viscosity results are compared with our Brookfield viscosities for the same systems.

3. Comparison of the Brookfield and Moving-Sphere Results

The results of both the Brookfield and moving-sphere viscosity measurements for the 95.5 and 191μ systems are plotted as a function of fluidizing velocity in Figures III-16 and III-17. The general agreement is seen to be quite good. The slightly larger and more erratic values for the moving-sphere results are not surprising in that, moving along the axis of the bed, the sphere is more strongly influenced by any vertical convective currents that exist. In addition, during each measurement the moving-sphere travels the length of the bed, consequently encountering any nonhomogeneities that may be present. Conversely, the rotating Brookfield-viscometer spindle remains in one location throughout a measurement, and its geometry was designed to minimize the effect of vertical convective currents. Therefore, the accord achieved between the results of the two measurement techniques suggests both that a true measure of viscosity was effected and that relatively homogeneous fluidization was achieved.

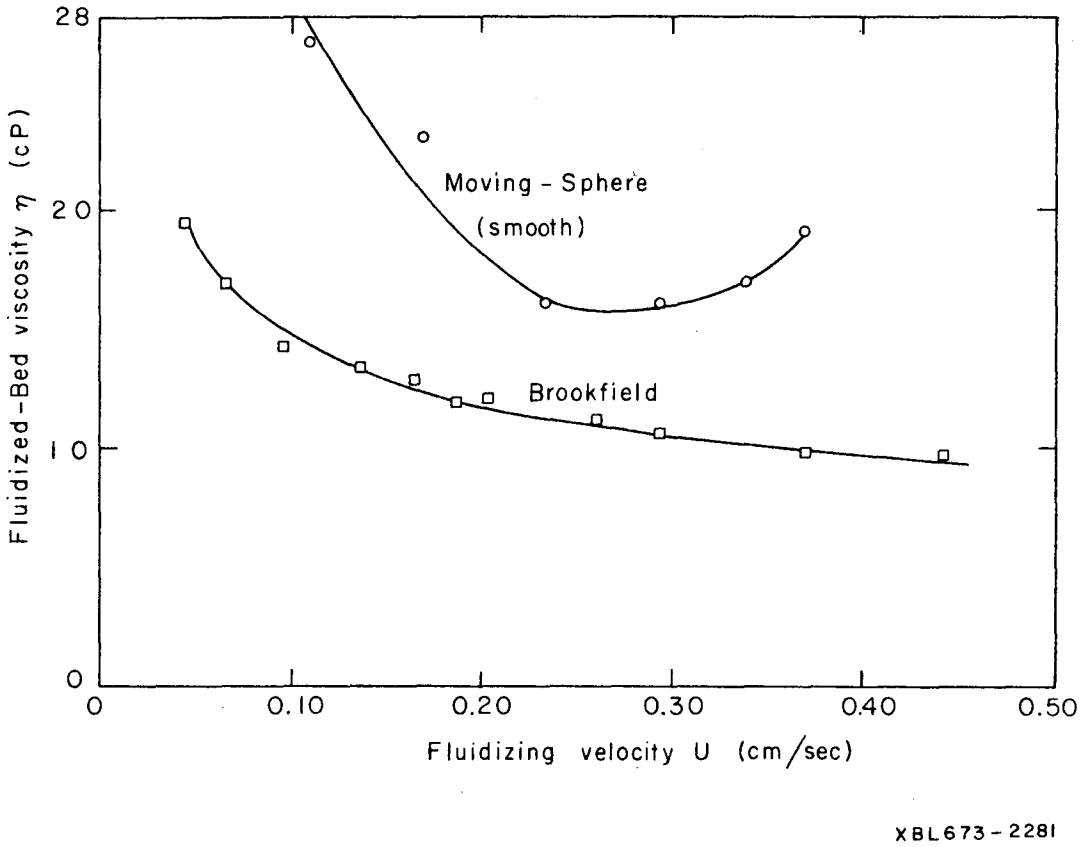

Fig. III-16. Comparison of Brookfield and moving-sphere viscosity data for 95.5μ particle beds.

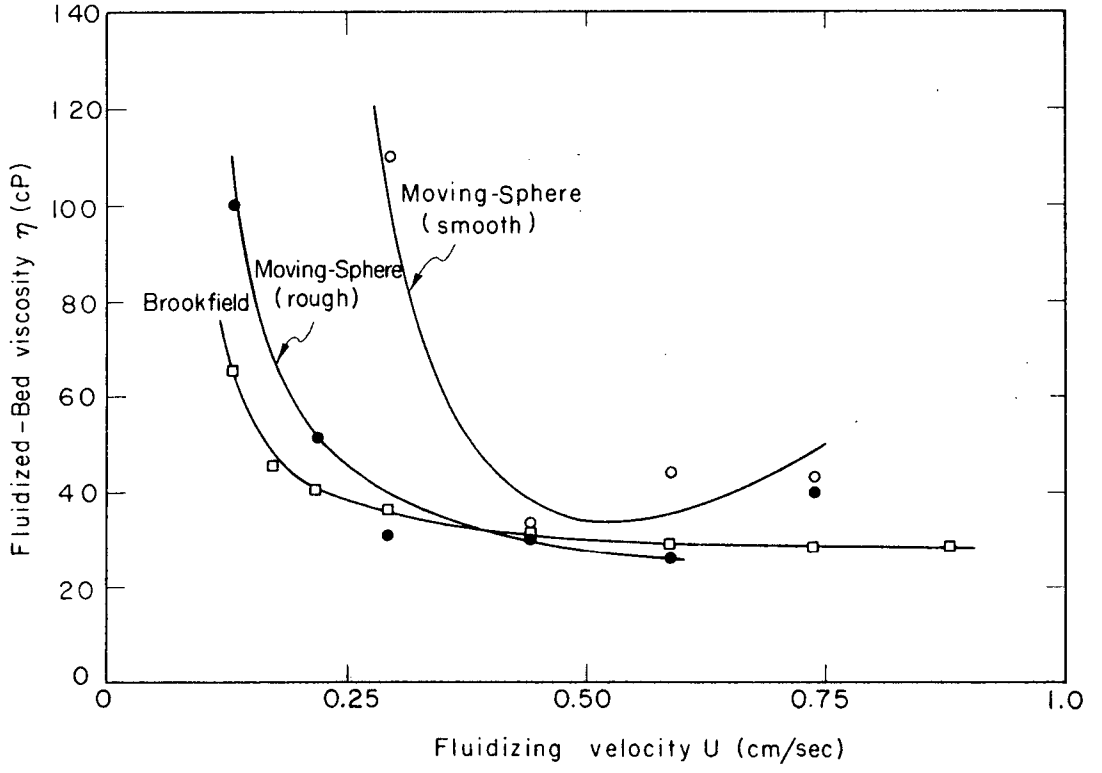

XBL673-2282

Fig. III-17. Comparison of Brookfield and moving-sphere viscosity data for 191μ particle beds.

D. Miscibility Measurements

1. Equipment Description

The sampling device used for our miscibility measurements was inserted vertically upward through the bottom column section, separated from the distributor material by the aluminum tubing provided. The device, shown in Figure III-18, was located two inches off the column centerline. Thus, the two-inch offset of its upper section of 5/8-inch copper tubing enabled, by rotation, sampling at any radial distance from the centerline to within 1/4-inch of the column wall. In addition, its 4-ft. straight section of 3/4-inch brass tubing (with 1/8-inch wall) permitted sampling at bed heights from 6 inches to somewhat over 3 feet.

The Teflon cap of the sampling tube was controlled by the length of #33 piano wire passing, within the 1/8-inch copper tubing, up the interior of the sampling tube. The copper tubing was centered at three points by a triangular-strut construction. The Teflon cap could be raised and lowered by the screw-type control mounted at the lower end of the tube.

The 1/2-inch line at the bottom of the sampling tube was controlled by a special self-cleaning valve. Following a sampling, it was attached to the collecting device shown in Figure III-19. The line was then opened and the sample drained into the collector. The 400-mesh stainless-steel screen in the collecting device served to separate the spheres from the fluidizing water. The 1/4-inch tubing on the side wall was attached to the house vacuum to hasten the drainage process; when separation was complete, the water was removed through the spigot at the bottom of the

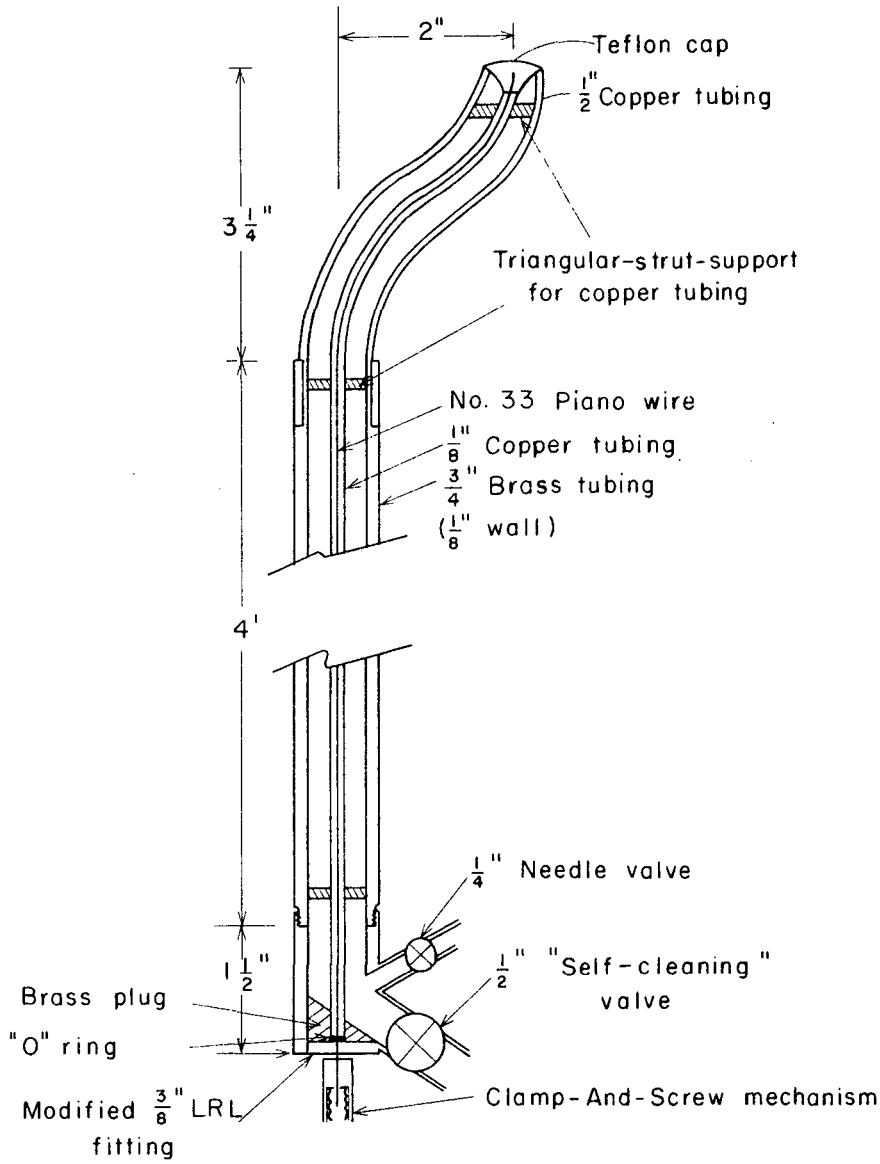

Fig. III-18. Sampling tube.

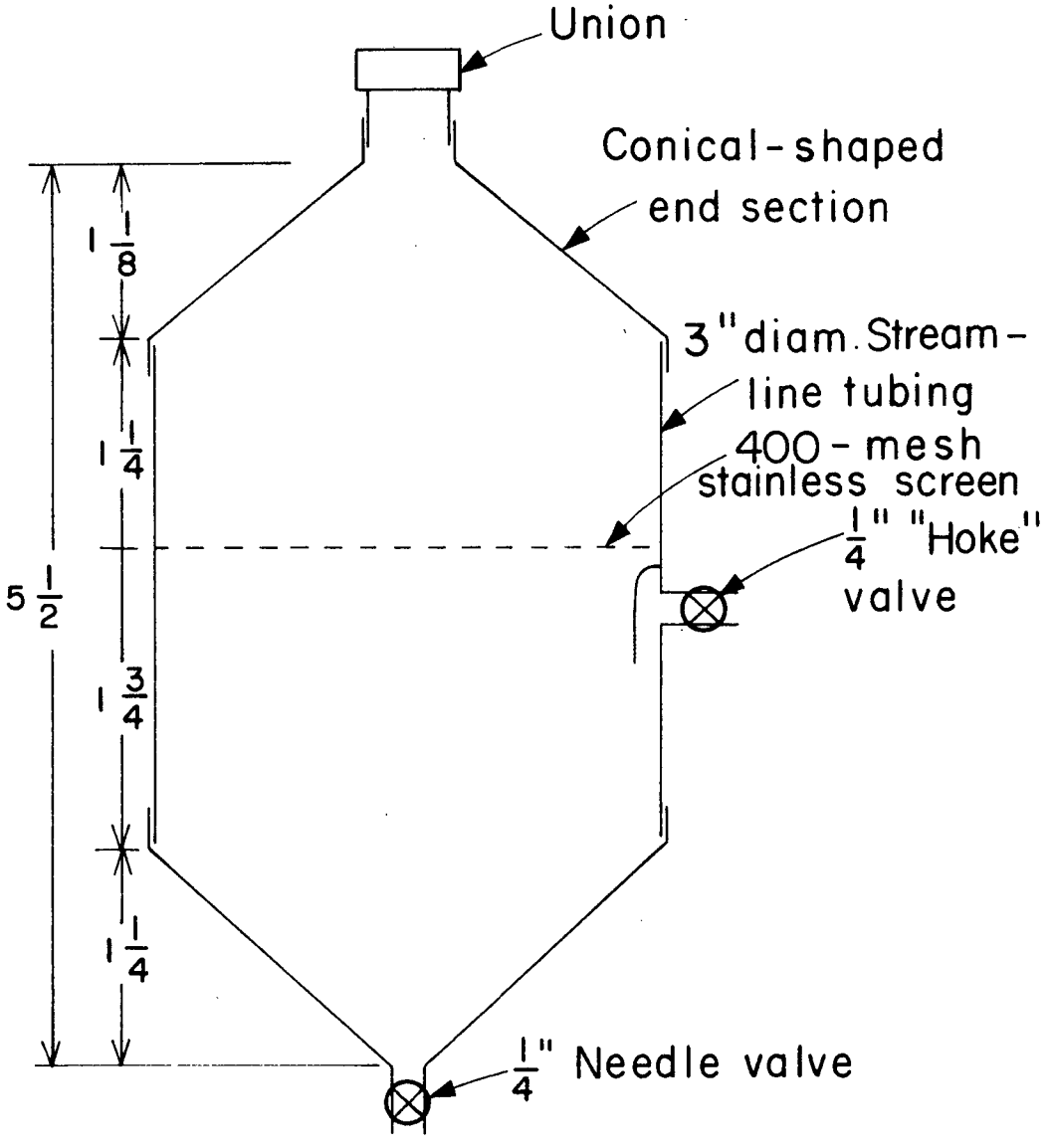

Fig. III-19. Collecting device.

collector. The 1/4-inch valve at the lower end of the sampling tube was next opened for the first of two water washes.

The conical shape of the top and bottom of the collector was designed for ease of particle and fluid removal. The union at its upper end permitted detachment of the collecting device when sampling in the lower part of the bed. The sampling tube could then be lowered until its lower end contacted the floor, which corresponded to a bed height of 6 inches for the tube opening.

2. Operational Procedure

Prior to obtaining a sample, the sampling tube was evacuated by connecting it to the house vacuum line. The Teflon cap was then raised, and 10 seconds allotted for the local fluidized liquid-solid mixture to enter the tube. The Teflon cap was then firmly secured, and the sample drained into the collecting device through the 1/2-inch line. The house vacuum to the collecting device was maintained during drainage to assist the gravity flow from the sealed sampling tube, and to promote rapid liquid-solid separation.

After complete drainage, the water was removed via the bottom spigot to prevent its level nearing the height of the vacuum line. The sampling tube was then reevacuated, and the 1/4-inch valve opened to conduct a water wash. The draining procedure was repeated, and another water wash carried out to insure that all solid material had been removed from the sampling tube.

The drained sample was next removed from the collection device and segregated into its two size fractions by sieving. The particles were then oven-dried for several hours at 120°C, and weighed on a Mettlar balance.

3. Measurement Results and Analysis

Miscibility measurements were made for three binary systems -- 95.5/191, 142/191, and 191/270μ. The results are presented in Table III-3. The mole-fractions given in the table are calculated from the measured weight-fractions by equations of the form:

$$x_{11} = \left[1 + \frac{w_{21}}{w_{11}}\left(\frac{v_{p1}}{v_{p2}}\right)\right]^{-1} \qquad \text{(III-20)}$$

where x_{11} denotes the mole-fraction of type-1 particles in phase 1, i.e., that phase in which type-1 particles predominate; w_{11} and w_{21} represent, respectively, the weight-fraction in phase 1 of type-1 and type-2 particles; and v_{p1} and v_{p2} are the particle volumes of type-1 and type-2 particles.

The interface between phases could be visually located, as illustrated by the photograph of a 52.2/270μ interface given in Figure III-20. In most instances, two samples were taken from each phase -- one well removed from the interface and the other within 2 to 3 inches of it. The samples taken near the interface confirmed its location, and indicated that the concentration was relatively uniform within each phase to within a few inches of the interface. A few data points from near 142/191μ interfaces, however, were midway between the corresponding bulk phase data, suggesting difficulty in interface definition for that system.

The changes in bed height (or volume) attributable to mixing are given in column 13 of the table. These figures represent the differences between the measured bed heights and the equivalent-total heights of type-1 and type-2 particles fluidized separately at the same flow

Table III-8. Miscibility data.

Run	System	Fluidizing velocity (cm/sec)	Interface height (inches)	Bed height (inches)	Sampling[a] height (inches)	Lower phase W_{11}	Lower phase W_{21}	Upper phase W_{12}	Upper phase W_{22}	X_{11}	X_{12}	Height Change due to mixing (inches)
35	191/95.5 (1)/(2)	0.293	9.772	20.5	8	127.582	3.2938			0.829		-2.16
36	"	0.428	10.147	27.897	15				66.7358	1.000	0	-3.10
		"	"	"	9	133.8730						
		0.192	8.397	15.647	10			1.6507	131.958	0.880	0.012	-4.60
		0.182	8.147	14.782	7	144.3881	2.4728					
41	"	0.371	13.397	28.647	23			0.0768	59.1675	0.976	-	0.19
		"	"	"	15			5.9540	80.4141	-	0.009	0.69
		"	"	"	11	80.8826	0.2494					
		"	"	"	8	83.0507	0.1377			0.987	-	1.19
		0.292	11.709	22.115	9	172.9866	0.4619			0.979	0.001	-0.58
		"	"	"	15			0.4229	104.5582			
		0.218	10.272	17.897	13			5.8260	128.8124	0.979	0.006	-0.66
		"	"	"	8	105.3757	1.6331					
		0.157	9.084	14.647	7	195.9534	16.6289			0.596	0.001	-0.96
		"	"	"	11½			0.9888	91.7616			
42	"	0.183	10.647	19.897	14			0.8998	122.3676	0.931	0.001	0
		"	"	"	7½	53.5702	0.4992					
		"	"	"	"	47.8384	0.6975			0.896	-	0.46
		"	"	"	"	47.5947	0.7321			0.890	-	0.90

Table III-8. (continued)

Run	System	Fluidizing velocity (cm/sec)	Interface height (inches)	Bed height (inches)	Sampling height (inches)	Lower phase W_{11}	Lower phase W_{21}	Upper phase W_{12}	Upper phase W_{22}	X_{11}	X_{12}	Height change due to mixing (inches)
37	191/142	0.663	-	37.397	30	-	-	-	30.1268	-	0.226	0.202
	(1)/(2)	"		"	12	-	-	46.8891	66.1714			
		0.369	13.647	23.397	16	-	-	17.5140	114.9922	0.935	0.059	-0.84
		"	"	"	10	156.01	4.4605					
		0.739	-	37.397	18	80.7870	6.8584	-	-	0.882	-	-2.54
		0.218	10.647	16.522	13	-	-	54.8748	103.1525	0.799	0.179	-1.33
		"	"	"	7½	106.7612	11.0229	-	-			
38	"	0.813	22.397	45.397	30	-	-	0.9457	17.8179	0.983	0.021	5.42
		"	"	"	30	-	-	8.5116	69.1498	-	0.048	5.72
		"	"	"	24	-	-	0.1666	6.5625	-	0.10	6.01
		"	"	"	20	73.1077	5.5644	-	-	0.844	-	6.31
		"	"	"	10	49.1416	0.3461	-	-			
		0.517	16.397	23.959	12	42.8367	1.3878	-	-	0.927	0.007	-1.67
		"	"	"	20	-	-	0.5044	32.4332	-	0.006	-1.21
		"	16.897	23.772	20	-	-	3.2365	80.1001	-	0.016	-0.76
		"	"	"	20/90°	-	-	1.8069	86.4876	-	0.009	
		"	"	"	20/180°	-	-	1.5712	86.3009			-0.30
		0.222	10.147	14.897	12	-	-	17.4036	27.1201	0.942	0.209	-0.15
					7	78.0286	1.9758	-	-			
39	"	0.118	9.272	14.709	7	53.1813	5.8247	-	-	0.790	0.190	-0.65
		"	"	"	10½	-	-	78.0401	91.4909	-	0.260	-0.47
		"	"	"	12½	-	-	19.2641	33.7103			

Table III-8. (continued)

Run	System	Fluidizing velocity (cm/sec)	Interface height (inches)	Bed height (inches)	Sampling height (inches)	Lower phase W_{11}	Lower phase W_{21}	Upper phase W_{12}	Upper phase W_{22}	X_{11}	X_{12}	Height change due to mixing (inches)
40	270/191	0.963	18.897	37.647	30	-	-	3.8783	88.2557	0.931	0.015	
	(1)/(2)	"	"	"	21	-	-	7.7772	80.2887	-	0.33	
		"	"	"	15	60.4666	12.1014	-	-	0.660	-	
		"	"	"	8	131.0420	3.4450	-	-			
		0.813	15.147	31.897	7	62.9898	1.6577	-	-	0.931	0.004	
		"	"	"	12	45.8994	2.4901	-	-	0.867	-	
		"	"	"	18	-	-	61.9169	68.8125	-	0.242	
		"	"	"	25	-	-	0.9309	89.9130			
		0.664	13.397	27.472	24	-	-	0.6229	71.1272	0.871	0.003	
		"	"	"	15½	-	-	53.9283	85.5631	-	0.182	
		"	"	"	10½	90.5465	8.2566	-	-	0.795	-	
		"	"	"	7	73.2364	3.8254	-	-			
		0.517	13.662	24.897	18	29.6777	28.8377	-	-	0.267	-	-0.57
		"	"	"	18/90°	-	-	12.7352	92.2350	0.768	0.047	-0.57
		"	"	"	9	77.1242	8.6281	-	-	0.870	-	-0.18
		"	"	"	9/90°	56.4582	6.0339	-	-			
		0.370	10.897	21.147	8	47.4800	4.8382	-	-	0.776	0.027	-0.19
		"	"	"	8/90°	62.1686	7.9219	-	-	0.735	-	0.02
		"	"	"	16	-	-	4.0863	52.4298			
		"	"	"	16/90°	-	-	10.3870	46.9695	-	0.073	0.24
		0.192	10.147	17.647	12	39.4342	37.0835	-	-	0.273	-	0.44
		"	"	"	12/90°	34.7555	25.6012	-	-	0.249	-	0.61
		"	"	"	7	48.3696	19.7153	-	-	0.465	-	0.79
		"	"	"	7/90°	51.3347	18.1654	-	-	0.500	-	0.97

[a]Measured at center line, except where indicated.

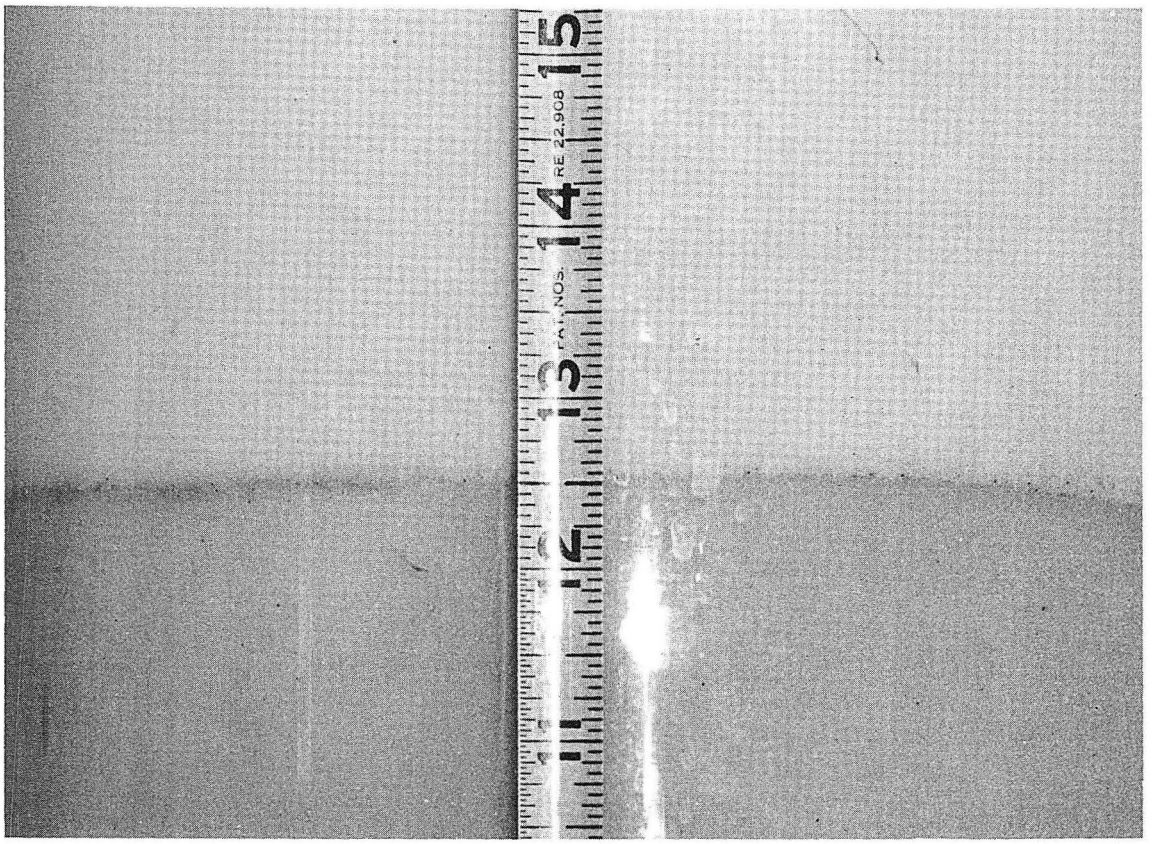

ZN-4078

Fig. III-20. Two-phase system at u = 0.055 cm/sec: upper phase, 52μ beads, ϵ = 0.748; lower phase, 270μ beads, ϵ = 0.469.

conditions. The decrease in the total particle count due to sample removal was taken into account. The data indicate that very little, if any, volume change occurred upon mixing.

Another parameter of interest, potentially determinable using our sampling device, is the local particle concentration, as compared to the mean bed concentration. During our experiments, however, it proved difficult to completely close the Teflon cap. Strong tension on the piano wire provided a tight seal, but then the wire tended to break. Therefore, a lower tension was applied which was sufficient to completely seal the tube to further solid-material entrance and permitted very little water leakage. With this mode of operation, it was not possible to accurately assess the local particle concentration.

The mole-fraction of large particles in each phase is plotted as a function of fluidizing velocity in Figures III-21, III-22, and III-23. The data for the two phases appear to be relatively symmetric and indicate that the mutual solubility decreases as the velocity increases. The symmetry is more clearly displayed by the solubility plots given in Figures III-24, III-25, and III-26. With the exception of the 142/191u data points evidently taken at the interface, the solubility data for both phases can be fit by a single curve, as indicated in the figures.

The equilibrium which is established at each fluidizing velocity represents a balance between the familiar diffusive mixing and the segregating effect of fluid drag on the different particle types. As the fluid velocity is increased the drag forces come to predominate. This is a continuous process where only particle size differences are involved. Furukawa and Ohmae's data (F2) for different-size sand

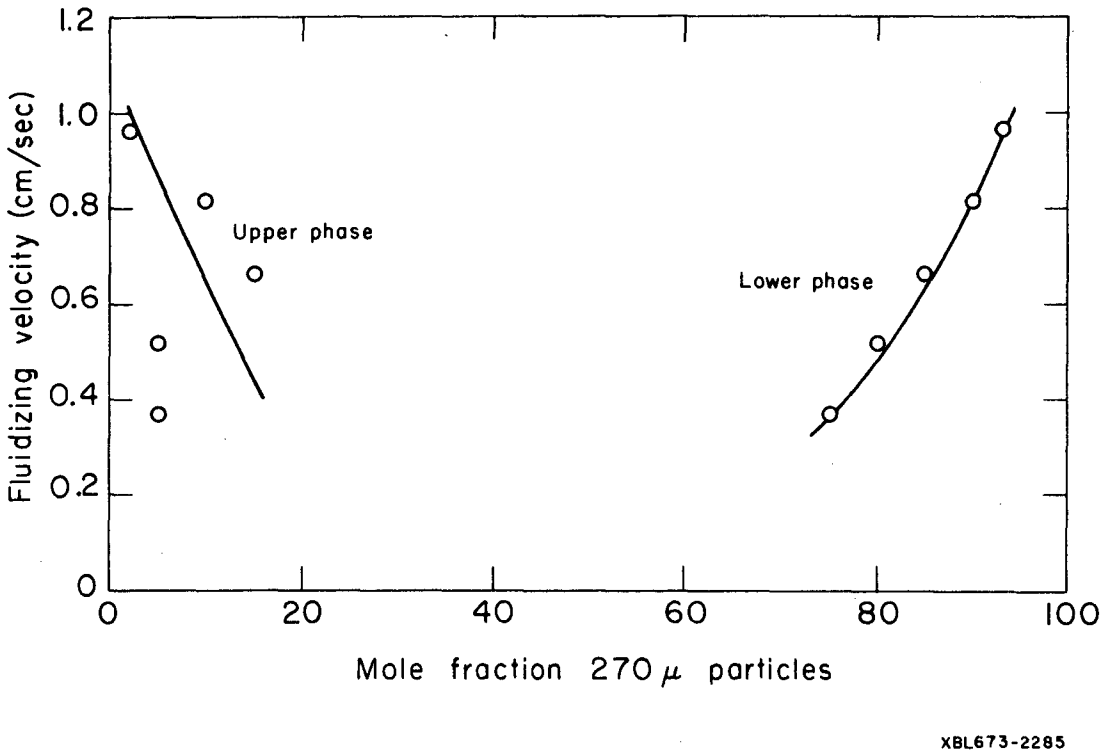

Fig. III-21. Velocity dependence of the mole-fraction of 270μ particles in the 191/270μ system.

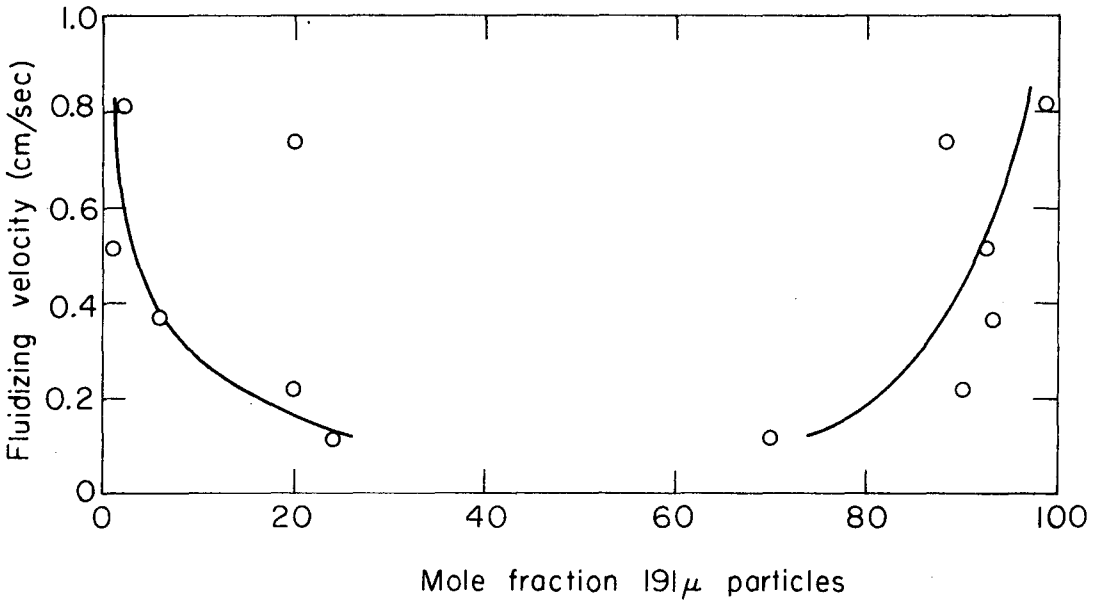

XBL673-2286

Fig. III-22. Velocity dependence of mole-fraction of 91μ in 142/191μ system.

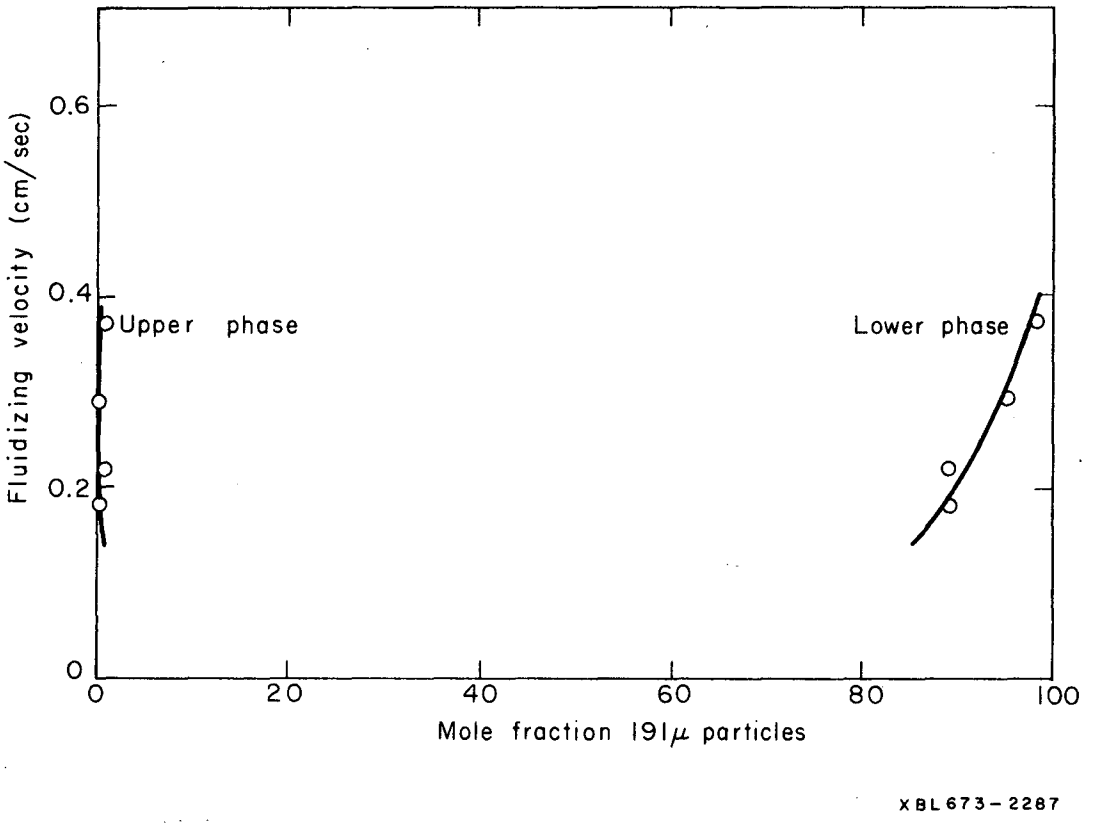

Fig. III-23. Velocity dependence of the mole-fraction of 191μ particles in a 95.5/191μ system.

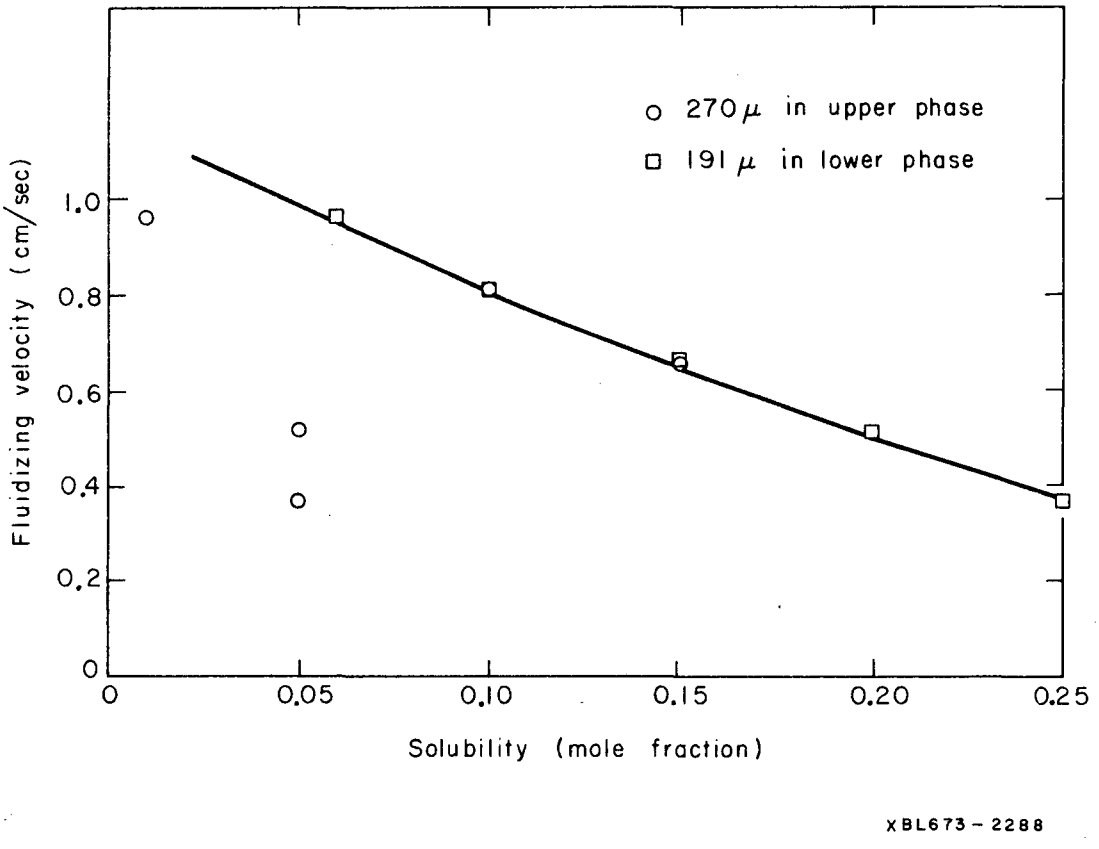

Fig. III-24. 191/270μ solubility dependence upon temperature
o 270μ in upper phase □ 191μ in lower phase.

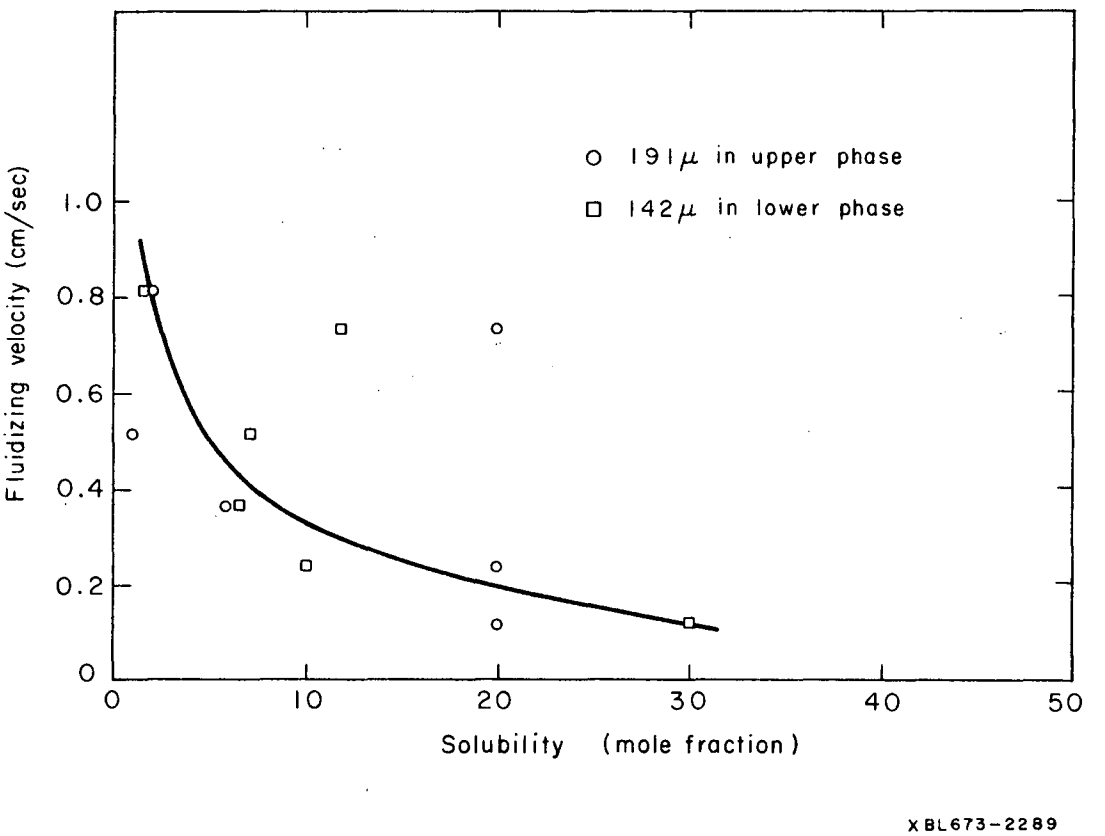

Fig. III- 25. 142/191μ solubility dependence upon temperature
o 191μ in upper phase □ 142μ in lower phase.

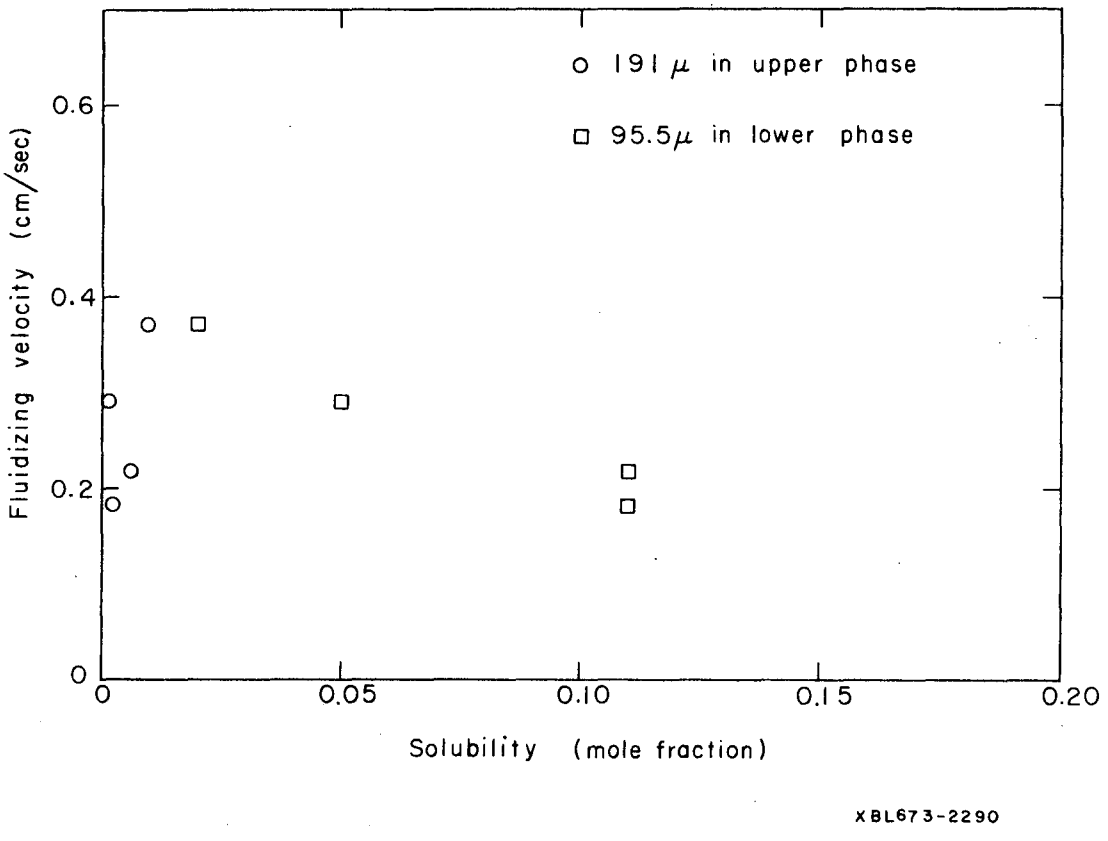

Fig. III-26. 95.5/191μ solubility dependence upon temperature
o 191μ in upper phase □ 95.5μ in lower phase.

particles exhibit the same behavior as our own data. Their results for the 755/200μ and 755/160μ charcoal-sand systems, with the charcoal larger and lighter, however, appear to behave in an opposite manner. This is an inversion phenomenon, as may be shown by considering Eq. (I-85) for suspended particles:

$$\frac{u_2}{u_1} = \sqrt{\left(\frac{\rho_2-\rho}{\rho_1-\rho}\right)\frac{d_2}{d_1}\frac{C_{D_1}}{C_{D_2}}} \qquad (I\text{-}85)$$

For the charcoal ρ_2=1.2 g/cc and d_2=755μ; and for the sand ρ_1=2.65 and d_1=200μ (or 160μ). At low velocities where $C_D \propto d^{-1}$, $u_2 > u_1$ so that the charcoal particles are at the bottom of the bed. At high velocities C_D approaches a constant value (independent of d): thus $u_2 < u_1$ and the sand particles move to the bed bottom. Consequently, as the velocity is increased from a low value, an intermediate region, in which nearly total mixing occurs, is encountered. Further increase in velocity brings passage through an inversion point followed by increasing segregation with the heavier particles now on the bottom. Furukawa and Ohmae's data for the charcoal-sand system, therefore, lay below the inversion point for that system.

4. Proposed Use of Sampling Tube

The techniques and apparatus used for obtaining the miscibility data also could be employed in an experimental assessment of self-diffusion. The only operational changes would be the marking and deployment of tracer particles in the bulk fluidized phase and the taking of samples at well-defined times. In addition, Sutherland (S8), who used a similar sampling technique for mixing studies in gas-fluidized beds, stated that it is statistically necessary to acquire simultaneous samples at several points in the bed. The importance of more than one sample point is a function of the smoothness of fluidization, however, and should be less necessary in a liquid-fluidized bed. If desired, a second sampling tube could be easily employed in our system.

E. Surface - Wave Measurement

The objective of this part of the study was to evaluate surface-tension effects in fluidized beds by the ripple, or surface-wave, technique. Although experimental difficulties precluded other than a few visual measurements of surface-wave properties, a description of the entire system is felt to be appropriate since future work may be done along these lines.

1. Equipment Description

A schematic diagram of the equipment assembled for use in the surface-wave measurements is given in Figure III-27. The Decker unit depicted is an instrument which converts minute changes of capacitance (1-50 mmf) into large analogous output voltages (30 volts maximum); it utilizes an ionization transducer to perform this function. The output from the Decker (Model 904-1 Delta) unit was sent to a Brush (Model BL-212) oscillograph, which was capable of chart speeds up to 125 mm/sec and voltage amplification ratios up to 2000.

The initiator is a push-button switch which energizes the solenoid control mechanism for the drop rod, and simultaneously causes a "zero" time mark to be made on the oscillograph record. The support ring is a 3/4-inch-high collar, expansion fitted into the column. Teflon sleeves, seated within vertically-oriented cylinders attached to struts from the collar, provided lateral support at the approximate midpoints of both the drop rod and capacitor-lead rod.

The drop rod was centered in the column as accurately as possible, because radial symmetry improves the precision and ease of measurements.

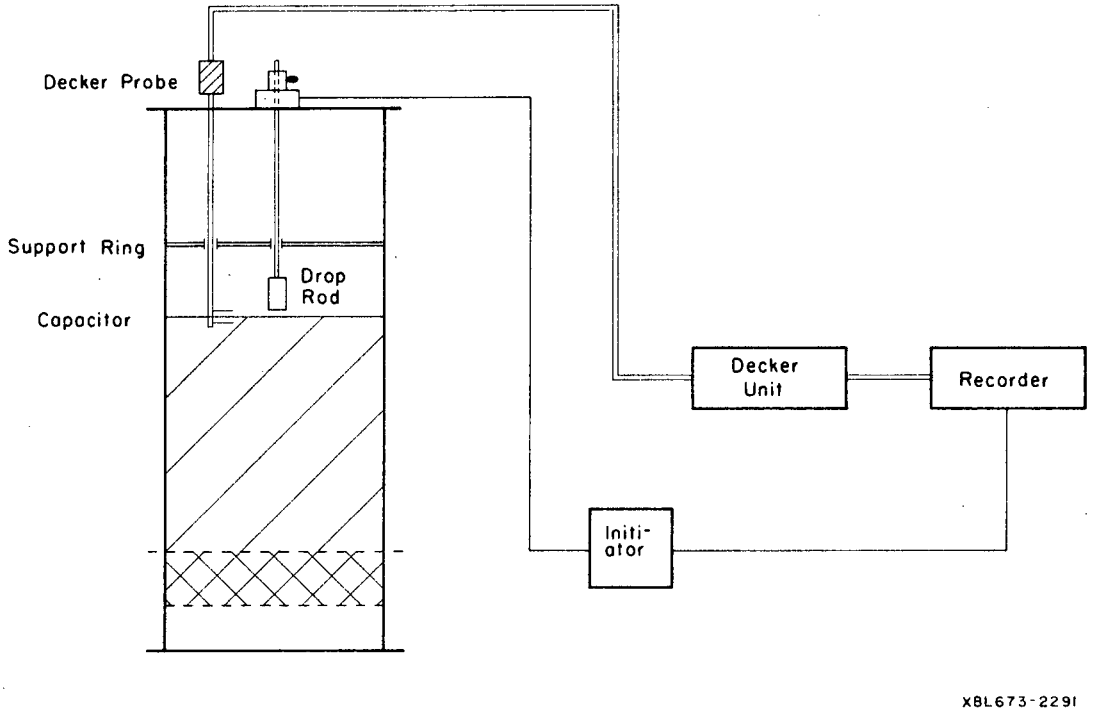

Fig. III-27. Surface-wave apparatus.

The 1-1/8-inch-long by 7/8-inch-diameter stainless-steel cylinder, which creates the surface-wave motion when dropped vertically-downward through the bed surface, was affixed to a 65-inch-long segment of 3/8-inch stainless-steel rod. The motion of the rod, which was separable into two equal-length sections for ease of handling, was controlled by the mounting and sleeve combination shown in Figure III-28. The rod passed through the 3/8-inch channel in the sleeve, and was held to it by the set screw; thus, the cylinder height could be easily adjusted. The mounting was secured to the top plate of the calming section by four screws, and was leveled prior to each measurement. A solenoid control mechanism and pin were emplaced where indicated on the side of the mounting. To set the cylinder for a measurement, the rod sleeve was raised 1.0 or 1.25-inches and the pin inserted into one of the slots in its side. To make the measurement, the solenoid was energized, causing pin withdrawal, thus permitting the cylinder to fall through the bed surface. The Teflon sleeve in the mounting enabled the rod to fall smoothly and accurately, and the felt pad softened the rod-mounting impact.

The capacitor was mounted 3 inches from the bed centerline; this allotted ample distance for wave development, but did not lead to interference effects from the column wall. Additional detail for the capacitor and its lead rod is given in Figures III-29a and III-29b. The slip collar around the top of the lead rod permitted matching the capacitor height to that of the bed surface for each measurement. The capacitor output was transmitted by low-capacitance coaxial cable (65 pf/ft) to the Decker probe mounted at the upper end of the 3/8-inch stainless-steel lead rod; low-capacitance connectors were used at all points. The

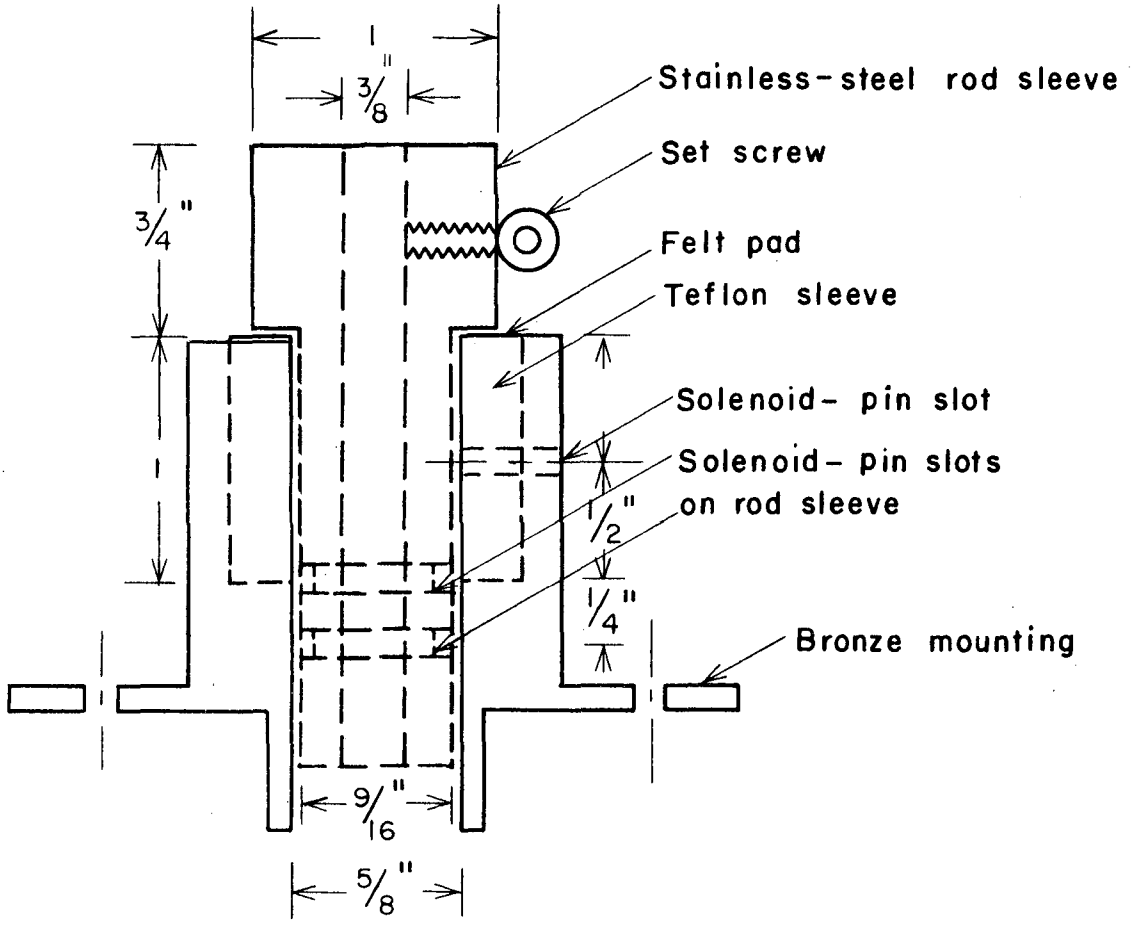

Fig. III-28. Drop-rod sleeve and mounting.

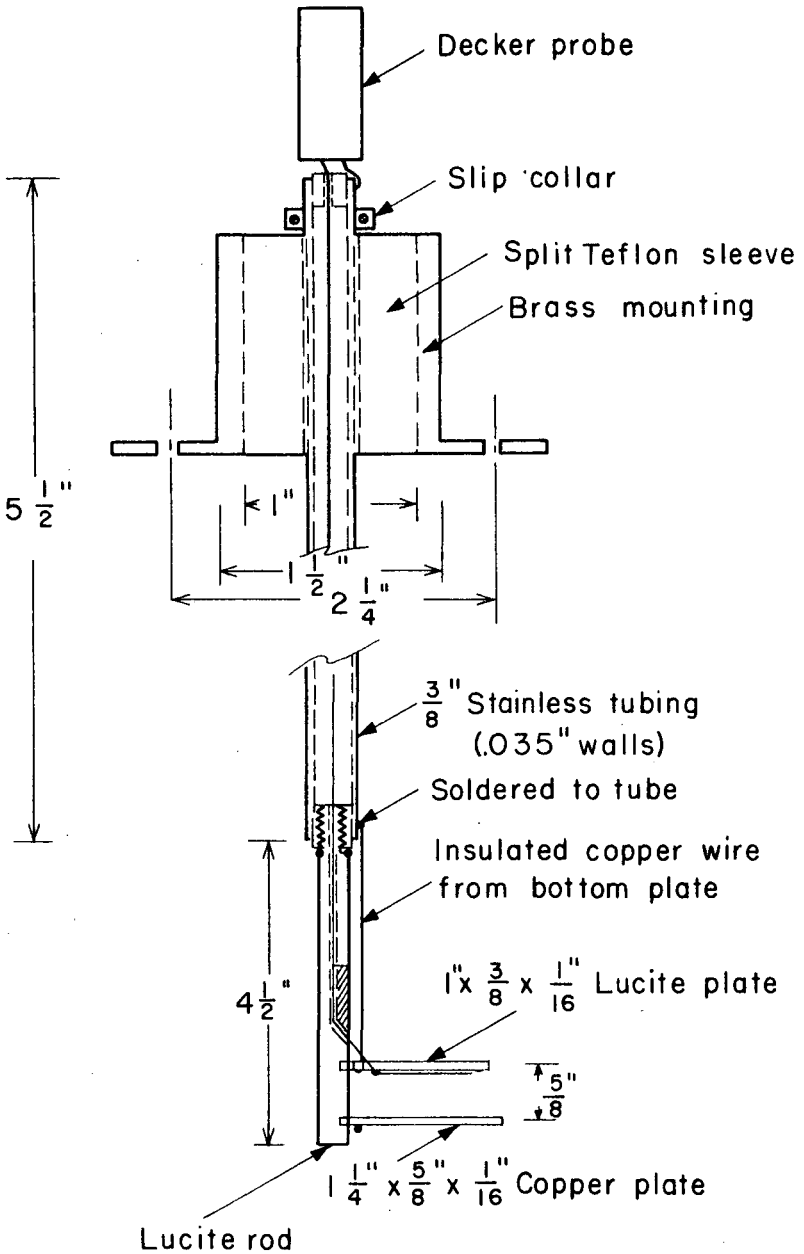

Fig. III-29a. Capacitor, lead rod, and mounting.

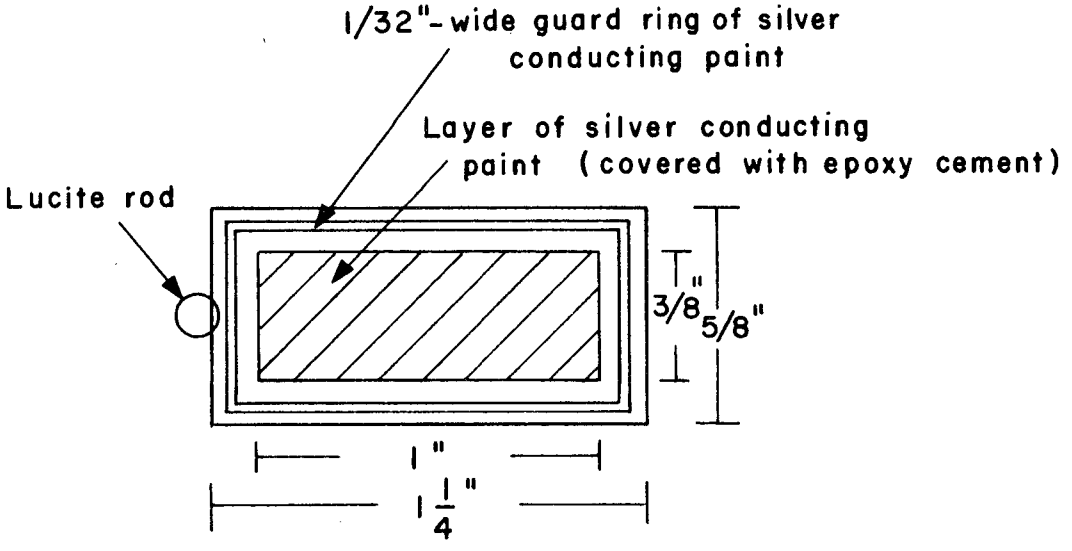

XBL673-2294

Fig. III-29b. Top electrode view showing nature of guard ring.

utilization of such low-capacitance equipment helped to alleviate the problem of capacitor-signal degradation introduced by the long lead-rod length (66 inches) necessary for stationing the capacitor at the less-expanded bed surfaces. In addition, a guard section on the capacitor plates minimized capacitor edge losses, thus strengthening the original signal.

2. Operational Procedure

The nominal procedure for using the surface-wave measuring apparatus is as follows. Measurement is started by depressing the initiator, which energizes the solenoid, and simultaneously marks the "zero" time on the Brush-recorder oscillograph. The drop rod then falls, and the cylinder penetrates the bed surface. The resulting sequence of surface waves is monitored by the capacitor stationed at the bed surface. The output from the capacitor is transformed by the Decker unit into an equivalent voltage, which is then transmitted to the Brush oscillograph and recorded on its high-speed print out.

Since the capacitor did not successfully perform its function, the wave motion was monitored visually during the actual measurements. The times of intersection with the column wall of the first two waves created by the dropping cylinder were clocked with a hand-held stopwatch.

3. Measurement Results and Discussion

As mentioned, it was anticipated that a more thorough investigation of surface tension would be made than was actually effected. The use of the capacitor to monitor wave characteristics, i.e., speed and amplitude, depended upon the capacitor's sensitivity to changes in the dielectric constant of the particle-fluid medium (M5, D7). Unfortunately, dissolved electrolytes in the available (industrial) water supply led to a conductivity for the fluid medium that was too large to permit sensitive capacitance measurements. This problem is mentioned in Reference P10: "The difficulty of preventing contammination of liquids of higher dielectric constant has effectively prevented their use for capacitors." Future efforts to employ a capacitor to characterize waves in the fluidized bed must, therefore, use fluidizing fluids of low dielectric constant. In our case, the fluidization system should be modified to permit recycle and storage of such fluidizing fluids.

The results of the three visual measurements of surface waves in the 95.5μ system are reported in Table III-9. The wave frequency ν was ascertained from the time lapse between the first and second wave intersections with the column wall, the speed c was calculated from the time taken by the first wave to reach the wall, and the wave length λ equals c/ν.

As discussed on pp. 24-25, the equation for wave propagation in a deep fluid may be rearranged to yield an expression for surface tension:

$$\sigma = \frac{\rho\lambda}{2\pi}\left(c^2 - \frac{g\lambda}{2\pi}\right) \qquad (I-42)$$

Table III-9. Surface-tension measurements.

Particle diameter (micron)	Fluidizing velocity (cm/sec)	Void fraction, ϵ	Fluidized height (cm)	Frequency, $\nu(\text{sec}^{-1})$	Speed, C (cm/sec)	Wave length, λ(cm)	Surface tension, σ (dyne/cm)
95.5	0.248	0.781	66.3	0.7	3.81	5.44	4.12
	0.163	0.711	49.9	0.9	4.31	4.79	6.15
	0.097	0.625	40.0	1.2	4.7	3.82	7.69

where ρ is the fluid density. The second term in this equation pertains to gravity waves, which predominate at long wave length. In our system, however, the gravitational force upon the fluidized particle is balanced by the fluid-drag force, so that the effective gravitation force is zero. Eq. (I-42) then becomes:

$$\sigma = \frac{\rho \lambda c^2}{2\pi} \qquad \text{(III-21)}$$

Here the effective density ρ is the mass density of solid particles, given by:

$$\rho = (\rho_s - \rho_f)(1 - \varepsilon) \qquad \text{(III-22)}$$

The surface tension values listed in Table III-9 were calculated by Eq. (III-22). The values are of the same order of magnitude as those for hard-sphere-type liquids, e.g., argon at 85°K has a surface tension of 13.2 dyne/cm (H6).

IV. THEORY AND DISCUSSION

In this chapter a liquid model is chosen for use in the interpretation of fluidization phenomena. The fluidized-bed variable equivalent to thermodynamic temperature is then specified; and the experimental data presented in Chapter III, plus some diffusion data from the literature, are analyzed using statistical-thermodynamic relations. The comparison of our experimental data to that of other investigators was made in Chapter III, and will not be considered here, except when it bears upon the validity of our statistical-thermodynamic model.

A. Choice of Model

In Chapter II the motion of particulately-fluidized particles was said to be localized and isotropic. Further, the particles are clearly hard spheres, and move in a force field resulting from a balance between the expansive pressure of fluid drag and the cohesive pressure of gravity. All of these attributes may be contained within the square-well form of the cell model, termed the "smoothed-potential" by Prigogine (P3). Therefore, this intuitively satisfying model, the main points of which were given on pages 18 and 19 of the Introduction, serves as a logical starting place for the use of liquid theory to analyze fluidization phenomena.

The parameters in the smoothed-potential model are readily interpreted for the case of the fluidized bed. The diameter d of the fluidized particles can be directly measured; and the free volume v_f can be ascertained through observation of bed-volume expansion. The

third parameter, the characteristic energy of particle interaction $\omega(0)$, is not known directly, but its volume derivative (at constant temperature) can be obtained from the equation of state [see Eq. (X-32)]. The prime requisite for the use of the cell model to interpret fluidization phenomena, however, is the identification of the fluidized-bed equivalent of temperature. This will now be considered.

B. Energetic Equivalent of Temperature

The fundamental attributes of the thermodynamic function known as temperature are the following:

(a) It is a statistical quantity that must be the same for any two vicinal bodies.

(b) It is the integrating factor that converts the infinitesimal heat flux $\bar{d}Q$ into the differential of a function of state dS.

(c) It is formally identifiable with $(\partial W/\partial s)_{v,N}$ in the differential form of the fundamental relation for internal energy $W(s,v,N)$.

The first of these attributes introduces the concept of thermal equilibrium: if two particle systems are immersed in the same heat bath, and kept there, the temperatures of the two systems become the same. For such thermal equilibrium to occur in the case of dissimilar particle types, e.g., differing in size, shape, or density, the fluidization parameter equivalent to thermodynamic temperature must depend solely upon fluid properties, and not upon particle properties. This will be set as an essential requirement in our development of a nominal temperature function for the fluidized bed, to be designated θ.

It seems reasonable to identify the flow energy of the "ether" as the heat source of the fluidized bed (see p.70). A measure of the nominal temperature may be gained then in two equivalent ways. First, it is the temperature, in energy units, associated with the particles; alternatively, it is the effective thermal energy of the medium with which the particles are in equilibrium. Viewed from the latter standpoint the nominal temperature θ should be related to the kinetic energy of the ether, ρU^2. It will be shown through analysis of our viscosity data that

indeed θ is proportional to U^2. Invoking the requirement that θ depend solely upon fluid properties, which may be functionally stated

$$\Theta = \Theta(\rho, \mu, g, U) \qquad (IV-1)$$

dimensional considerations require that, if θ is proportional to U^2, it must be given by

$$\Theta = \Omega \frac{\mu^2}{\rho g} U^2 \qquad (IV-2)$$

where Ω is a numerical constant. The validity of this nominal-temperature function rests, of course, upon the extent of success achieved by its use in cell-model expressions to describe fluidized-bed properties, such as the viscosity behavior.

It is of interest to compare Eq. (IV-2) with the nominal-temperature expressions of the three other investigators, discussed in Chapter I (pp53 - 63), who have related fluidized beds to liquids. Furukawa and Ohmae (F2), basing their arguments upon a harmonic-oscillator model and empirical considerations, postulated that the nominal temperature should be proportional to μU. While this function exhibits the necessary independence from particle properties, a number of steps in its development are somewhat arbitrary; and is was not applied in a consistent manner to interpret their fluidized-bed experimental data on expansion, viscosity, surface tension, and miscibility behavior.

Schügerl et al.(S7) arrived at Eq. (I-101), i.e.,

$$kT = \frac{a}{2n\delta_o} \frac{U_{mf}(U-U_{mf})}{C_q d^4} \qquad (I-101)$$

by comparing their gas-fluidized-bed-viscosity data correlation with Eyring's rate-theory expression. An expression may be established for the minimum-fluidization velocity U_{mf} by equating Eqs. (I-70) and (I-72):

$$U_{mf} = \frac{\Delta\rho g}{k_1 \mu s^2} \frac{\varepsilon_{mf}^3}{(1-\varepsilon_{mf})} \qquad (IV-3)$$

Then, since the specific particle surface s equals 3/(2d) for spheres, the particle number density is $(1-\varepsilon)^{-1}$, and in most applications a/δ equals unity, Eq. (I-101) becomes:

$$kT = \frac{2}{9} \frac{\Delta\rho g \varepsilon_{mf}^3}{k_1 c_4 \mu d^2} \frac{(1-\varepsilon)}{(1-\varepsilon_{mf})} (U-U_{mf}) \qquad (IV-4)$$

Plotted as a function of superficial velocity, this expression exhibits particle diameter and density dependence both in slope and intercept (or zero point). It does, therefore, not permit the possibility of thermal equilibrium in a two-phase system.

Although Ruckenstein (R4) did not develope a specific expression for nominal temperature, his mean vibration velocity $\overline{v^2}$, given by Eq. (I-107), should be directly related to thermal energy, e.g., $kT \propto m\overline{v^2}$ where m is the particle mass. In that case, the resulting nominal temperature possesses a dependence upon particle properties similar to that of Schügerl's expression.

In light of the above, it was felt worthwhile to establish a "universal" temperature function for fluidization, and to use it within a single liquid model to interpret fluidized-bed behavior. It will be shown that our data support the relationship given by Eq. (IV-2).

C. Expansion Behavior

The free volume per cell in the smoothed-potential model, as for hard spheres, is given by Eq. (I-29):

$$v_f = \frac{4\pi}{3}\gamma\left(v^{1/3} - v_o^{1/3}\right)^3 \qquad (I\text{-}29)$$

The "free-volume length" ($v^{1/3} - v_o^{1/3}$) may be equivalently expressed for fluidized beds in terms of void-fraction:

$$v^{1/3} - v_o^{1/3} = v_p^{1/3}\left[(1-\varepsilon)^{-1/3} - (1-\varepsilon_o)^{-1/3}\right] \qquad (V\text{-}5)$$

where v_p is the particle volume and ε_o is the void-fraction corresponding to the minimum compressible volume v_o. Therefore, to establish the temperature dependence of the free-volume length, our expansion data were plotted as $(1-\varepsilon)^{-1/3}$ versus U. As shown in Figure IV-1, our data are well fit by a linear dependence of $(1-\varepsilon)^{-1/3}$ upon U, and the curves for the six particle sizes converge to a common intercept. To determine the particle-diameter dependence, the slopes of the six curves are plotted as a function of d in Figure IV-2. The curve drawn through the data points indicates that the curve slopes are inversely proportional to $d^{1.7}$. Our expansion data are, therefore, represented by

$$(1-\varepsilon)^{-1/3} - 1.21 = 7.1 \times 10^{-4}\, U/d^{1.7} \qquad (V\text{-}6)$$

as shown in Figure IV-3. The free-volume length is then

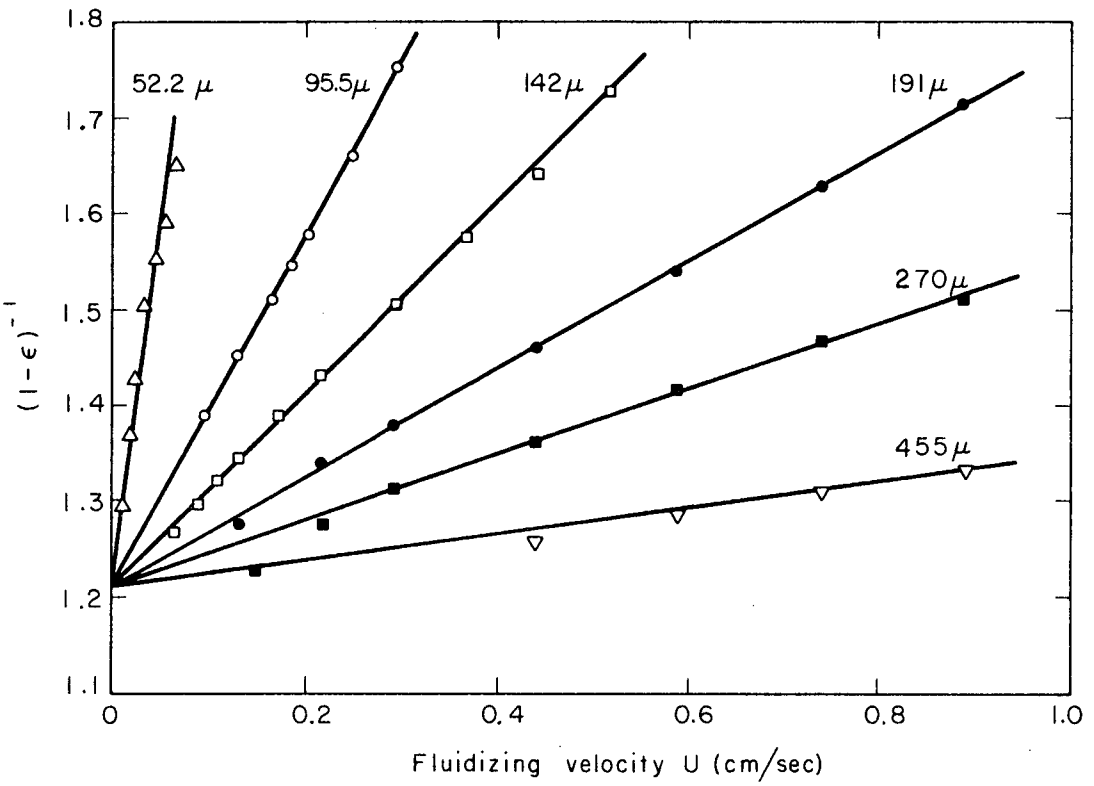

Fig. IV-1. Expansion data correlation.

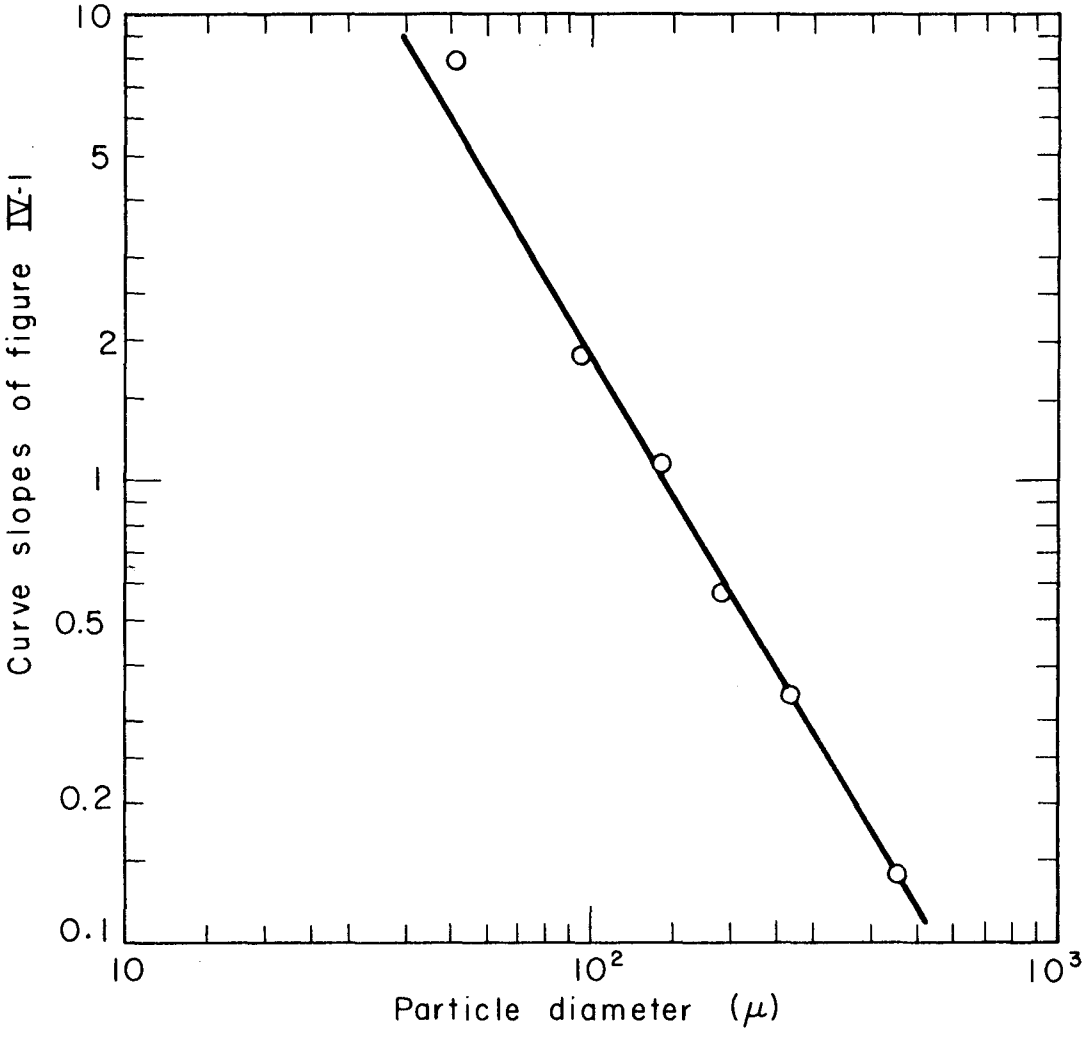

Fig. IV-2. Diameter dependence of the curve slopes of Fig. IV-1.

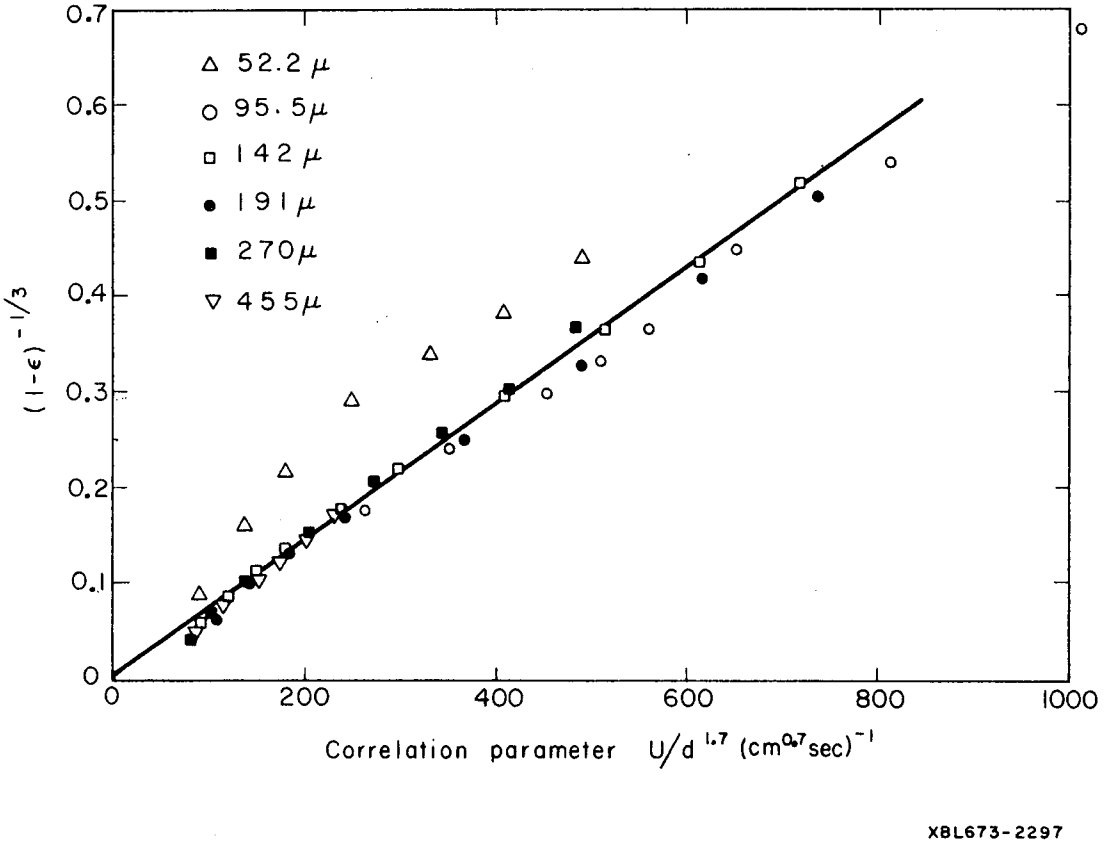

Fig. IV-3. Expansion-data correlation
△ 52.2μ ○ 95.5μ □ 142μ ● 191μ ■ 270μ ▽ 455μ.

$$v^{1/3} - v_o^{1/3} = 6.0 \times 10^{-4}\, U / d^{0.7} \qquad (IV-7)$$

where the intercept 1.21 has been equated to $(1-\varepsilon_o)^{-1/3}$.

The excellent fit to our data furnished by Eq. (IV-6) is encouraging in that it lends support to our premise that the free-volume length is a fundamental parameter for fluidized beds. Also, the common intercept $(1-\varepsilon_o)^{-1/3}$ may be identified with the zero point of temperature. That is, since we have dealt solely with geometrically similar bodies, (spheres) we would expect the nondimensional cell volume $(1-\varepsilon)^{-1}$ to approach a universal limit, e.g., $(1-\varepsilon_o)^{-1}$, as the temperature θ goes to zero. Out data indicate that the volumetric condition at zero temperature is $\varepsilon_o = 0.436$. Since we have identified the fluidized bed with the liquid state and the fixed bed with the corresponding solid state, we would not expect to ever achieve the geometric condition given by ε_o. Viewed in this light the relatively large value of ε_o suggests that bed expansion takes place in a near cubic manner with a minimum-fluidization void fraction ε_{mf} of roughly 0.476, and that void fractions of less than this are the result of geometric rearrangements caused by the relatively nonuniform flow conditions near the minimum-fluidization point. The lower velocity data points in Figure IV-1 do indeed tend to fall below the curve fitting the higher void-fractions. Thus, we conceptionally hypothesize that in the solid state, i.e., $U < U_{mf}$, particle "interpenetration" occurs. This enables identification of zero temperature with zero velocity rather than with the particle-dependent minimum-fluidization velocity, given by Eq. (IV-3), and is in accord with our statistical-

thermodynamic needs as well as the observable existence of a solid state at lower superficial velocities.

A more general form of Eq. (IV-6) can be established by dimensional analysis and use of the force balance on the particle. The relation for bed void-fraction may be functionally written:

$$(1-\varepsilon)^{-1/3}-(1-\varepsilon_0)^{-1/3}= f(d, \Delta\rho, \rho, \mu, g, U) \qquad (IV-8)$$

which by dimensional analysis simplifies to:

$$(1-\varepsilon)^{-1/3}-(1-\varepsilon_0)^{-1/3}= B_3\left(\frac{\Delta\rho}{\rho}\right)^{\alpha_2}\left(\frac{\rho U d}{\mu}\right)^{\beta_2}\left(\frac{\rho\Delta\rho g d^3}{\mu^2}\right)^{\gamma_2} \qquad (IV-9)$$

where $\rho Ud/\mu$ is the Reynolds number Re and $\rho\Delta\rho gd^3/\mu^2$ is the Archimedes number Ar. Comparing Eqs. (IV-6) and (IV-9), the exponents of the Reynolds number and Archimedes number can be immediately determined from the measured velocity and diameter dependence to be: $\beta_2=1$ and $\gamma_2=-0.9$.

Since measurements were made for only a single particle density, determination of the exponent of the density-ratio factor requires additional information. This is available from consideration of the force balance on the particle, which yields for the terminal velocity of a single particle (as discussed in Chapter I):

$$C_D u_t^2 = 4\Delta\rho g d/(3\rho) \qquad (I-7)$$

We assume that in the region of validity of the cell model the free-

volume void-fraction $[(1-\varepsilon)^{-1/3}-(1-\varepsilon_o)^{-1/3}]$ serves as a measure of the open area of the cell, and from our experimental data we know this function is linearly dependent upon the superficial velocity U. Therefore, employing Jahnig's (J1) argument that the intersticial velocity past a particle in the multiparticle system remains equal to its terminal velocity, the relation between the superficial and terminal velocities is assumed to be:

$$U = K_4 u_t \left[(1-\varepsilon)^{-1/3}-(1-\varepsilon_o)^{-1/3}\right] \qquad (\text{IV-10})$$

where K_4 is a proportionality constant. The drag coefficient C_D may be expressed as:

$$C_D = K_5 \left(\frac{\rho u_t d}{\mu}\right)^{a_1} \qquad (\text{IV-11})$$

where K_5 and a_1 depend upon the flow regime. Substituting Eqs. (IV-10) and (IV-11) into Eq. (I-71) leads to:

$$(1-\varepsilon)^{-1/3}-(1-\varepsilon_o)^{-1/3} = \frac{U}{K_4}\left[\frac{4\Delta\rho g d}{3K_5\rho}\left(\frac{\rho d}{\mu}\right)^{a_1}\right]^{\frac{1}{a_1-2}} \qquad (\text{IV-12})$$

Comparing this to Eq. (IV-6) and equating the exponents of the diameter factors, we find:

$$a_1 = 0.889 \qquad (\text{IV-13})$$

As a result, the exponent of the $\Delta\rho$ factor is -0.9; hence in Eq. (IV-9) $\gamma_2 \equiv 0$. Therefore, the more general correlation of our expansion data is

$$(1-\varepsilon)^{-1/3} - (1-\varepsilon_o)^{-1/3} = 20.0\, Re\, Ar^{-0.9} \qquad (IV-14)$$

This is of the same form as Bena's (B3) result for the laminar flow regime given by Eq. (I-80):

$$\varepsilon^{4.65} = 12.8\, Re\, Ar^{-0.89} \qquad (I-80)$$

In Figure IV-4 it is shown that

$$(1-\varepsilon)^{-1/3} - 1.21 \sim 1.5\, \varepsilon^{4.65} \qquad (IV-15)$$

Therefore, Bena's relation may be stated

$$(1-\varepsilon)^{-1/3} - (1-\varepsilon_o)^{-1/3} = 19.2\, Re\, Ar^{-0.89} \qquad (IV-16)$$

which is in excellent agreement with Eq. (IV-14), and confirms our density-ratio analysis since his experimental data encompassed density ratios of 0.2 and 1.5.

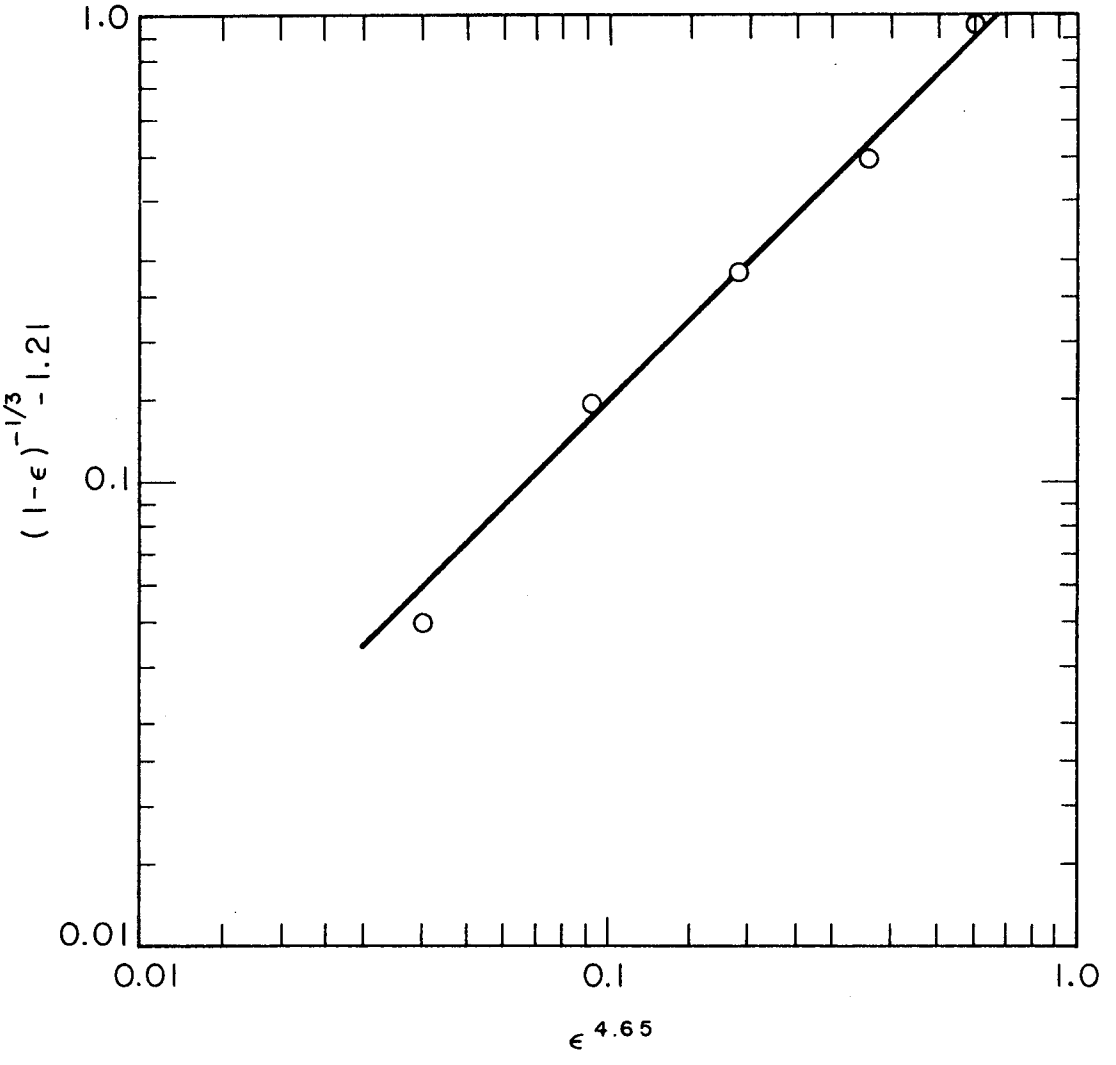

XBL673-2298

Fig. IV-4. Relationship between Bena's void fraction function $\epsilon^{4.65}$ and our own $(1-\epsilon)^{-1/3} - 1.21$.

D. Viscosity Behavior

In Chapter III the two types of viscosity measurements (using Brookfield and moving-sphere viscometers) were interpreted, and a close correspondence was found between the results of the two techniques. Thus, it is felt that a true measure of bed viscous effects was attained.

From our statistical-thermodynamic model the fluidized-bed viscosity should be given by Collins and Raffel's (C4) collision-based relation (p.31):

$$\eta = \frac{2}{5} d \left(\frac{m k T}{\pi}\right)^{1/2} \left(\frac{p_K}{kT} - \frac{1}{v}\right) \qquad (I\text{-}54)$$

where p_K is the kinetic pressure as given by the second term in Eq. (I-32):

$$p_k = \frac{kT}{v^{2/3}(v^{1/3} - v_o^{1/3})} \qquad (IV\text{-}17)$$

The internal pressure does not contribute since action at a distance is neglected in Collins and Raffel's development. The viscosity of the fluidized bed, with $\theta \equiv kT$, is then

$$\eta = \frac{2}{5\sqrt{6}} \frac{(\Delta \rho d^5 \theta)^{1/2}}{v} \frac{v_o^{1/3}}{v^{1/3} - v_o^{1/3}} \qquad (IV\text{-}18)$$

This expression may be rearranged to solve for θ:

$$\Theta = \frac{37.5}{\Delta\rho d^5}\left(\frac{v^{1/3}-v_0^{1/3}}{v_0^{1/3}}\right)^2(\eta v)^2 \qquad (\text{IV-19})$$

and from our expansion data

$$\frac{v^{1/3}-v_0^{1/3}}{v_0^{1/3}} = \frac{(1-\varepsilon)^{-1/3}-(1-\varepsilon_0)^{-1/3}}{(1-\varepsilon_0)^{-1/3}} = 5.87\times10^{-4}\,U/d^{1.7} \qquad (\text{IV-20})$$

Therefore

$$\Theta = \frac{2.59\times10^{-5}\,U^2}{\Delta\rho^{2.8}}\left(\frac{\eta v}{d^{4.2}}\right)^2 \qquad (\text{IV-21})$$

As stated previously (p.151), for thermal equilibrium to occur in two-phase systems this expression should be independent of particle properties. Accordingly our experimental viscosity data for three particle diameters and two measurement techniques are plotted in Figure IV-5 as $\eta v/d^{4.2}$ versus U. A reasonable fit to the data is offered by the indicated constant value of 62; therefore, our data support a temperature function given by

$$\Theta = 0.0330\,U^2 \qquad (\text{IV-22})$$

From dimensional considerations (p.154), this may be generalized to

$$\Theta = 3.25\times10^5\,\frac{\mu^2}{\rho g}\,U^2 \qquad (\text{IV-23})$$

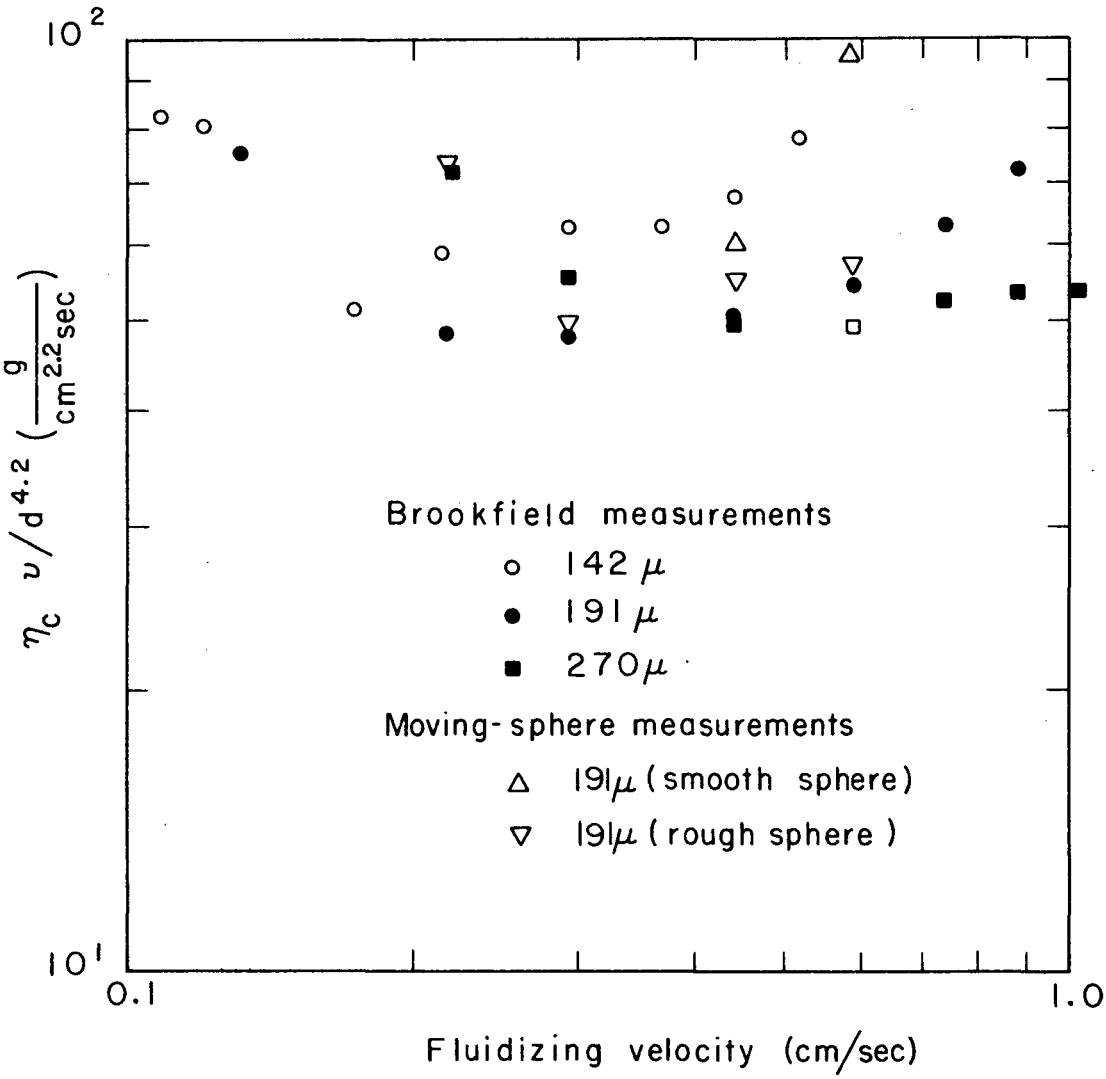

XBL673-2299

Fig. IV-5. Viscosity-data correlation
Brookfield measurements: o 142μ ● 191μ ■ 270μ
Moving-sphere measurements: △ 191μ (smooth sphere)
▽ 191μ (rough sphere).

where the constant Ω in Eq. (IV-2) has now been specified. Therefore, the definition of the nominal-temperature function for the fluidized bed has been completed, and our viscosity data attest to the lack of particle-diameter dependence in it.

A further check on the validity of Eq. (IV-23) is available from the viscosity behavior of gas-fluidized beds. Substituting Eqs. (IV-20) and (IV-23) into Eq. (IV-28) we arrive at a general viscosity expression:

$$\eta v = 6.1 \left(\frac{\mu^{0.2} g^{0.4}}{\rho^{0.6}} \right) \Delta\rho^{1.4} d^{1.2} \qquad \text{(IV-24)}$$

The experimental data of Schügerl et al. (S7) for rotating-concentric-cylinder viscometer measurements in three quartz-sand and one glass-ball systems fluidized by air are tabulated in Table IV-1. In the last two columns the experimental values for ηv are compared with those predicted by Eq. (IV-24). The agreement is to within a factor of three, which seems quite reasonable in view of the two-orders-of-magnitude difference between the viscosities of the air-fluidized systems and those of the water-fluidized systems upon which Eq. (IV-24) was based. Therefore, although the air-fluidized bed data do not suffice to confirm the absence of $\Delta\rho$ dependence in the nominal-temperature function, Eq. (IV-23), they do attest to the basic soundness of our model.

Returning to Figure IV-1, some comments may be made with regard to a region of validity for the cell model. A concave-upward bow shape can be perceived in the set of viscosity data for each particle size, i.e., at both ends of the velocity scale the viscosity values tend to rise

Table IV-1. Comparison of Schügerl, et al., data to Eq. IV-24.

Material	Density difference $\Delta\rho$ (g/cc)	Particle diameter (micron)	Fluidizing velocity (cm/sec)	Void fraction ϵ	Viscosity η (poise)	ηv ($6 \cdot cm^2/sec$)	$(\eta v)_{Eq.IV-24}$
Quartz sand (sharp edged)	2.65	350	18.7	0.598	18.42	1.03×10^{-3}	2.8×10^{-3}
			16.42	0.582	27.40	1.47×10^{-3}	2.8×10^{-3}
		275	19.0	0.622	9.18	0.264×10^{-3}	1.01×10^{-3}
			15.1	0.585	11.85	0.31×10^{-3}	1.01×10^{-3}
			13.2	0.573	13.73	0.35×10^{-3}	1.01×10^{-3}
			11.6	0.567	16.54	0.416×10^{-3}	1.01×10^{-3}
			9.14	0.537	54.9	1.29×10^{-3}	1.01×10^{-3}
		175	11.76	0.746	7.71	0.85×10^{-4}	1.53×10^{-4}
			7.38	0.739	6.76	0.725×10^{-4}	1.53×10^{-4}
			4.80	0.709	8.77	0.845×10^{-4}	1.53×10^{-4}
Glass balls (smooth)	2.88	250	15.0	0.570	14.27	2.71×10^{-4}	8.29×10^{-4}
			13.1	0.563	11.52	2.16×10^{-4}	8.29×10^{-4}
			11.1	0.554	11.32	2.08×10^{-4}	8.29×10^{-4}
			9.12	0.529	29.14	5.05×10^{-4}	8.29×10^{-4}

above the mean value predicted by our cell model. The larger values at the higher fluidizing velocities are attributable to the onset of convective motion and the beginning of cell breakup as the interparticle distance increases. The tendency for cell disruption in the relatively nonuniform lower-flow regime was mentioned on page 62 in regard to the expansion data. As a result, the accessible volume for motion diminishes more rapidly at the lower fluidizing velocities due to cell rearrangement than predicted by the cell model which assumes constant geometry; consequently, higher viscosity values are observed. Therefore, our cell model is strictly valid only in the intermediate region of most uniform fluidization, but may be extended into the higher and lower velocity regions as a relatively good approximation.

E. Miscibility Behavior

The equation of state for the smoothed-potential cell model yields for the vapor pressure (p. 19):

$$p = -\frac{1}{2}\left[\frac{d\omega(o)}{dv}\right]_{kT} + \frac{kT}{v^{2/3}(v^{1/3}-v_o^{1/3})} \qquad (I\text{-}23)$$

or

$$p = -p_{internal} + p_{kinetic} \qquad (IV\text{-}24)$$

In the fluidized bed, a balance exists between the "thermal energy" supplied to the particle by the "ether" and the consolidation pressure of the gravitational force acting on the system. The vapor pressure p may be taken to be essentially zero, as indicated by the near absence of particles above the bed. Setting p to zero in Eq. (IV-24) and solving for the internal pressure p_i:

$$p_i = p_k = \frac{\Theta}{v^{2/3}(v^{1/3}-v_o^{1/3})} \qquad (IV\text{-}25)$$

where again $\theta \equiv kT$.

With this knowledge of the internal pressure, an approximate analysis of miscibility behavior may be made within the context of the one-cell, or random-mixing, model (p. 35). This model assumes that the fluid is composed of uniform cells having mean molecular parameters determined by the average environment. The excess free energy of mixing f^E is given

by Eq. (I-61):

$$f^E = \frac{1}{2}\left[\omega_m(0) - x_1\omega_{11}(0) - x_2\omega_{22}(0)\right] - kT\ln\frac{\psi_m}{\psi_{11}^{x_1}\psi_{22}^{x_2}} \qquad (I\text{-}61)$$

where the cell partition function ψ is identical to the cell free volume v_f in the smoothed-potential model. The first term in Eq. (I-61) reflects the energetic changes involved in mixing, and the second term is related to the entropy difference resulting from free-volume changes. Hoffman et al. (H5) reported little volume change on mixing in two-and three-phase fluidized-bed systems, and our data appear to bear this out (see Table III-8). It will be assumed, therefore, that there is no volume change upon mixing, hence the second term in Eq. (I-61) goes to zero.

The cell potential $\omega(0)$ will be approximated by an internal-pressure-based relationship, which for the unmixed state is:

$$\frac{1}{2}\left[x_1\omega_1(0) + x_2\omega_2(0)\right] = -\bar{v}\left[x_1(p_i)_1 + x_2(p_i)_2\right] \qquad (IV\text{-}26)$$

and in the mixed state is:

$$\frac{1}{2}\omega_m(0) = -\bar{v}\left[x_1^2(p_i)_{11} + 2x_1x_2(p_i)_{12} + x_2^2(p_i)_{22}\right] \qquad (IV\text{-}27)$$

The geometric-mean form will be used for the mean cell volume $\bar{v}$ and internal-pressure cross-term $(p_i)_{12}$, i.e., $\bar{v}=\sqrt{v_{11}\cdot v_{22}}$ and $(p_i)_{12}=(p_i)_1^{1/2}\cdot(p_i)_2^{1/2}$. The excess free energy of mixing is then given by:

$$f^E = x_1x_2\bar{v}\left[(p_i)_1^{1/2} - (p_i)_2^{1/2}\right]^2 \qquad (IV\text{-}28)$$

and the activity coefficients may be directly determined, e.g.,

$$\ln \gamma_{12} = \frac{\partial (n_1+n_2) f^E}{\Theta \partial n_1} = \left\{ \left[\frac{(p_i)_1}{\Theta}\right]^{1/2} - \left[\frac{(p_i)_2}{\Theta}\right]^{1/2} \right\}^2 \bar{v} x_{22}^2 \qquad (\text{IV-29})$$

where γ_{12} is the activity coefficient of type-1 particles in phase 2, and x_{22} is the mole fraction of type-2 particles in phase 2. From Eq. (IV-25):

$$p_i/\Theta = \left[v^{2/3} (v^{1/3} - v_0^{1/3}) \right]^{-1} \qquad (\text{IV-30})$$

which when inserted into Eq. (IV-29) leads to

$$\ln \gamma_{12} = \frac{\left\{ v_2^{1/3} \left[v_1^{1/3} - (v_1)_0^{1/3} \right]^{1/2} - v_1^{1/3} \left[v_2^{1/3} - (v_2)_0^{1/3} \right]^{1/2} \right\}^2}{(v_1 v_2)^{1/6} \left[v_1^{1/3} - (v_1)_0^{1/3} \right] \left[v_2^{1/3} - (v_2)_0^{1/3} \right]} \qquad (\text{IV-31})$$

From the discussion of our miscibility data in Chapter III we know that in the three systems studied the solubility curves for the two phases may be reasonably approximated by a geometric-mean fit. For such systems, the particle activity coefficients can be expressed in the symmetric form:

$$\ln \gamma_{12} = A^* x_{22}^2 \qquad (\text{IV-32})$$

where $A^*>2$ must be true for immiscibility to occur. Substituting Eq. (IV-32) into the relations expressing the necessary equality of the activities of each particle in the two phases, e.g.,

$$\gamma_{12} x_{12} = \gamma_{11} x_{11} \qquad (IV\text{-}33)$$

and

$$\gamma_{22} x_{22} = \gamma_{21} x_{21} \qquad (IV\text{-}34)$$

A pair of relations may be established which enable us to evaluate A* from the experimental data:

$$A_1^* = \frac{\ln (x_{11}/x_{12})}{x_{22}^2 - x_{11}^2} \qquad (IV\text{-}35)$$

and

$$A_2^* = \frac{\ln (x_{22}/x_{11})}{x_{11}^2 - x_{22}^2} \qquad (IV\text{-}36)$$

The mixing data have been numerically interpreted in this manner, and the results are presented in Table IV-2 and Figure IV-6. A_1^* and A_2^*, which are identical when Eq. (IV-32) is exactly true, are found to be nearly equal for the two more closely-sized systems, i.e., the 142/191μ and 191/270μ mixtures, but diverge for the 95.5/191μ system. Apparently a 2:1 diameter ratio is too large to be described satisfactorily by the one-cell model. The A* values for the 142/191μ and 191/270μ systems approach the immiscibility limit of 2 at low fluidizing velocities, but increased immiscibility occurs at the higher velocities.

The statistical-thermodynamic relation for A* may be easily identified

Table IV-2. Experimental and theoretical A^* values for Eq. (IV-32).

System	Fluidizing velocity (cm/sec)	Mole fraction of larger particles in lower phase	Mole fraction of larger particles in upper phase	A_1^*	A_2^*	A_{JT}^*
191/270μ	0.963	0.931	0.020	4.019	3.063	0.0124
	0.813	0.900	0.100	2.747	2.727	0.095
	0.664	0.850	0.150	2.478	2.478	0.57
	0.517	0.800	0.050	3.215	2.444	0.62
	0.370	0.750	0.050	3.224	2.384	1.09
142/191μ	0.813	0.983	0.021	4.014	4.197	0.00048
	0.739	0.882	0.200	2.370	2.594	0.00053
	0.517	0.927	0.010	4.647	3.034	0.267
	0.369	0.935	0.059	3.135	3.069	0.44
	0.220	0.900	0.200	2.387	2.701	0.43
	0.118	0.700	0.240	2.195	2.150	1.18
95.5/191μ	0.371	0.980	0.009	4.778	4.064	1.656
	0.292	0.950	0.001	6.887	3.318	2.26
	0.218	0.890	0.006	5.123	2.779	3.2
	0.183	0.890	0.002	6.198	2.784	3.95

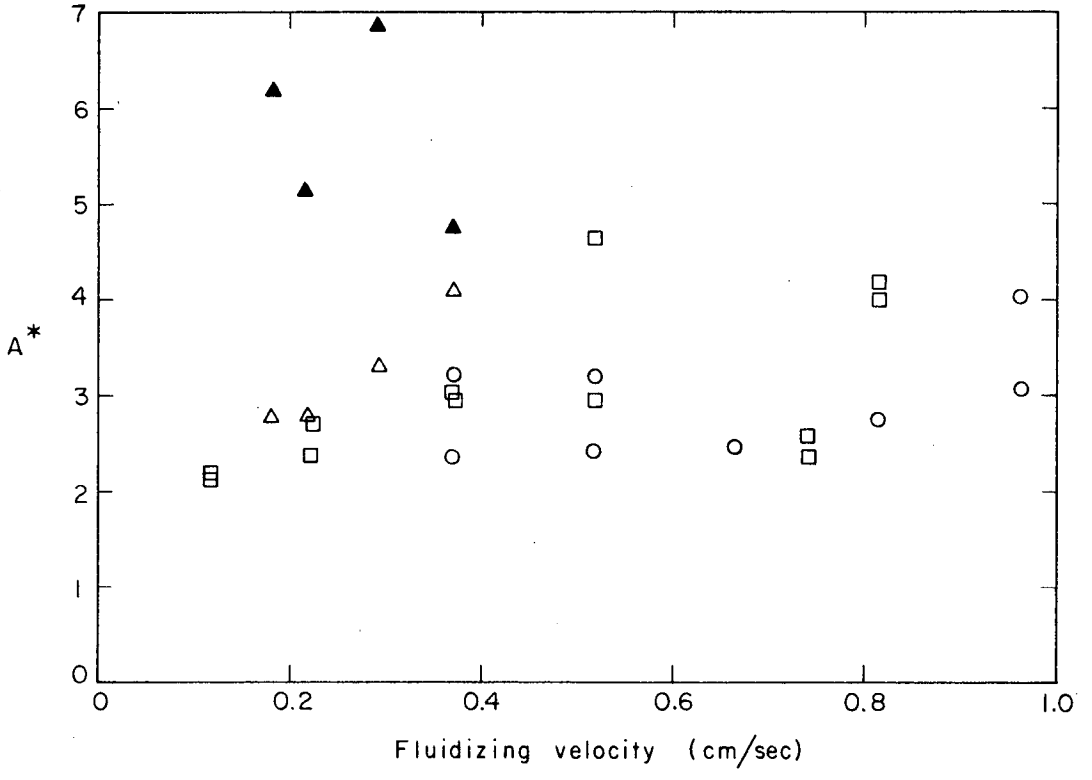

Fig. IV-6. Fluidizing velocity (cm/sec).

by comparing Eqs. (V-31) and (V-32):

$$A_{ST}^{*} = \frac{\left\{ v_2^{1/3}\left[v_1^{1/3} - (v_1)_o^{1/3}\right]^{1/2} - v_1^{1/3}\left[v_2^{1/3} - (v_2)_o^{1/3}\right]^{1/2} \right\}^2}{(v_1 v_2)^{1/6}\left[v_1^{1/3} - (v_1)_o^{1/3}\right]\left[v_2^{1/3} - (v_2)_o^{1/3}\right]} \qquad (V-37)$$

The calculated values for A_{ST}^{*} have been listed in the last column of Table V-2. For the lower velocities ($U<0.7$), at which our cell model is valid (see p. 169), the results agree with the experimental data to within an order of magnitude, but do not exhibit the correct velocity, i.e., "temperature", dependence.

Although the failure to predict the proper velocity dependence indicates a defect in our present miscibility expression, the order-of-magnitude agreement is encouraging and suggests that use of a refined definition for the internal pressure p_i could bring the statistical-thermodynamic prediction into line with the experimental observations. Examination of particle terminal-velocity behavior and the transition from particulate to aggregative fluidization should enable resolution of a nonzero vapor pressure p. Then the revised internal pressure, given by Eq. (IV-24), may be used with Eq. (V-28) to predict mixing behavior. Alternatively, by definition p_i can serve to define the cell partition function $\omega(0)$:

$$\frac{1}{2}\omega(0) = \int_{v_{ref}}^{v} p_i \, dv \qquad (V-38)$$

which with Eq. (I-61) more directly defines the miscibility behavior.

A further improvement would be to utilize the two-cell model (p36) to describe mixture properties. This should lead to better results for systems of large diameter ratio, e.g., $d_1/d_2 > 1.5$, but requires very accurate volumetric data for definition of the cell parameters, v_{f1} and v_{f2}.

In summary then, use of the one-cell model and assumption of zero vapor pressure yields a zero-level approximation to miscibility behavior. In effect, we have conducted a feasibility investigation, the results of which indicate that our smoothed-potential cell model can be used to predict fluidized-bed miscibility behavior.

F. Surface - Wave Behavior

The cell-model expression for surface tension, modified to be in accord with Eötvos' law (E2), is given by Eq. (I-39), with $\theta \equiv kT$:

$$\sigma v^{2/3} = \frac{\omega_s(0)-\omega(0)}{2} - \theta \ln\left(\frac{v_s}{v_f}\right) \qquad (\text{IV-39})$$

where the configuration-energy difference $\omega_s(0)-\omega(0)$ and the free-volume ratio v_s/v_f are assumed to be independent of the temperature θ. In accord with this equation, our experimental data for σ are plotted as $\sigma v^{2/3}$ versus U^2 in Figure IV-7. From the intercept and slope of the linear fit to the three data points, the following values are ascertained:

$$\frac{\omega_s(0)-\omega(0)}{2} = 9.3 \times 10^{-4} \text{ erg} \qquad (\text{IV-40})$$

and

$$v_s = 0.905\, v_f \qquad (\text{IV-41})$$

Eq. (IV-41) states that the free volume of the surface particles is less than the free volume of the bulk particles. This is true in liquid molecular structure due to the asymmetric net-downward force on the surface molecule caused by a larger number of attractive-force centers (molecules) below it than above it. In the fluidized bed, the surface particle lies at the point of flow-channel expansion, with associated fluid-velocity diminishment. The surface particle, thus, senses a flow velocity somewhat

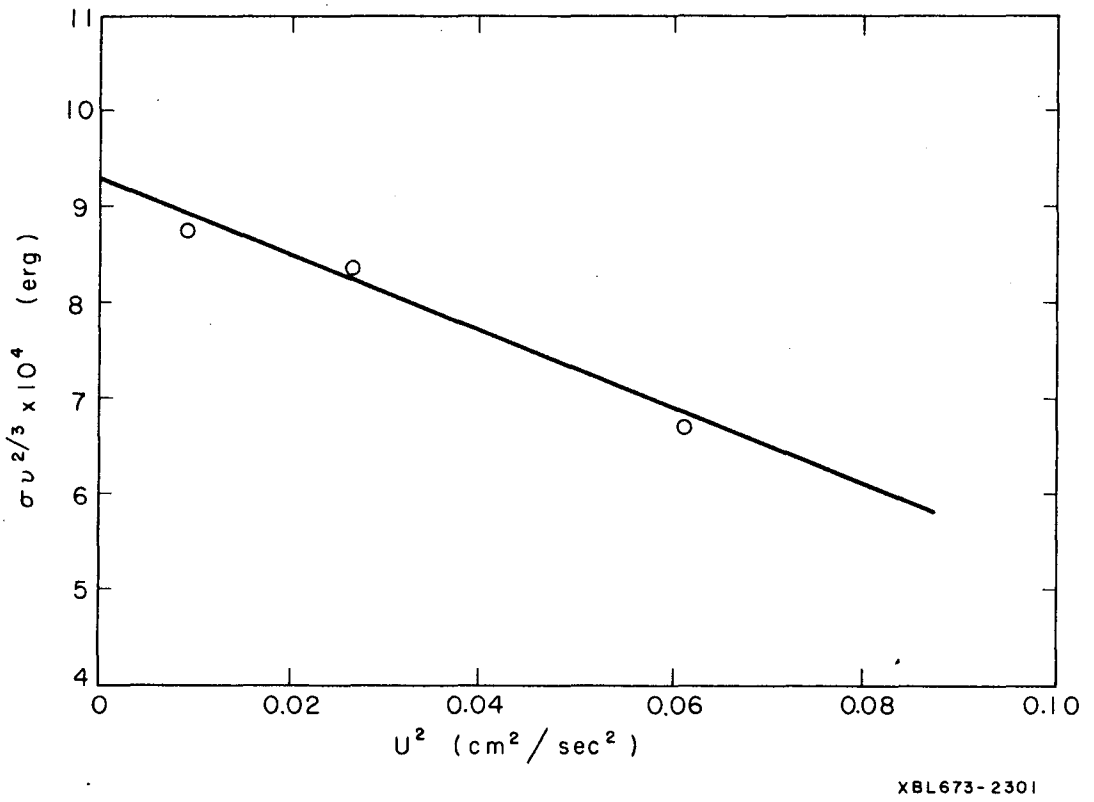

Fig. IV-7. Surface-tension correlation from surface-wave measurements for 95.5μ fluidized particles.

less than the interstitial-flow velocity through the bed, and does not require as great a volume. The lower free volume of the surface particles, predicted by Eq. (IV-41), is, therefore, in line with physical reality.

G. Self - Diffusion Analysis

An expression for the self-diffusion coefficient D_s, related to Eq. (I-54) for the viscosity, is given by Eq. (I-55), with $\theta \equiv kT$:

$$D_s = \frac{5}{12}\left(\frac{\theta}{\pi m}\right)^{1/2}\left[\alpha^2\left(\frac{p_k}{\theta} - \frac{1}{v}\right)\right]^{-1} \qquad (IV-42)$$

INserting the expression for p_K given by Eq. (IV-25):

$$D_s = \frac{5}{12\alpha^2}\left(\frac{\theta}{\pi m}\right)^{1/2}\frac{v\left(v^{1/3}-v_o^{1/3}\right)}{v_o^{1/3}} \qquad (IV-43)$$

and replacing $(v^{1/3}-v_o^{1/3})/v_o^{1/3}$ and θ by their fluidized-bed relations, Eqs. (IV-5), (IV-14), and (IV-23), we arrive at a general expression for the diffusivity:

$$\frac{D_s}{v} = 3.13\times 10^{-3}(1-\varepsilon_o)^{1/3}\left(\frac{\mu^{1.8}}{\rho^{0.4}g^{1.4}}\right)\left(\frac{v^2}{\Delta\rho^{1.4}d^{5.2}}\right) \qquad (IV-44)$$

Kennedy and Bretton (K7) have recently made diffusivity measurements in closely-sized glass-sphere systems fluidized by water. A comparison of their experimental results with diffusivities calculated by Eq. (IV-44) is given in Table IV-3. Our predicted values are seen to be roughly two orders of magnitude lower than their experimental values.

This discrepancy may be attributable in large measure to the possible existence of strong convective effects in their system. In our 455μ system

Table IV-3. Comparison of Kennedy and Bretton's data with Eq. IV-45.

Particle diameter (micron)	Density difference $\Delta\rho$ (6/cc)	Fluidizing velocity (cm/sec)	Void fraction ϵ	Kennedy and Bretton's explanation diffusivity (cm^2/sec)	$(D_s)_{Eq.\ IV-45}$
912	1.862	2.09	0.511	0.96	0.0145
946	1.862	2.06	0.513	0.60	0.0134

we observed the onset of convective currents (see p. 92) not present in the smaller-diameter systems on which Eq. (IV-45) is based. In their study they employed only particles that were more than twice as large, i.e., 912 - 973μ, as those which we found to be unstable. Wilde (W1) in his photographic study of water-fluidized glass spheres of slightly larger diameter, i.e., 2400 - 5000μ, found convective currents to be significant.

In addition to comparably large particle diameters, Kennedy and Bretton employed a relatively small column diameter, i.e., 1.0 inch. Therefore, the influence of the wall is felt to a greater extent in their system than in our much larger 8-17/32-inch-diameter bed.

For both these reasons, it is suspected that convective currents were significant in their bed, and led to larger measured diffusivities than predicted by our statistical-thermodynamic model, which assumes smooth, nonconvective fluidization. Thus, it was proposed in section E.4 of Chapter III that a careful experimental study of diffusion be made with our fluidization system using the sampling tube employed for the miscibility measurements.

ACKNOWLEDGEMENTS

Thanks are due to G. G. Young and Mel Flamm for their suggestions with regard to equipment design, and their rapid and skillful fabrication of the experimental apparatus.

This work was performed under the auspices of the U. S. Atomic Energy Commission.

APPENDICES

A. Rotameter Calibration

The three parallel rotameters were calibrated by collecting and weighing the outflow from each over a specified time interval. The measured weight-flow rate of water w was converted to the superficial velocity U through our 8-17/32-inch-diameter column by

$$U = \frac{w}{\rho A} = 0.0406\, w \qquad (A\text{-}1)$$

The calibration curves in Figure A-1 were established by this procedure.

B. Particle - Size Distributions

The actual size distribution for each of the six nominal particle diameters was established by counting and measuring the particles in microphotographs (see Figure III-6). The distributions for the 52.2, 95.5, 142, and 191μ sizes are given in Figures A-1 - A-5. The arithmetic-mean diameter was used to characterize the particles:

$$d = \frac{\sum_{j=1}^{i} n_j d_j}{\sum_{j=1}^{i} n_j} \qquad (A\text{-}2)$$

where n_j is the number of particles of diameter d_j observed in the micro-photograph. For example, in the case of the 142μ particles, from Figure A-4:

$$d = \frac{1(100) + 2(120) + 1(125) + 4(130) + 2(135) + 6(140) + 4(145) + 4(150) + 2(155) + 2(160)}{1+2+1+4+2+6+4+4+2+2} \qquad (A\text{-}3)$$

$$= \frac{398.5}{28} = 142.3\,\mu$$

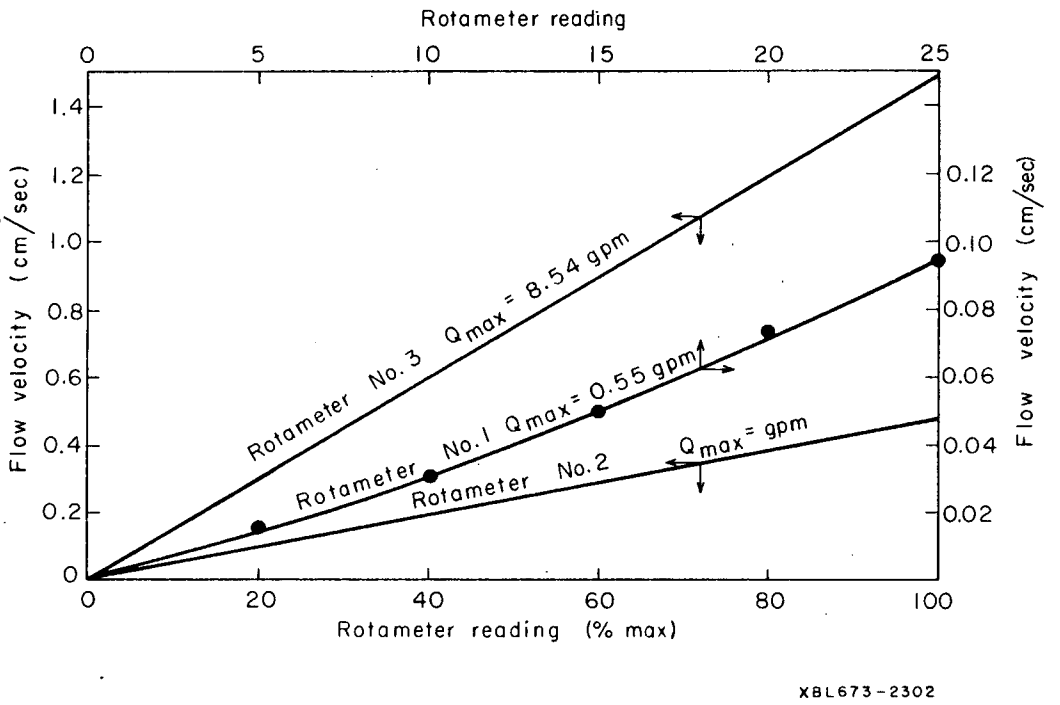

Fig. A-1. Rotameter calibration chart velocity values based on 8-17/32-inch diameter column.

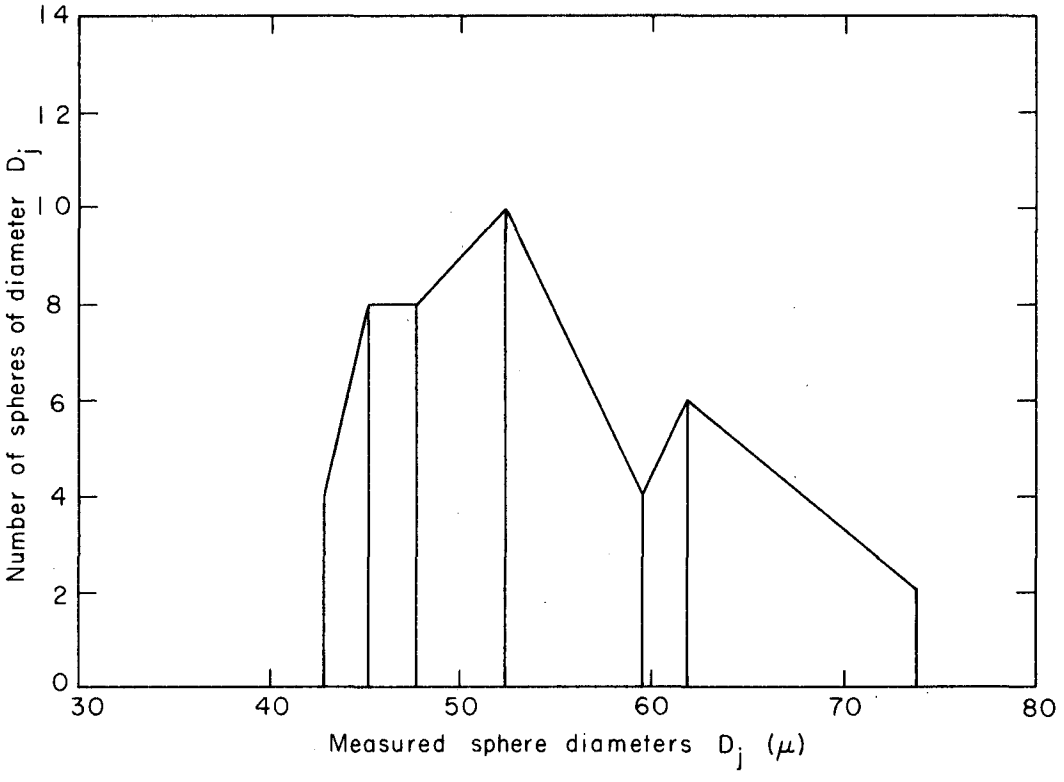

Fig. A-2. Size distribution of 52.2μ particles.

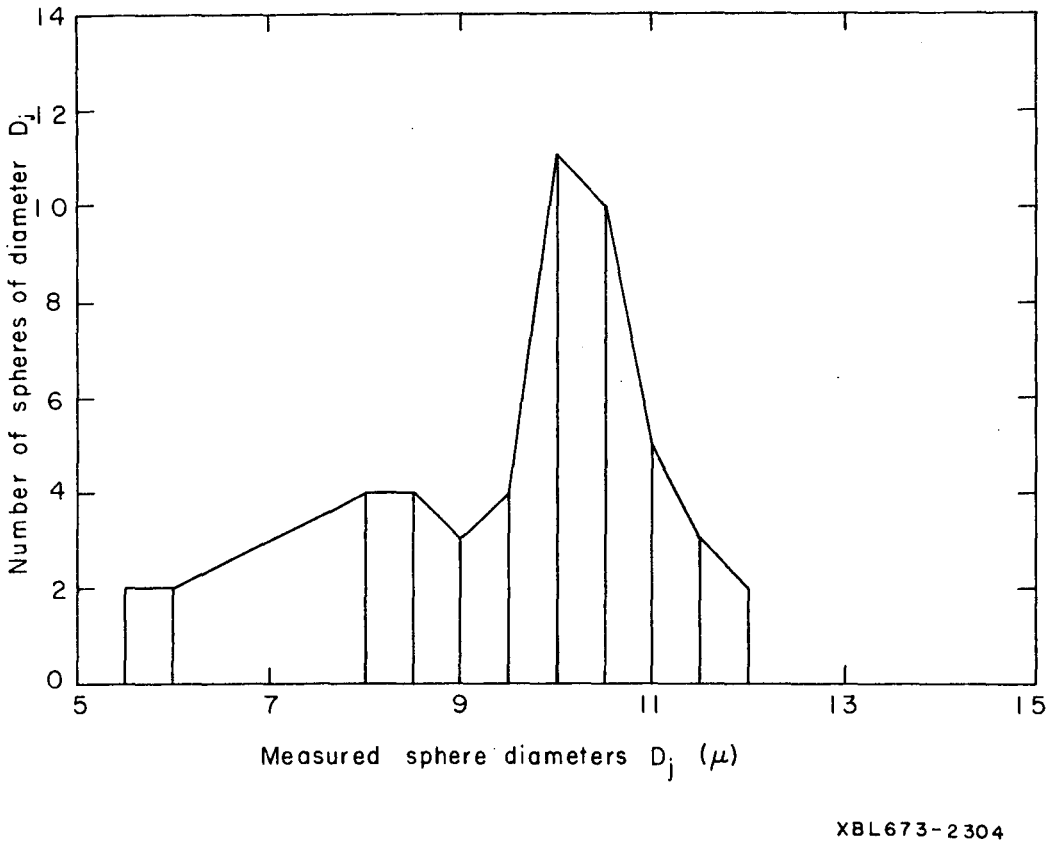

Fig. A-3. Size distribution of 95.5μ particles.

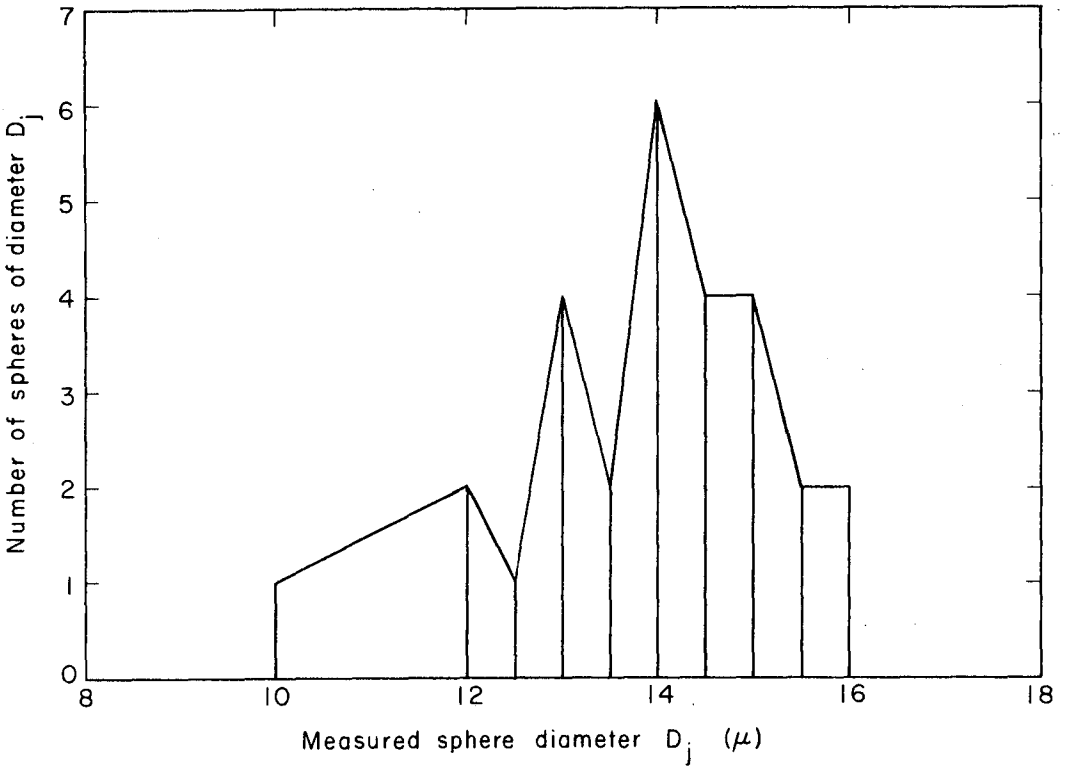

Fig. A-4. Size distribution of 142μ particles.

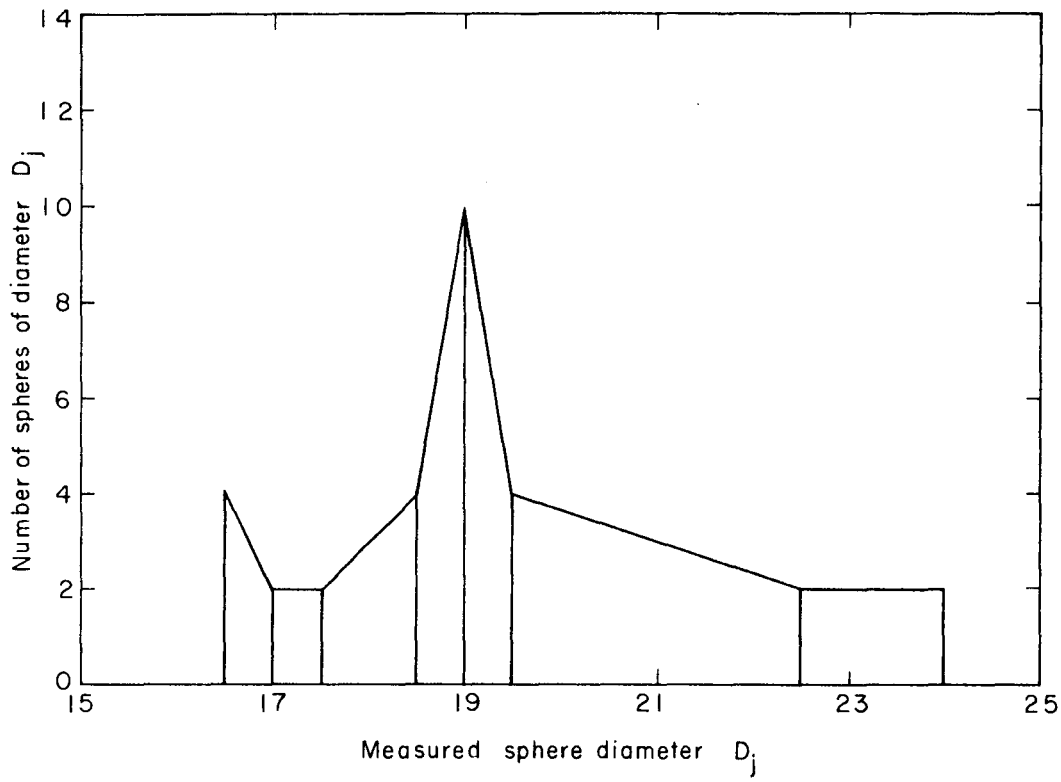

Fig. A-5. Size distribution of 191μ particles.

NOMENCLATURE

Latin Letters

a	cell radius
a	diffusion "jump distance"
a_p	amplitude of particle oscillation
A	number of nearest neighbors (p. 16)
A	Molecular shielding factor (p. 30)
A	fraction minimum area in direction of fluid flow
A^*	parameter in Eq. (IX 32) for the activity coefficient
A_0	experimentally-determined constant
A_1	parameter defined by Eq. (I 97)
Ar	Archimedes' number
B_0	experimentally-determined constant
B_1	parameter defined by Eq. (I 98)
c	wave velocity (p. 24)
c	concentration of diffusion component (p. 49)
$\vec{c}$	molecular velocity
$\vec{c}_o$	mean molecular velocity
C_4	function of particle shape in Eq. (I 98)
C_B	drag coefficient in bed
C_D	particle drag coefficient for free fall
c_0	concentration of diffusion component at injection point

d length parameter in Lennard-Jones potential (p. 16)

d particle diameter (p. 41)

d_l length parameter in the two-cell model

d_m distance parameter in the one-cell model

d_s metallic sphere diameter

$d\vec{p}_i$ volume element in momentum space

$d\vec{r}_i$ volume element in position space

dQ infinitesimal heat flux

D overall column diameter of bed

D_j equilibrium value of a representative property in the jth quantum state

D_s self-diffusion coefficient

$D(\tau)$ strain function, i.e., velocity gradient

E_f empirical constant in Eq. (192)

E_j energy of the jth quantum state

E_s solid-diffusion coefficient

$f^{(2)}$ nonequilibrium pair-distribution function

f^E excess free energy of mixing (Helmholz)

$f(q, \vec{p}, t)$ nonequilibrium distribution function

F force; Helmholz free energy

F_D measured drag force corrected for buoyancy and pulley friction

F_f fluid drag force

F_f empirical constant in Eq. (192)

F_s fluidized-particle drag force

f pulley friction

g gravitational acceleration

$\vec{g}$ relative velocity of two molecules, $\vec{c}_1 - \vec{c}_2$

$g^{(3)}_{\alpha\alpha\alpha}$ triplet distribution function

g_{ij} pair-distribution function of molecules i and j

$g(r)$ radial distribution function

$g_o^{(2)}(r)$ equilibrium radial distribution function

G_f empirical constant in Eq. (I 90)

h fluid depth (p. 25)

h bed height (p. 82)

h_o unfluidized bed height

H Hamiltonian

$H_{s,\,mf}$ rate of energy dissapation at minimum fluidization

$\underset{\sim}{J}$ flux tensor

k Boltzmann constant

k_1 constant in Eq. (I 72)

k'_0 frequency of diffusion "jump distances" in absence of external forces

$\vec{k}$ unit vector along line of molecular centers at collision

K empirical constant in Eötvos' Law

K_1 integration constant in Eq. (III 3)

K_4 proportionality constant in Eq. (IV 10)

K_5 proportionality constant in Eq. (III 11)

l_e characteristic length of equilibrium cell volume

L bed height

$\mathcal{L}$ characteristic length of the "atmosphere" around vibrating particle

m_a apparent particle density

$n^{(1)}$ average molecule number density

N number of molecules (p. 2)

N net downward weight on pulley (p.107)

N_s number of molecules per unit interfacial area

p vapor pressure (p. 22)

p empirical constant in Eq. (194)

p^o uniform isotropic bulk pressure

p_i internal pressure

p_K kinetic pressure

q empirical constant in Eq. (194)

Q heat content

r interparticle distance

r_o outer radius of concentric-cylinder viscometer

r_i inner radius of concentric-cylinder viscometer

$\vec{r}$ radial location

$\vec{r}_i$ position vector of molecule i

Re Reynolds' number

Re_f fluid Reynolds' number

s specific particle surface

S superficial solid velocity (p. 50)

S entropy (p. 151)

t time

T absolute temperature

T_o empirical constant in Eötvos' Law

u_t particle terminal velocity

U superficial flow velocity

U_i antilog of intercept at $\varepsilon=1$ of log U vs ε curve

U_{max} empirical constant in Eq. (191)

U_{rel} relative velocity between sphere and fluid

U_s terminal moving-sphere velocity

v_o cell volume of closest packing

v_f free volume

v_{pl} particle volume of type 1 particles

v_s free volume in surface phase

v_θ angular velocity

$\bar{v}$ mean cell volume

$\overline{v^2}$ mean square oscillation velocity

$\vec{v}$ particle velocity

V volume

V_e equilibrium volume

V_{max} empirical constant in Eq. (191)

V_{mf} minimum-fluidization volume

V_s velocity of metallic sphere

w external weight

w_{11} weight-fraction in phase 1 of type-1 particles

w_{21} weight-fraction in phase 1 of type-2 particles

w_s sphere weight

$\vec{w}$ relative velocity between fluid and particles

W potential energy of system

W_{ij} intermolecular potential

x cartesian coordinate (p. 23)

x upstream distance of sample point relative to injection (p. 58)

x_1 mole-fraction of type-1 molecules

x_{11} mole-fraction of type-1 particles in phase 1

x_{22} mole-fraction of type-2 particles in phase 2

x_i mole-fraction

x_j mole-fraction

y cartesian coordinate

z cartesian coordinate

z' distance away from plane of surface

Z partition function

Z_{int} internal partition function

Z_{tr} translational partition function

Greek Letters

β reciprocal of kT

γ empirical packing parameter

γ_{12} activity coefficient of type-1 particles in phase 2

δ friction constant

δ_o distance between molecular layers

δ_f empirical constant in Eq. (I 89)

δ'_f empirical constant in Eq. (I 89)

Δl_w buoyed-line-weight difference

$\Delta\rho$ difference between moving sphere and mean bed density

ΔP pressure drop across bed

$\Delta P/L$ expansive force per unit volume

ε void-fraction function

ε_o minimum void fraction

ε_{mf} minimum-fluidized-bed void-fraction

ε^* energy

ε^*_m energy parameter in the one-cell model

ε^*_1 energy parameter in the two-cell model

$\bar{\varepsilon}$ mean void-fraction of bed

η_a apparent-fluidized-bed viscosity

θ viscometer-pointer angular deflection

λ wave length

μ fluid viscosity

ν kinetic air viscosity (p. 47)

ν wave frequency (p. 146)

ξ coupling parameter

ρ fluid density

ρ_B bed density

ρ_e contractive force per unit volume

ρ_s solid-particle density

σ surface tension

σ_{mf} empirical constant in Eq. (193)

σ_ε mean deviation of void fraction

τ tangential shear on fluid element

τ' oscillation period

τ_1 small time increment

τ_c plateau time

ϕ bulk, or dilational, viscosity

$\phi(r)$ intermolecular potential

ψ quantity being transferred [see Eq. (159)]

$\psi_2(r)$ perturbation function

$\psi_o - \phi_o$ potential energy of surface creation

ω energy of molecule in its average potential field (p. 14)

ω shear rate resulting from an imposed shear stress τ

$\omega(0)$ configuration energy of particle at cell center

$\omega(r)$ configuration energy of molecule in a symmetric cell

$\omega_{\alpha\beta}$ potential function for interaction between molecules α and β

Ω dimensionless constant in Eq. (172)

§ autocorrelation function

$\underset{\sim}{U}$ unit tensor

κ bed elasticity

Other Symbols

$\langle\ \rangle$ indicates ensemble average

double subscripts indicate properties of the pure fluids

REFERENCES

A1. B. J. Alder, J. Chem. Phys. 23, 263 (1955).

A2. E. A. da C. Andrade, Phil. Mag. 17, 497 (1934).

B1. M. Born and H. S. Green, Proc. Roy. Soc. A188, 10 (1946).

B2. W. B. Brown, Phil. Trans. Roy. Soc. of London 250-A, 175 (1957).

B3. J. Benâ, Chemicky Prùmysl 8 (10) 516 - 23 (1958).

B4. A. M. Binnie, Trans. Instu. Chem. Engrs. 41, 17 (1963).

B5. R. Bart, Mixing of Fluidized Solids in Small-Diameter Columns (ph.D. Thesis), Mass. Inst. of Tech., 1950 (unpublished).

B6. A. J. Batschinski, Z. Physik. Chem. 84, 643 (1913).

C1. F. Cernuschi and H. Eyring, J. Chem. Phys. 7, 547 (1939).

C2. S. Chapman and T. G. Cowling, Mathematical Theory of Non-Uniform Gases (Cambridge University Press, Cambridge, 1951).

C3. F. C. Collins and H. Raffel, J. Chem. Phys. 22, 1728 (1954).

C4. F. C. Collins and H. Raffel, Advances in Chemical Physics (Interscience Publishers, Inc., New York, 1958) Vol. I, pp. 135-164.

D1. J. S. Dahler, J. O. Hirschfelder, and H. C. Thatcher, Jr., J. Chem. Phys. 25, 249 (1956).

D2. J. S. Dahler and J. O. Hirschfelder, WADC TN59-234.

D3. J. deBoer, Physica 20, 655 (1954).

D4. J. deBoer, Repts. Progr. in Phys. 12, 305 (1949).

D5. T. C. Daniels, J. Mech. Eng. Sci. 4, 103 (1962).

D6. R. Diekmann and W. L. Forsythe, Jr., Ind. Eng. Chem. 45, 1174 (1953).

D7. R. E. De La Rue and C. W. Tobias, J. Electrochem. Soc. 106, 827 (1959).

E1. H. Eyring and J. O. Hirshfelder, J. Chem. Phys. 41, 249 (1937).

E2. Eötvos, Wied. Ann. 27, 456 (1886).

E3. D. Enskog, Kgl. Svenska Vetenskapsakad. Handl. 63, No. 4, 1 (1921).

E4. R. Eisenschitz, Statistical Theory of Irreversible Processes (Oxford Library of the Physical Sciences, London, 1958).

E5. H. Eyring, J. Chem. Phys. 4, 283 (1936).

E6. S. Ergun, Chem. Eng. Progr. 48, 89 (1952).

F1. G. Fournet, J. Phys. Radium 592, 12 (1951).

F2. J. Furukawa and T. Ohmae, Ind. Eng. Chem. 50, 821 (1958).

G1. E. A. Guggenheim, Mixtures (Oxford University Press, London, 1952).

H1. Terrell L. Hill, Introduction to Statistical Thermodynamics (Addison-Wesley Publishing Company, Inc., Massachusetts, 1960).

H2. Terrell L. Hill, op. cit., p. 4.

H3. D. R. Hartree, Proc. Camb. Phil. Soc. 24, 89 (1928).

H4. J. H. Hildebrand and R. L. Scott, Regular Solutions (Prentice-Hall, Inc., New Jersey, 1962).

H5. R. F. Hoffman, L. Lapidus, and J. C. Elgin, AIChE J. 6, 321 (1960).

H6. A. Harasima, Advances in Chemical Physics, (Interscience Publishers, Inc., New York, 1958) Vol. I, p. 229.

I1. J. H. Irving and J. G. Kirkwood, J. Chem. Phys. 18, 817 (1950).

J1. C. E. Jahnig, Generalized Correlation for Free Fall and Multiparticle Systems, paper presented at the annual AIChE meeting, Chicago, Illinois, (December, 1957).

J2. R. Jottrand, J. Appl. Chem. 2, Supplementary Issue No. 1, S17 (1952).

K1. J. G. Kirkwood, J. Chem. Phys. 3, 300 (1935).

K2. J. G. Kirkwood, E. K. Mann, and B. J. Alder, J. Chem. Phys. 18, 1040 (1950).

K3. J. G. Kirkwood and F. P. Buff, J. Chem. Phys. 17, 338 (1949).

K4. J. G. Kirkwood, J. Chem Phys. 14, 180 (1946).

K5. J. G. Kirkwood, F. P. Buff, and M. S. Green, J. Chem. Phys. 17, 988 (1949).

K6. J. Kozeny, Ber. Wien Akad., 136A, 271 (1927).

K7. S. C. Kennedy and R. H. Bretton, AIChE J. 12, 24 (1966).

L1. J. E. Lennard-Jones and A. F. Devonshire, Proc. Roy. Soc. A163, 53 (1937).

L2. J. E. Lennard-Jones and J. Corner, Trans. Faraday Soc. 36, 1156 (1940).

L3. J. E. Lennard-Jones and J. Corner, Trans. Faraday Soc. 36, 1156 (1940).

L4. H. C. Longnet-Higgins and J. A. Pople, J. Chem. Phys. 25, 884 (1956).

L5. F. F. Liu and C. Orr, Jr., J. Chem. and Eng. Data 5, 430 (1960).

L6. R. P. Levey, A. de la Garza, S. C. Jacobs, H. M. Heidt, and P. E. Trent, Chem. Eng. Prog. 56, 43 (1960).

L7. A. L. Loeffler and B. F. Ruth, AIChE J. 5, 310 (1959).

M1. L. M. Milne-Thomson, Theoretical Hydrodynamics (MacMillan Co., New York, 1957), 3rd. ed., p. 394.

M2. G. L. Matheson, W. A. Herbst, and P. H. Holt, II, Ind. Eng. Chem. 41, 1099 (1949).

M3. W. G. May, Dechem. Monogr. 32, 261 (1959).

M4. L. Massimilla and S. Bracale, Ric. Sci. Mem. 27, 1509 (1957).

M5. J. C. Maxwell, Electricity and Magnetism (Oxford University Press, London, 1892), Vol. 1, 3rd. ed., p. 440.

N1. L. H. Nosanow, J. Chem. Phys. 30, 1596 (1959).

O1. L. Onsager, J. Am. Chem. Soc. 58, 1486 (1936).

P1. I. Prigogine, The Molecular Theory of Solutions (Interscience Publishers, Inc., New York, 1957).

P2. Proceedings of the International Union of Pure and Applied Physics on "Statistical Mechanical Theory of Transport Properties," Brussels (1956).

P3. I. Prigogine and V. Mathot, J. Chem. Phys. 20, 49 (1952).

P4. J. A. Pople, Phil. Mag. 41, 459 (1951).

P5. I. Prigogine and G. Garikian, Physica 16, 239 (1950).

P6. I. Prigogine and V. Mathot, J. Chem. Phys. 20, 49 (1952).

P7. I. Prigogine and A. Bellemans, Disc. Faraday Soc. 15, 80 (1953).

P8. R. L. Pigford and T. Baron, Ind. Eng. Chem. Fund. 4, 81 (1965).

P9. J. Pawlowski, Kolloidzschr. 130, 129 (1953).

P10. H. Pender and K. McIlwain, Electrical Engineers Handbook (Wiley Engineering Handbook Series, New York, 1950), 4th.ed., pp. 2-50.

R1. M. N. Rosenbluth and A. W. Rosenbluth, J. Chem. Phys. 22, 881 (1954).

R2. S. A. Rice and J. G. Kirkwood, J. Chem. Phys. 31, 901 (1959).

R3. J. F. Richardson and W. N. Zaki, Trans. Inst. Chem. Engrs. 32, 35 (1954).

R4. E. Ruckenstein, Ind. Eng. Chem. Fund. 3, 260 (1964).

S1. Symposium on the "Many Body Problem" in New York (1957).

S2. E. B. Smith and B. J. Alder, J. Chem. Phys. 30, 1190 (1959).

S3. Z. W. Salsburg and J. G. Kirkwood, J. Chem. Phys. 20, 1538 (1952).

S4. Z. W. Salsburg, Los Alamos Report No. LA-2667 (1962).

S5. H. C. Simpson and B. W. Rodger, Chem. Eng. Sci. 16, 153 (1961).

S6. W. W. Shuster and F. C. Haas, J. Chem. and Eng. Data 5, 525 (1960).

S7. K. Shügerl, M. Merz, and F. Fetting, Chem. Eng. Sci. 15, 1 (1961).

S8. K. S. Sutherland, Trans. Instu. Chem. Engrs. 39, 188 (1961).

T1. R. C. Tolman, The Principles of Statistical Mechanics (Oxford University Press, London, 1938).

T2. R. E. Turner, J. Chem. Phys. 29, 856 (1958).

W1. D. J. Wilde, Aggregative Fluidization of a Solid with a Liquid (M.S. Thesis), Univ. of Wash., 1956 (unpublished).

W2. R. H. Wilhelm and M. Kwank, Chem. Eng. Prog. 44, 201 (1948).

Y1. L. M. Yang, Proc. Roy. Soc. (London) A198, 471 (1949).

Z1. F. A. Zenz and D. F. Othmer, Fluidization and Fluid-Particle Systems (Reinhold Publishing Corp., New York, 1960).